Evaluation of Cooperative Navigation Strategies with Maneuvering UAVs

by

Jacob Pryor

A thesis submitted to the Graduate Faculty of
Auburn University
in partial fulfillment of the
requirements for the Degree of
Master of Science

Auburn, Alabama
August 7, 2021

Keywords: Cooperative Navigation, Relative Navigation, Sensor Fusion

Approved by

Scott Martin, Chair, Assistant Research Professor of Mechanical Engineering
David Bevly, Professor of Mechanical Engineering
John Hung, Professor of Electrical and Computer Engineering

Abstract

This thesis presents and evaluates cooperative navigation methods used to reduce navigation solution error growth between members of an unmanned aerial vehicle - unmanned ground vehicle (UAV-UGV) or all-UAV team when Global Position System (GPS) measurements are partially or completely unavailable to the group. Multiple scenarios with varying numbers of vehicles were simulated with a centralized navigation algorithm based on the Extended Kalman Filter (EKF) and with a decentralized navigation algorithm based on the Covariance Intersection (CI) filter. Measurements including relative range, relative range-rate, and relative bearing were made available to the vehicles in different simulation runs to compare their impact on navigation state observability and navigation state estimation accuracy. The UAVs were also guided along varied trajectories of a "spiral" class during different simulation runs to investigate whether estimation accuracy can be improved by varying inter-vehicle dynamics and geometry.

The results of these studies show that cooperative navigation is a promising strategy to reduce navigation state error growth. To analyze the observability of the studied scenarios, a condition number test was performed on the observability Gramian matrix. This study indicates that the navigation state observability in cooperative navigation scenarios where a kinematic vehicle model is aided with relative measurements can be improved by the proposed vehicle maneuver. As the rate of the proposed spiral maneuver is increased, this analysis suggests an improvement in observability. This result is further validated in the simulated results which show that with relative bearing only, even low rates of inter-vehicle spiral motion allow for estimates of relative position with less than 3 meters of error. As the spiral rate increases, accurate relative positioning is shown to be possible with only relative range measurements. IMU biases are also shown to be estimated for cooperative

groups with low meter-level relative positioning error but no absolute position reference. In scenarios where the vehicles can accurately estimate their relative positions and at least one vehicle in the cooperative group has access to accurate GPS information, all of the vehicles in the cooperative group benefit equally through communication with that vehicle. In UAV-UGV scenarios, the cooperative group includes a heterogeneous mixture of vehicles equipped with high and low quality inertial navigation systems (INS) and/or alternative navigation methods. In this case, if the vehicles can estimate their relative positions to meter-level accuracy, all cooperating vehicles benefit with navigation solution error characteristics matching that of the most accurate navigation system in the group.

Lastly, experimentally collected data was analyzed to validate the simulation results. This experiment demonstrated similar results to the simulated scenarios. Relative position error was reduced from over 100 meters to sub-meter accuracy, depending on relative measurement availability. Absolute error was also reduced from over 70 meters (in the IMU-only case) to meter-level accuracy depending on measurement availability.

Acknowledgments

First, I would like to thank my wife, Abbi, for loving and encouraging me throughout these past two years of graduate school. I could not have done this without you. I would also like to thank my parents who have loved and supported me throughout my entire life. I thank my dad for being a good role model and my mom for always being there to encourage me. I would not be where I am today without them.

I would like to thank Dr. David Bevly for giving me the opportunity to work in the GAVLAB. I would also like to thank Dr. John Hung for his teaching, advice, and oversight on this thesis and Dr. Howard Chen for always being willing to help and offer advice despite our heated ping-pong rivalry. I would especially like to thank Dr. Scott Martin for his mentorship over the past two years and for his contributions to my education and this thesis.

I owe a lot of thanks to my fellow GAVLAB members, especially Dan Kamrath, John David Sprunger, Christian Campos-Vega, and Sam Morgan for spending many long hours helping me with data collection, Brendan Schretter and Amy Strong for always being willing to help look at data and answer questions, and Matthew Castleberry and Ben Jones for their help editing this thesis.

Most importantly, I would like to thank God for blessing me with these opportunities and for providing a way to have a relationship with Him through His son Jesus Christ (Romans 5:6-11). The work in this thesis pales in comparison to the importance of what God has done in my life and what God can do in the life of anyone who comes to Him through faith in Jesus Christ (1 Corinthians 15:1-11).

Table of Contents

List of Figures

List of Tables

List of Abbreviations

AHRS	Attitude Heading Reference System
CI	Covariance Intersection
DEM	Digital Elevation Model
DOF	Degrees of Freedom
DOP	Dilution of Precision
DSRC	Dedicated Short Range Communication
EKF	Extended Kalman Filter
EOM	Empirical Observability Gramian
GNSS	Global Navigation Satellite System
GPS	Global Positioning System
IMU	Inertial Measurement Unit
INS	Inertial Navigation System
JTIDS	Joint Tactical Information Distribution System
LOG	Linear Observability Gramian
LTI	Linear Time-Invariant
MAV	Miniature Air Vehicle
MEMS	MicroElectroMechanical Systems

NCAT	National Center for Asphalt Technology
NED	North East Down
PDOP	Position Dilution of Precision
ROS	Robot Operating System
RPMG	Relative Position Measurement Graph
UAV	Unmanned Aerial Vehicle
UGV	Unmanned Ground Vehicle
UWB	Ultra-Wide-Band
V2V	Vehicle-to-Vehicle
WGS84	World Geodetic System 1984

Chapter 1

Introduction

Recent advances in small unmanned aerial vehicle (UAV) technology have provided opportunities for small-UAV use in many applications. Some common applications of small UAVs include: search and rescue, package and disaster relief supply delivery, patrol and surveillance, infrastructure inspection, and three-dimensional mapping. Employing a team of cooperative UAVs to complete these missions is often more effective than employing a single UAV, as teams of UAVs have increased robustness, efficiency, and increased sensing capabilities. A group of UAVs is also less prone to mission failure as there is a single point of failure in single-UAV missions whereas risk is mitigated across multiple vehicles in cooperative efforts. Missions involving heterogeneous teams of unmanned ground vehicles (UGVs) and UAVs are also increasingly common in recent years. In each of these cases, one key problem that must be solved in order for the mission to be successful is vehicle navigation.

1.1 Background and Motivation

Typically, UAVs and UGVs navigate independently using an integrated GPS-INS (Global Positioning System - Inertial Navigation System) navigation solution. GPS-INS navigation has become a standard method as the combination of these two technologies provides a more accurate navigation solution than either could generate by itself.

GPS was developed by the US Department of Defense in the 1970s. The system consists of a constellation of 32 satellites orbiting Earth. The orbits are designed in such a way that at any given moment, at least 4 satellites are visible in the sky from any point on Earth. Each satellite broadcasts signals designed in such a way that a GPS receiver on Earth

can determine its range to that satellite. Because the measured range is corrupted with timing errors from the satellite and receiver clocks, it is often referred to as a "pseudorange" measurement. With a measured range to a least 3 different satellites, a receiver can estimate its position by trilateration. However, a fourth satellite measurement is typically required for a receiver to estimate its internal clock bias and accurately estimate its position. Additional satellite measurements further increase the the position accuracy of the receiver.

An INS system typically consists of an inertial measurement unit (IMU) and can also contain additional aiding sensors such as magnetometers and altimeters, among others. A 6-DOF IMU consists of 3 accelerometers that measure specific force (acceleration relative to free-fall) and 3 gyroscopes that measure angular rate. Some cheaper, consumer grade IMUs measure in fewer than 6-DOF. This thesis will consider 6-DOF IMUs. The accelerometers and gyroscopes are arranged orthogonally so that they measure values along a 3-dimensional orthogonal coordinate system. This coordinate system is typically aligned with the body frame of a vehicle. In this way, the acceleration and angular rate of the vehicle can be determined by the IMU. These measurements are integrated in time in order to calculate the attitude, velocity, and position of the vehicle.

GPS and INS measurements are highly complementary. The GPS provides an absolute, "global" navigation solution that remains very accurate over long periods of time. Stated another way, GPS navigation solutions are not subject to drift. However, GPS updates position at a relatively low update rate (usually lower than 10 Hz) and is prone to meter level "jumps" and intermittent outages. The INS solution updates at a much higher rate (100 Hz or higher) and because the INS is not dependant on outside signals, there are very few cases where INS measurements are unavailable. However, INS measurements are typically subject to noise and bias, and when integrated, this noisy, biased measurement results in a "drifting" navigation solution with errors unbounded in time. Figure 1.1 shows a typical INS drift in two-dimensions for small-UAVs over a period of 60 seconds. As can be seen in the figure, the INS navigation solution has drifted over 40 meters from the true position of the

UAV over the course of 60 seconds. Also, because the INS has no access to outside "global" information, the INS must be accurately initialized in order to provide a navigation solution. Integrated together, the GPS provides a navigation solution with error that is bounded in time that eliminates any "drift" from the integrated INS solution. Additionally, the GPS solution allows the INS measurement biases to be estimated, further reducing the overall navigation error. The INS smooths out any "jumps" in the GPS solution and can provide a sufficient navigation solution during *short* GPS outages.

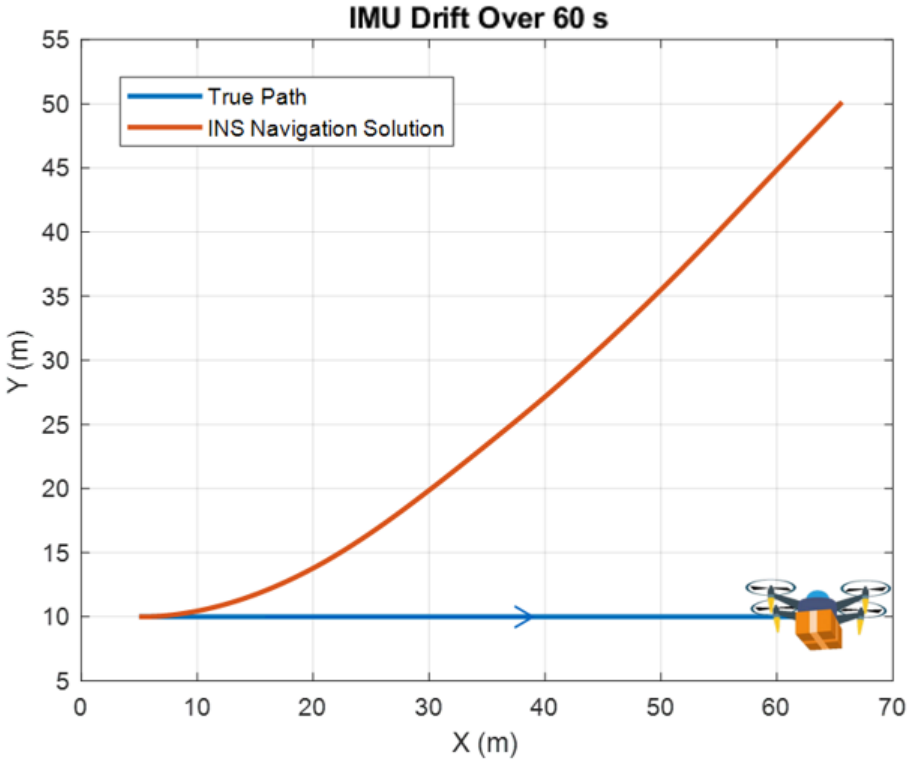

Figure 1.1: IMU drift over 60 s

However, a problem develops when accurate GPS navigation is unavailable for periods of time longer than just a few seconds. This condition is not uncommon and can be caused by any blockage of a clear view of the sky to the GPS antenna from foliage or urban canyons, intentional or unintentional jamming or spoofing, or other conditions that corrupt GPS integrity. Under these conditions, the vehicle navigation is left solely to the INS, which as previously stated is subject to an unbounded "drift." Many diverse solutions have been

suggested to combat this problem. A few of them include: visual navigation, signal-of-opportunity navigation, magnetic field based navigation, cooperative navigation, and other multisensor navigation techniques. While each of these solutions offers unique benefits, the solution that is explored in this thesis is cooperative navigation.

Cooperative navigation is an approach in which two or more cooperating vehicles share relative measurement information in order to mutually aid their own INS navigation solutions. Relative measurement information can include range, range-rate, and/or bearing. Additional shared information can include vehicle navigation state estimates and their associated uncertainty in the form of a covariance matrix. This information can be communicated between vehicles through the use of dedicated short range communication (DSRC) channels and can then be combined in a navigation filter and used to update the navigation states of each of the cooperating vehicles.

Ideally, all of this information for each vehicle would be sent to a central navigation filter where the information would be used to update each vehicles' navigation state and re-broadcast the vehicles. This type of architecture is referred to as a *centralized* filter. Two key limitations in this process are communication bandwidth and computational load. While this centralized method does offer the best possible fusion of measurement and vehicle state information, there can be an especially high load on the communication and computational capabilities of the system. For large groups of cooperating vehicles, this approach may become impossible as the amount of information that must be processed and communicated by the central navigator becomes too large. Additionally, this system architecture is not robust to failure of the central navigator.

Another commonly used architecture in cooperative navigation is *decentralized* (distributed) estimation. In this architecture, each vehicle runs its own independent navigation filter that only keeps track of its own navigation states. Inter-vehicle measurements and vehicle state information are still communicated between members of the group, but the demands

on computation and communication bandwidth are lower. This is because, as the name implies, the computational and communicational loads are distributed among the members of the group instead of concentrated at one central node. This type of system can easily accommodate vehicles entering and leaving the cooperative group and is more robust as it is not reliant on a single point of failure. Because of the reduced amount of information available to each vehicle, however, additional difficulties are encountered when processing relative measurement information with this type of estimation architecture. Additional communication channels may be required in this architecture to handle the communication between each vehicle.

One of the goals of this thesis is to explore if decentralized estimation techniques can provide sufficient navigation solutions when compared to centralized techniques to be used in UAV-UGV and UAV-only cooperative navigation. While this type of comparison has been done before [19, 20], these works considered range-only cooperative navigation and did not consider the possibility of UAV maneuver to aid cooperative navigation or an analysis of observability.

Because the scenarios in this thesis will be considering the "mid-course" of the vehicle navigation problem (i.e. excluding the initial take-off and final arrival portions of the trajectory), the primary focus will be on achieving accurate vehicle positioning solutions. While other vehicle states such as attitude and velocity may become of primary importance in the initial take-off and final arrival portions of the vehicle paths, positioning is the state of primary concern during this main part of the vehicle path.

This thesis also aims to further leverage cooperative navigation by applying this technique to scenarios with a heterogeneous group of vehicles with complimentary characteristics such as UAV-UGV navigation. Because small UAVs have a limited weight capacity, the INS used on these vehicles are generally small and relatively inaccurate. However, UAVs can freely maneuver in 3-D space and can more easily avoid GPS denied areas that result from occlusions such as dense foliage and urban canyons. Because UGVs operate on the ground,

they are often more subject to these GPS outages, but because weight is not as critical, UGVs are often equipped with higher quality, more accurate INS. UGVs can also utilize information from digital elevation models (DEM) to obtain accurate absolute positioning information in the vertical direction because they operate on the earth's surface. Cooperative navigation between UAVs and UGVs allows the sharing of this complimentary navigation information in order to provide significant navigation solution improvements for the entire cooperating group.

1.2 Prior Work

One of the first major applications of cooperative navigation technology was part of the Joint Tactical Information Distribution System (JTIDS). This system, developed by the US armed forces in the 1970's allowed for secure communication and "precision relative navigation" [39] that relied on time-of-arrival range measurements between vehicles. The introduction of this technology sparked a new area of research that has been under investigation ever since.

In [37], a cooperative navigation algorithm for GPS-denied environments was developed for miniature air vehicles (MAVs). In that paper, MAVs were assumed to be equipped with IMUs and relative range and bearing sensors. A centralized EKF was used along with a simplified planar MAV model. The work showed significant navigation accuracy improvements by utilizing the cooperative navigation system over the navigation solution calculated with only the IMU. A similar centralized EKF approach was taken in [9], except a full 6-DOF UAV was used, and UAVs were allowed to take range, range-rate, and bearing measurements. It was also assumed that landmarks with known locations were located in the environment. That paper reported the best results when a combination of range and range-rate was used. However, high levels of noise in the bearing measurement at short ranges caused an increase in error when this measurement was used. For future work, the authors

suggested development of a decentralized cooperative navigation algorithm to investigate the effect of different UAV trajectories without the presence of landmarks.

There are several key challenges noted in the literature facing the future practical implementation of cooperative navigation. Mokhtarzadeh et. al focused on issues of availability, solution integrity, and estimator architecture in [19, 20]. Availability refers to the fraction of time that cooperative navigation can be implemented between nearby vehicles due to communication and measurement range constraints. Solution integrity refers to the problem of ensuring that the cooperative navigation algorithm does not give an erroneous navigation solution without indicating proper uncertainty bounds. Estimator architecture refers to the type of estimation algorithm and communication architecture that is used in cooperative navigation.

In [3], Brink discussed the challenge of scalability. To be scalable, the system needs to minimize the number of bits sent/ received and maximize the value of those bits. To this end, this thesis seeks to evaluate potential cooperative aiding measurements in conjunction with available estimation architectures to determine which cooperative data is most beneficial. If certain combinations of cooperative measurements with estimation architecture and UAV maneuver can be shown to provide adequate navigation solutions, then additional information exchange beyond this key data can be neglected, resulting in a more scalable system that requires less information exchange.

The concept of using a vehicle maneuver and formation geometry to improve cooperative navigation accuracy has been suggested in [6, 7, 29, 31, 34, 38]. Causa investigated the case where a high flying "father" UAV maneuvers to help improve the navigation solution of a "son" UAV that operates in an environment where GPS information is occluded from almost all of the available satellites in [6]. Causa primarily focused on using the father UAV to improve the dilution of precision (DOP) characteristics of the son UAV to ultimately improve the son's navigation solution. In [34], Sharma developed an observability-based controller intended to improve the cooperative localization accuracy of a team of unmanned

vehicles in the presence of landmarks of known locations. In [31], a class of vehicle maneuvers that relied on the placement of vehicle waypoints was investigated. In this work, two vehicles were assumed to travel alongside each other from nearby start locations to similar, nearby goal locations. Vehicle position uncertainty was reduced by a factor of 15, when the vehicles were guided to certain along-route waypoints, as opposed to the case where the two vehicles traveled parallel to each other, straight to their goals throughout the entire run. Many simplifying assumptions were made in this study, including that the vehicles traveled only on a 2-D plane. To the best of this author's knowledge, no similar study that compares a class of vehicle maneuvers in 3-D space to improve cooperative navigation performance exists in the literature.

Several authors have performed observability analyses on various cooperative navigation scenarios [7, 8, 22, 36, 37]. These analyses have generally focused on simplified vehicle models with relatively few states, operating in planar environments, sometimes in the presence of landmarks of known position. The results of these analyses include that if at least one of the cooperating members has access to absolute position measurements, then the position states of the entire group become observable assuming that the relative vehicle positions can be measured [22]. In [37], Sharma et. al. show that in certain cases UAV position and heading may not be directly observable, but there still may be nonlinear combinations of these states (modes) that are observable. This work, [37], also shows that when relative range and bearing measurements are fused with IMU output, the IMU bias, relative position and relative headings become observable. Additionally, [5, 10, 16, 23, 28, 33, 36] investigate other elements of cooperative navigation, such as: adaptive cooperative navigation strategies, map-aided cooperative navigation, robustness issues, bearing-only tracking, multi-vehicle mapping, interacting multiple model radar tracking, and graph-based analysis of cooperative navigation observability. This thesis aims to perform an observability analysis that considers varied measurement availability and vehicle maneuvers to aid observability. To the best of this author's knowledge, a study of this type does not currently exist in the literature.

1.3 Contributions

Applications of centralized, EKF-based algorithms and decentralized, CI-based cooperative navigation algorithms do exist in the literature. However, a comparison of these algorithms in UAV-UGV and UAV-only scenarios with varied measurement availability and UAV maneuver to improve observability has not been explored. The primary contributions of this thesis are:

- Analysis and evaluation of both relative and absolute positioning errors for groups of cooperating vehicles in a variety of scenarios
- Evaluation and comparison of the effect of different measurements on cooperative navigation, including: relative range, relative range-rate, relative bearing, inertial, and absolute position (from GPS and/or DEM)
- Analysis of a class of UAV maneuvers to improve cooperative navigation observability and estimation accuracy
- Cooperative navigation observability analysis, considering varied measurement availability and vehicle maneuver
- Evaluation and comparison of a centralized, EKF-based cooperative navigation algorithm and decentralized, CI-based algorithm
- Simulated and experimental results of UAV-UGV and UAV only scenarios to validate the algorithms

1.4 Thesis Outline

Chapter 2 provides an introduction and background on the cooperative navigation algorithms and methods used in this thesis. This chapter also discusses the measurement models

and kinematic vehicle model. In Chapter 3, observability concepts are discussed and simulations to analyze the observability characteristics of the cooperative navigation scenarios are presented. Chapter 4 presents the simulation results of various cooperative navigation scenarios. Comparisons between the results for centralized and decentralized algorithms are made as well as a comparison of the results produced with different levels of vehicle maneuver and measurement availability. Next, in Chapter 5, results from the experimental tests are described. Lastly, in Chapter 6, final conclusions are drawn, major findings are summarized, and possible areas for future work are discussed.

Chapter 2

Cooperative Navigation Background

In order for any cooperative navigation scheme to be implemented, a state estimation algorithm that can suitably fuse sensor measurements with a dynamic system model is required. Since its invention by R.E. Kalman in 1960 [18], the Kalman filter has formed the basis of many such algorithms. The Kalman filter is a recursive algorithm, based on Bayesian estimation theory, that provides state estimates given a system model and a stream of measurements, along with associated uncertainties. These state estimates are calculated to be an optimal trade-off between model error and sensor noise. The linear, continuous-time system to be estimated is assumed to be of the form:

$$\dot{x} = Ax + Bu + w \tag{2.1}$$

$$y = Hx + \eta \tag{2.2}$$

where x is the $n \times 1$ system state, u is the $m \times 1$ input, A is the $n \times n$ system matrix, B is the $n \times m$ deterministic control input matrix, u is the deterministic control input, w is the $n \times 1$ stochastic error input which is assumed to be Gaussian and zero-mean, y is the $r \times 1$ output, and H is the $r \times n$ measurement matrix, and η is the $r \times 1$ stochastic measurement error which is also assumed to be Gaussian and zero-mean. An $n \times n$ covariance matrix of the process noise, w, is called Q. An $r \times r$ measurement covariance matrix, R, is formed from η. Note that this model assumes that all of the additive error is contained in w and η and that there is no error in H or A. If this assumption is violated, as is often the case in practical application, the performance of the algorithm can begin to break down.

While Kalman filter algorithms do commonly exist for continuous implementation, this thesis will focus on the *discrete*-time Kalman filter. A discrete system is formed by discretizing the original, *continuous*-time system. Discrete-time systems are of the form:

$$x_{k+1} = \Phi_{k,k+1} x_k + B_k u_k + B_w w_k \tag{2.3}$$

$$y_k = H_k x_k + \eta_k \tag{2.4}$$

where x_k is the system state at time k, $\Phi_{k,k+1}$ is the state transition matrix from time k to time $k+1$, B_k is the discrete control input matrix, u_k is the deterministic control input at time k, w_k is the stochastic error input, B_w is the stochastic input matrix, y_k is the output at time k, and H_k is the measurement matrix at time k, and η_k is the stochastic measurement error at time k. Similar to the continuous system, a covariance matrix of the process noise, w_k, is called Q_d, and a measurement covariance matrix, R, is formed from η_k. The state transition matrix, Φ can be derived from the original continuous system dynamic matrix by taking the matrix exponential:

$$\Phi_{k,k+1} = e^{Adt} \tag{2.5}$$

where dt is the model propagation time step. Note that for linear time-invariant (LTI) systems, Φ will be the same at every time step, but for time-varying systems, Φ should be re-calculated at every time-step. The discrete forms of B, H, and Q are calculated by:

$$B_d = \int_0^{dt} e^{A\tau} d\tau B \tag{2.6}$$

$$H_k = H \tag{2.7}$$

$$Q_d = Qdt \tag{2.8}$$

Note that this calculation of Q_d is a commonly used approximation. The discrete-time Kalman filter algorithm is implemented in two steps, the *time* update (or prediction) step

and the *measurement* update step. In the time update, the estimated state, $\hat{x}$, and its associated uncertainty, P, are propagated forward in time by:

$$\hat{x}_{k+1}^{-} = \Phi \hat{x}_k + B_d u_k \tag{2.9}$$

$$P_{k+1}^{-} = \Phi P_k \Phi^T + B_w Q_d B_w \tag{2.10}$$

where $\hat{x}_{k+1}^{-}$ and P_{k+1}^{-} are the *a priori* state estimate and covariance at time $k+1$ respectively. The propagation (2.9, 2.10) is iteratively repeated until a measurement becomes available. Then, the measurement update step can be performed. First, the Kalman gain, K, must be calculated:

$$K = \frac{P_{k+1}^{-} H_{k+1}^T}{H_{k+1} P_{k+1}^{-} H_{k+1}^T + R} \tag{2.11}$$

Next, the state estimate can be corrected:

$$\hat{x}_{k+1}^{+} = \hat{x}_{k+1}^{-} + K(y - H_{k+1}\hat{x}_{k+1}^{-}) \tag{2.12}$$

Lastly, the state covariance matrix is updated:

$$P_{k+1}^{+} = P_{k+1}^{-} - K H_{k+1} P_{k+1}^{-} \tag{2.13}$$

$\hat{x}_{k+1}^{+}$ and P_{k+1}^{+} are the *a posteriori* state estimate and covariance respectively. For a more detailed review of the Kalman filtering algorithm, see [14, 42].

2.1 6-DOF IMU Mechanization

Now that the Kalman Filter algorithm has been outlined, the specific cooperative navigation implementation can be discussed. As noted in [32], estimation approaches for vehicle dynamics can be broadly categorized as either *model*-based or *kinematic* approaches. Model-based approaches primarily rely on specific properties and dynamic characteristics of

the vehicle to define the dynamic model to be used in the time-update portion of Kalman filter-based algorithms. A model-based approach is used in [1] for the problem of small-UAV navigation. Model-based approaches take advantage of physical relationships between the vehicle and the surrounding world to predict future vehicle states. This can be a good approach assuming that the vehicle dynamics are well understood, can be modeled, and are not subject to change. Specific vehicle inputs such as steering angle and motor torque must also be measured to use this type of approach.

Instead of using specific vehicle parameters to form a dynamic model, kinematic approaches rely on the acceleration and angular rate outputs of vehicle-mounted accelerometers and gyroscopes to model the system dynamics used in the Kalman time update. One of the advantages of the kinematic approach is that it does not depend on specific vehicle parameters that are subject to change. An IMU can also be mounted to almost any vehicle to measure these outputs, so detailed dynamic modeling is not typically required for this approach. Kinematic estimation approaches are also vehicle-agnostic. Therefore, results obtained by using this type of model are more general and can be applied to multiple vehicle platforms, assuming that similar types of vehicle motion are possible. A kinematic-based approach will be used in this thesis. Specifically, the 6-DOF IMU equipped to the body-frame of each vehicle will be mechanized in a North, East, Down (NED) navigation frame. An arbitrary vehicle with body frame axes along with NED axes can be seen in Figure 2.1. The vehicle's attitude is parameterized by its roll (ϕ), pitch (θ), and yaw (ψ) angles.

Because the 6-DOF IMU is fixed to the body frame and the vehicle is navigating in the NED frame, a coordinate transformation must be made in order for the acceleration and angular-rate values measured in the body frame to provide useful NED frame information. This coordinate transformation will be handled by a 1-2-3 Euler angle rotation. "1-2-3" refers to the order of rotation. First, a "1" rotation (or rotation about the body frame "x"

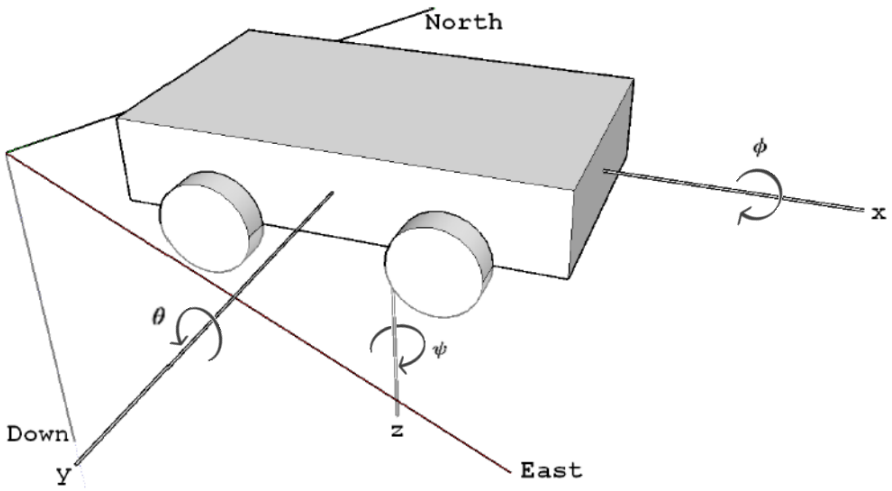

Figure 2.1: Body Frame and NED Frame [41]

or "1" axis) is made by angle ϕ. This rotation is mathematically represented by:

$$R_1(\phi) = \begin{bmatrix} 1 & 0 & 0 \\ 0 & \cos(\phi) & \sin(\phi) \\ 0 & -\sin(\phi) & \cos(\phi) \end{bmatrix} \tag{2.14}$$

Next, a "2" rotation (or rotation about the rotated frame's "y" or "2" axis) is made by angle θ. This rotation is mathematically represented by:

$$R_2(\theta) = \begin{bmatrix} \cos(\theta) & 0 & -\sin(\theta) \\ 0 & 1 & 0 \\ \sin(\theta) & 0 & \cos(\theta) \end{bmatrix} \tag{2.15}$$

Lastly, a "3" rotation (or rotation about the twice rotated frame's "z" or "3" axis) is made by angle ψ. This rotation is mathematically represented by:

$$R_3(\psi) = \begin{bmatrix} \cos(\psi) & \sin(\psi) & 0 \\ -\sin(\psi) & \cos(\psi) & 0 \\ 0 & 0 & 1 \end{bmatrix} \tag{2.16}$$

This rotation sequence allows acceleration and angular rate measurements made in the body frame to be re-oriented into the NED navigation frame. Performing the matrix multiplication results in the final body frame to navigation frame rotation matrix R_B^N.

$$
\begin{aligned}
R_B^N &= R_3(\psi)R_2(\theta)R_1(\phi) \\
&= \begin{bmatrix}
\cos(\theta)\cos(\psi) & -\cos(\phi)\sin(\psi)+\sin(\phi)\sin(\theta)\cos(\psi) & \sin(\phi)\sin(\psi)+\cos(\phi)\sin(\theta)\cos(\psi) \\
\cos(\theta)\sin(\psi) & \cos(\phi)\cos(\psi)+\sin(\phi)\sin(\theta)\sin(\psi) & -\sin(\phi)\cos(\psi)+\cos(\phi)\sin(\theta)\sin(\psi) \\
-\sin(\theta) & \sin(\phi)\cos(\theta) & \cos(\phi)\cos(\theta)
\end{bmatrix}
\end{aligned}
\tag{2.17}
$$

Rotating body frame accelerations into the NED frame is given by:

$$
\begin{bmatrix} a_N \\ a_E \\ a_D \end{bmatrix} = R_B^N \begin{bmatrix} a_x \\ a_y \\ a_z \end{bmatrix} \tag{2.18}
$$

where a_N, a_E, and a_D are acceleration in the north, east and down directions, respectively, and a_x, a_y, and a_z are the measured body frame x, y, and z direction accelerations, respectively.

One important note is that accelerometers actually measure specific force, not true acceleration. Specific force is an acceleration relative to free fall, so a freely falling accelerometer will ideally have zero output (assuming no other forces are are applied to the accelerometer body). A stationary accelerometer can measure gravitational acceleration. Once the body frame accelerations (or specific force) are rotated into the NED frame, the acceleration due to the earth's gravitation must be subtracted from the measurement. The earth's gravitation is typically taken from a pre-defined gravity model.

The World Geodetic System 1984 (WGS84) datum includes a model for the acceleration due to gravity at any given latitude that includes considerations for the Earth's rotation

rate and ellipsoidal shape. For more information on this model, see [14]. Once the properly rotated gravitational acceleration has been subtracted from the NED accelerations, they can be integrated to compute NED velocity, and these velocities can be integrated to get NED position.

In order to correctly rotate the IMU accelerometer readings into the proper frame, the gyro measurements must first be processed to obtain an updated vehicle attitude. Body frame angular rate measurements are rotated into the proper, Euler-rate frame by the following rotation:

$$\begin{bmatrix} \dot{\phi} \\ \dot{\theta} \\ \dot{\psi} \end{bmatrix} = \frac{1}{\cos(\theta)} \begin{bmatrix} \cos(\theta) & \sin(\phi)\sin(\theta) & \cos(\phi)\sin(\theta) \\ 0 & \cos(\phi)\cos(\theta) & -\sin(\phi)\cos(\theta) \\ 0 & \sin(\phi) & \cos(\phi) \end{bmatrix} \begin{bmatrix} g_x \\ g_y \\ g_z \end{bmatrix} \tag{2.19}$$

where g_x, g_y, and g_z are the body frame angular rates, and $\dot{\phi}$, $\dot{\theta}$, and $\dot{\psi}$ are the Euler rates. These Euler rates are integrated to calculate the Euler angles. The 6-DOF IMU mechanization algorithm described above, is summarized in Figure 2.2. Note that for this mechanization to be performed, position, velocity, and attitude must be accurately initialized by some other navigation technique (eg. GPS). In this work, the 15×1 state vector of the

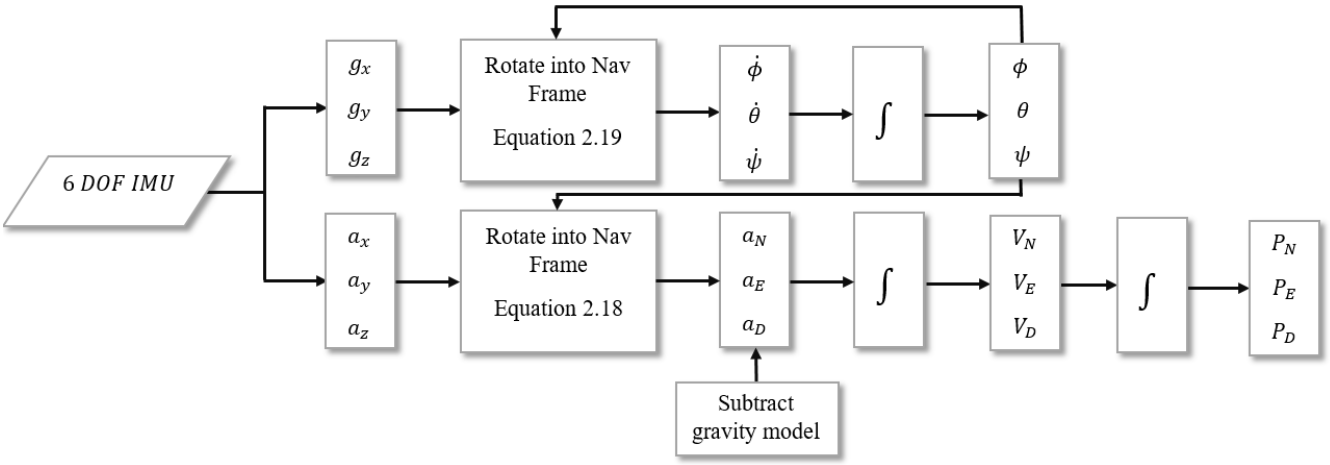

Figure 2.2: IMU Mechanization

ith vehicle is formulated as:

$$\boldsymbol{x}_i = \begin{bmatrix} \boldsymbol{P}_{NED} \\ \boldsymbol{V}_{NED} \\ \boldsymbol{\Psi} \\ \boldsymbol{b_a} \\ \boldsymbol{b_g} \end{bmatrix} \tag{2.20}$$

where $\boldsymbol{P}_{NED}$ is the 3×1 NED-frame position vector of the vehicle, $\boldsymbol{V}_{NED}$ is the 3×1 NED velocity vector, $\boldsymbol{\Psi}$ is the 3×1 vector of "1-2-3" Euler Angles, and $\boldsymbol{b_a}$ and $\boldsymbol{b_g}$ are the 3×1 accelerometer and gyro biases of the IMU, respectively. These accelerometer and gyro biases will be discussed in more detail in the next section.

2.2 Measurement Models

In this work, measurements are taken from on-board navigation sensors and then processed in order to compute a navigation solution. Each of these measurements is subject to a variety of sources of error and can be modeled by mathematical equations.

2.2.1 IMU Model

As noted in Chapter 1, IMU measurements are subject to noise and bias. Additional error sources for IMUs include scale factor errors, cross-coupling errors, errors associated with temperature, and vibration induced errors [14]. The IMU model used in this thesis assumes that all of the deterministic sources of IMU error can be removed by calibration, or are negligible. This leaves the primary error sources as a zero-mean, Gaussian noise and a "random walk" bias. The accelerometer output for a given body-frame direction is:

$$a_{meas} = a_{body} + b_a + \eta_a \tag{2.21}$$

where a_{meas} is the measured output, a_{body} is the true body-frame acceleration, b_a is the "random walk" bias, and η_a is the zero-mean, Gaussian noise with standard deviation σ_a. The "random walk" bias, b_a, is not truly a random walk, as it is modeled by a first order Gauss-Markov process:

$$\dot{b_a} = -\frac{1}{\tau_{bias}}(b_a + \eta_b) \tag{2.22}$$

where τ_{bias} is the time constant associated with the Gauss-Markov process, and η_b is a zero-mean, Gaussian noise term with standard deviation σ_b that drives the Gauss-Markov process.

As can be seen in Equations 2.21 and 2.22, there are three parameters that determine the "quality" of the IMU measurements (σ_a, σ_b, and τ_{bias}). These parameters can be determined by forming an Alan variance plot from static IMU data. For a detailed explanation on this process, see [41]. Five general "quality" levels or grades of IMUs are defined in [13, 14]. From least accurate to most accurate, these grades are: consumer, tactical, intermediate, aviation, and marine. Table 2.1 shows typical biases for each of these IMU grades, as reported in [14].

Table 2.1: Typical accelerometer and gyro biases for different grade IMUs (from:[14])

IMU Grade	**Accelerometer Bias** (m/s^2)	**Gyro Bias** (deg/s)
Marine	10^{-4}	0.001
Aviation	$3 \times 10^{-4} - 10^{-3}$	0.01
Intermediate	$0.001 - 0.01$	0.1
Tactical	$0.01 - 0.1$	$1 - 100$
Consumer	> 0.03	> 100

In this thesis, UAVs are assumed to be equipped with IMUs that fit into a low quality tactical grade, and UGVs are equipped with IMUs that fit into either a high quality tactical or low quality intermediate grade. This is because, as previously mentioned, the higher grade IMUs are typically also larger in size, and UGVs are not subject to the same size and weight

constraints as UAVs. In the simulations, parameters, (σ_a, σ_b, and τ_{bias}), were set so that the bias values for the IMUs are characteristic of the IMU grade as defined in Table 2.1.

Using this model, with the states described in Equation 2.20, the process noise covariance matrix, Q, for each vehicle is defined as in Groves, [14]:

$$Q = \begin{bmatrix} 0_3 & 0_3 & 0_3 & 0_3 & 0_3 \\ 0_3 & S_a I_3 & 0_3 & 0_3 & 0_3 \\ 0_3 & 0_3 & S_g I_3 & 0_3 & 0_3 \\ 0_3 & 0_3 & 0_3 & S_{ba} I_3 & 0_3 \\ 0_3 & 0_3 & 0_3 & 0_3 & S_{bg} I_3 \end{bmatrix} \tag{2.23}$$

where 0_3 is a 3×3 matrix of zeros and I_3 is the 3×3 identity matrix. Scalars, S_a, S_g, S_{ba}, and S_{bg} are the power spectral densities (PSDs) of accelerometer noise, gyro noise, accelerometer bias noise, and gyro bias noise, respectively. While true PSDs vary with frequency, these approximate values do not include this variation. This assumption is made because the Kalman filter assumes that all noise sources are white. The values of these parameters as defined in [14] are:

$$S_a = \sigma_a^2 dt \qquad S_g = \sigma_g^2 dt \tag{2.24}$$

where dt is the mechanization time-step, σ_a is the standard deviation of the noise on the accelerometer measurements and σ_b is the standard deviation of the noise on the gyro measurements. The spectral densities on the biases are:

$$S_{ba} = \frac{\sigma_{ba}^2}{\tau_{abias}} \qquad S_{bg} = \frac{\sigma_{bg}^2}{\tau_{gbias}} \tag{2.25}$$

where σ_{ba} and σ_{bg} are the standard deviations of the driving noise on the accelerometer and gyro biases respectively and τ_{abias} and τ_{gbias} are the time constants associated with the Gauss-Markov processes modeling the accelerometer bias and gyro bias respectively. Note

that this process noise matrix must still be discretized by Equation 2.8 if a discrete algorithm is being used.

2.2.2 Exteroceptive Sensor Models

The cooperative vehicle-to-vehicle (V2V) measurements used in this thesis include relative range, range-rate, and bearing. There are various on-board, exteroceptive sensors that can be equipped to small UAVs that make each of these measurements possible. Range and range-rate can be measured by radar, laser scanners, ultra-wide-band (UWB) radios, or other transponder-based techniques [11]. Range and/or range-rate measurements were used for cooperative navigation in [11, 31, 38]. Relative bearing can be determined by visual methods, LIDAR, radar, or other multi-antenna, angle-of-arrival estimation algorithms such as Multiple Signal Classification (MUSIC). Relative bearing measurements have been used in cooperative navigation in [6, 24, 36].

All three of these relative measurements (range, range-rate, and bearing) are mathematically modeled by nonlinear functions of the vehicle states. Inter-vehicle range measurements are modeled by:

$$\rho_{ij} = \sqrt{\Delta P_N^2 + \Delta P_E^2 + \Delta P_D^2} + \eta_\rho \tag{2.26}$$

where ρ_{ij} is the range measurement from vehicle i to vehicle j, $\Delta P_N, \Delta P_E$, and ΔP_D represent the difference in North, East, and Down position respectively between the two vehicles, and η_ρ represents zero mean, Gaussian measurement noise with standard deviation σ_ρ. Inter-vehicle range-rate measurements are modeled by:

$$\dot{\rho_{ij}} = \frac{\Delta P_N \Delta V_N + \Delta P_E \Delta V_E + \Delta P_D \Delta V_D}{\rho_{ij}} + \eta_{\dot{\rho}} \tag{2.27}$$

where $\dot{\rho_{ij}}$ is the range-rate measurement and $\Delta V_N, \Delta V_E$, and ΔV_D represent the difference in North, East, and Down velocity respectively between the two vehicles. Inter-vehicle bearing

is broken into separate azimuth and elevation components [5]. Azimuth is modeled by:

$$\Lambda_{ij} = \arctan(\frac{\Delta P_N}{\Delta P_E}) - \psi_i + \eta_\Lambda \tag{2.28}$$

where Λ_{ij} is the azimuth measurement and ψ_i is the yaw angle of vehicle i [36]. Elevation is modeled as:

$$E_{ij} = \arctan(\frac{-\Delta P_D}{\sqrt{\Delta P_N^2 + \Delta P_E^2}}) - \theta_i + \eta_E \tag{2.29}$$

where E_{ij} is the elevation measurement and θ_i is the pitch angle of vehicle i.

Absolute measurements are allowed to certain vehicles in a few of the simulated cooperative navigation scenarios. GPS measurements give *absolute* position information as opposed to the *relative* information given in Equations 2.26-2.29. GPS measurements are modeled as:

$$\boldsymbol{P}_{meas} = \boldsymbol{P} + \boldsymbol{\eta}_{GPS} \tag{2.30}$$

where $\boldsymbol{P}$ is the 3x1 vector of NED position coordinates of a vehicle, and $\boldsymbol{\eta}_{GPS}$ is a 3x1 vector of zero-mean, Gaussian random variables with standard deviation σ_{GPS}. While this is a simplistic model for GPS measurement information, it is sufficient for this thesis. Additionally, absolute attitude information is allowed to certain vehicles in a few of the simulated cooperative navigation scenarios. This information is assumed to come from an attitude heading reference system (AHRS) that combines information from the GPS receiver along with gyro, accelerometer, and magnetometer sensors to compute absolute vehicle attitude. An AHRS design of this type is presented in [12, 14]. The measurement model used in this thesis for this device is:

$$\boldsymbol{\Psi}_{meas} = \boldsymbol{\Psi} + \boldsymbol{\eta}_{AHRS} \tag{2.31}$$

where $\boldsymbol{\Psi}$ is the 3x1 vector of Euler angles describing the attitude of the given vehicle, and $\boldsymbol{\eta}_{AHRS}$ is a 3x1 vector of zero-mean, Gaussian random variables with standard deviation σ_{AHRS}. Digital elevation models provide the vertical elevation of points on the Earth's

surface. The US Geological Survey (USGS) provides free access to various elevation models, collected from a variety of sources, on their website (www.usgs.gov). Since UGVs operate on the surface of the Earth, they can use these models to obtain absolute vertical positioning information for their estimated location. In this work, digital elevation measurements are modeled as:

$$P_{DEM} = P_{Dt} + \eta_{DEM} \tag{2.32}$$

where P_{DEM} is the measured vertical position from the DEM, P_{Dt} is the true position of the UGV in the down (vertical) direction, and η_{DEM} is Gaussian random noise with standard deviation σ_{DEM}.

The measurement covariance matrix, R, is formed as a diagonal matrix from the error characteristics of the individual measurements.

$$R = \begin{bmatrix} \sigma^2_{meas\,1} & & \\ & \ddots & \\ & & \sigma^2_{meas\,m} \end{bmatrix} \tag{2.33}$$

Where $\sigma_{meas\,i}$ is the standard deviation of the noise on the ith measurement.

2.3 Centralized Cooperative Navigation Algorithm (EKF)

The Extended Kalman Filter (EKF) is a modification of the Kalman filter algorithm (given in Equations 2.9 - 2.13) for nonlinear systems of the form:

$$\dot{x} = f(x, u) + w \tag{2.34}$$

$$y = h(x) + \eta \tag{2.35}$$

where $f(x, u)$ is a $n \times 1$ set of nonlinear state equations as a function of the states, x, and inputs, u, w is the $n \times 1$ stochastic error input which is assumed to be Gaussian and zero-mean, y is the $r \times 1$ output, $h(x)$ is the $r \times n$ set of nonlinear measurement equations as a function of the states, x, and η is the $r \times 1$ stochastic measurement error which is also assumed to be Gaussian and zero-mean. w and η are again characterised by the covariance matrices Q and R, respectively.

The centralized cooperative filter state is constructed by combining each individual vehicle's state into a single state vector:

$$\boldsymbol{x}_{centralized} = \begin{bmatrix} \boldsymbol{x}_1 \\ \boldsymbol{x}_2 \\ \dots \\ \boldsymbol{x}_i \end{bmatrix} \tag{2.36}$$

For cooperative navigation with two vehicles Equation 2.36 will be a 30×1 state vector, for three vehicles this is a 45×1 state vector, etc.

A block diagram describing the centralized cooperative navigation architecture is shown in Figure 2.3. Each of the vehicles passes IMU data along with inter-vehicle measurements

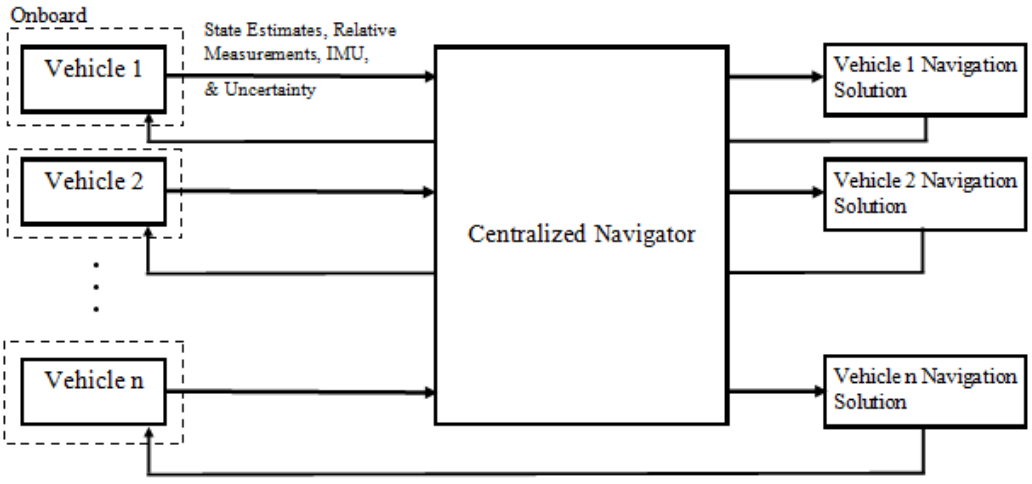

Figure 2.3: Centralized Cooperative Navigation Block Diagram

(as available) to a centralized processor. This centralized navigator could be located on one of the vehicles or on some type of supporting infrastructure. The centralized navigator processes and fuses this information from all of the vehicles as described above and re-transmits each vehicle's navigation solution back to that vehicle. Note that the centralized processor must handle receiving, processing, and re-transmitting all of the data for all of the cooperating vehicles. Depending on the number of vehicles in the cooperative group, this task could require a high computational and communicational bandwidth.

Both the 6-DOF IMU mechanization (Equations 2.18-2.19) used for the time update portion of the algorithm and the measurement update equations (Equations 2.26-2.31) are nonlinear functions of the state and input. Therefore, the EKF will be used as the basis of the centralized cooperative navigation algorithm. The EKF differs from the standard Kalman Filter (Equations 2.9-2.13), in that the nonlinear system is linearized in order to be used in the algorithm. The steps of the time update of this modified algorithm are as follows:

1. propagate state estimates forward using *nonlinear* state equations, $\dot{x} = f(x, u)$.

2. Calculate linearized state matrix, A. Each element of the state matrix is determined by calculating the Jacobian and evaluating at the current operating point. See Appendix A for a detailed calculation of matrix A for this system.

$$A_{i,j} = \frac{\partial f_i}{\partial X_j} \tag{2.37}$$

3. Discretize the state transition matrix by Equation 2.5.

4. Propagate the state covariance matrix by Equation 2.10.

This time update is repeated until measurements become available. When measurements become available, the measurement update step can be performed as follows:

1. Calculate linearized measurement matrix, H. This matrix is the Jacobian of the non-linear measurement equations evaluated at the current operating point. See Appendix A for a detailed calculation of matrix H.

$$H_{i,j} = \frac{\partial h_i}{\partial X_j} \tag{2.38}$$

2. Calculate the Kalman gain, K, by Equation 2.11, using the linearized H matrix.

3. Calculate the *a posteriori* state estimate using the nonlinear measurement equations, $h(x)$:

$$x_{k+1}^{+} = x_{k+1}^{-} + K(y - h(x_{k+1}^{-})) \tag{2.39}$$

4. Calculate the *a posteriori* covariance matrix, P_{k+1}^{+}, using Equation 2.13.

As mentioned in Chapter 1, one of the goals of this thesis is to compare centralized and decentralized estimation architectures for cooperative navigation. The centralized architecture is described as being "optimal" from an information theory point of view in [20]. This is because one of the main advantages of this architecture is that all of the inter-vehicle state cross-covariance values are kept track of in the centralized covariance matrix, P. For a centralized cooperative navigation scenario with three vehicles, this covariance matrix can be described as:

$$P_{centralized} = \begin{bmatrix} P_{11} & P_{12} & P_{13} \\ P_{21} & P_{22} & P_{23} \\ P_{31} & P_{32} & P_{33} \end{bmatrix} \tag{2.40}$$

where P_{ii} is the 15×15 covariance matrix correlating vehicle i states to themselves and P_{ij} is the 15×15 covariance matrix correlating vehicle i states to vehicle j states. In cases where no inter-vehicle cooperation exists, the off-diagonal covariance values are zero. However,

the inter-vehicle correlation is non-zero if there is any form of cooperative aiding. The off-diagonal covariance correlations are important when processing relative measurements that are functions of multiple vehicle's states.

Zero inter-vehicle correlation indicates that any measurement made between the two vehicles is completely new information and should be weighted accordingly in the measurement update step. However, non-zero inter-vehicle correlation indicates that that measurements made between the two vehicles do not contain new or unique information. Due to the nature of the cooperative navigation problem, these inter-vehicle correlations grow as more cooperative measurements are processed and the vehicle state estimates become more tightly coupled [19].

Figure 2.4 illustrates the basic problem in cooperative navigation. Cooperative measurements with associated uncertainties, R, are taken between cooperating vehicles whose states also have an associated uncertainty, P. If a centralized estimation approach is taken, each of these uncertainties is optimally accounted for so that when the measurement update occurs, it is optimally weighted taking all uncertainties into consideration. Note that while for linear systems, this solution can be said to be optimal, for nonlinear systems a globally optimal solution cannot usually be guaranteed.

Weighting of the measurement based on associated uncertainties can be seen in the calculation of the Kalman gain in Equation 2.11. The numerator of this equation can be said to represent the *a priori* state uncertainty, while the denominator of this equation represents the total uncertainty associated with the measurement, including both the measurement uncertainty, R, and the uncertainty of the states about which the measurement is made, HPH^T.

To further understand this weighting, it is useful to look at two edge cases in regard to these uncertainties. In the case of a perfect measurement, $R = 0$, Equation 2.11 reduces to $K = H^{-1}$. Plugging this Kalman gain into Equation 2.12, the updated state is calculated

as $\hat{x}^+ = H^{-1}y$. This indicates that the updated state estimate is solely based on the measurement and that the previous estimate is neglected. In the case of a perfect *a priori* state estimate, the Kalman gain is calculated as $K = 0$. Plugging this Kalman gain into the state update equation results in $\hat{x}^+ = \hat{x}^-$. The new measurement is completely ignored because the already perfect state estimate cannot be improved by adding any further information. While neither of these two edge cases would ever happen in reality, they do provide insight into how this algorithm is able to fuse cooperative measurements with state estimates in the centralized case.

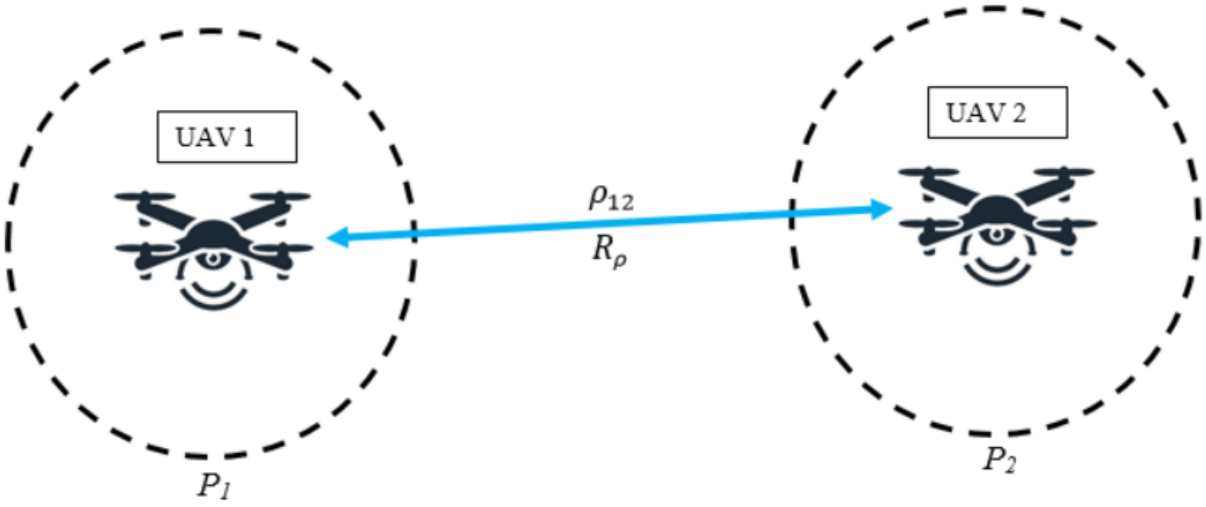

Figure 2.4: Uncertain measurement, ρ_{12}, taken between two UAVs with uncertain estimated states with covariances P_1 and P_2

2.4 Decentralized Cooperative Navigation Algorithm (CI)

Now that the centralized algorithm has been outlined, the additional challenges involved in the decentralized implementation can be discussed. For decentralized cooperative navigation with three vehicles, the covariance matrices that can be tracked are:

$$P_{vehicle1} = \left[P_{11}\right], P_{vehicle2} = \left[P_{22}\right], P_{vehicle3} = \left[P_{33}\right] \tag{2.41}$$

Comparing Equations 2.41 and 2.40, it can be seen that a decentralized cooperative navigation system cannot calculate inter-vehicle state correlations, P_{ij}, that a centralized algorithm can calculate directly. This is because each vehicle separately estimates its own navigation state in the decentralized case. Therefore, the convenient mathematical properties that the centralized EKF uses to fuse inter-vehicle measurements cannot be used in the decentralized case.

To use an EKF in a decentralized manner would lead to a violation of one of the key assumptions made in the Kalman Filter derivation, that the *a priori* state and the measurement errors are independent. In this case, each relative measurement update would be counted as completely new information, and the growing inter-state correlation between cooperating vehicles would be completely neglected. If neglected, this violation can lead to filter divergence and error loops that can amplify state estimation errors [19]. To combat this unknown correlation issue, alternative algorithms must be considered for the decentralized case.

In the literature, the most widely cited algorithm to correct for this problem in cooperative navigation is the Covariance Intersection (CI) filter [19, 20, 21, 43]. The Covariance Intersection filter was first introduced in [17]. This filter is based on the standard Kalman filter, but contains additional steps to account for unknown inter-state correlations. The time update step of this algorithm is the exact same as the EKF time update. The difference in the algorithm is in the measurement update step. The measurement update of the CI filter is given as follows:

1. Calculate linearized measurement matrix, H, as in Equation 2.38.

2. Inflate measurement covariance elements.

$$R_i = R_i + H_j P_{jj} H_j^T \tag{2.42}$$

where R_i is the uncertainty of the measurement from vehicle i to vehicle j, H_j is vehicle j's measurement matrix associated with that measurement, and P_{jj} is vehicle j's state covariance matrix. This step should be performed separately for each individual cooperative measurement, with the vehicle i's final measurement covariance, R, being composed of all R_i terms, combined in a block-diagonal fashion.

3. Define a cost function, J.

$$J(\omega) = \text{trace}\left\{ \left(\omega(P_{k+1}^{-})^{-1} + (1-\omega)H^T R^{-1} H \right)^{-1} \right\} \tag{2.43}$$

4. Find ω^* that minimizes J for $\omega \in [0, 1]$. The MATLAB function $fminbnd()$ was used to perform this calculation in this work.

5. Calculate the *a posteriori* covariance estimate.

$$P_{k+1}^{+} = (\omega^*(P_{k+1}^{-})^{-1} + (1-\omega^*)H^T R^{-1} H)^{-1} \tag{2.44}$$

6. Calculate the Kalman Gain.

$$K = (1-\omega^*)P_{k+1}^{+} H^T R^{-1} \tag{2.45}$$

7. Update the state estimate according to Equation 2.39.

Performing this algorithm on a model with more than just a few states can result in the algorithm greatly under-weighting the effect of the measurement updates. This is especially true when the values modeled by different states have different units as stated by Mokhtarzadeh in [19]. This is the case here, as each vehicle has 15 states with five different types of units among those states. To mitigate this effect, Mokhtarzadeh notes that it may be necessary to perform a scaling on the states and covariances or use non-"optimal" ω^* values. These scalings are often done heuristically, based on engineering judgement, and

may not be robust to various scenarios and applications. This can be a major drawback of this technique. See [19] for a more detailed discussion of these issues.

When comparing the calculation of the Kalman gain for the centralized and decentralized algorithms, Equations 2.11 and 2.45, two main differences can be observed. First, for the centralized algorithm, the HPH^T term in Equation 2.11 represents the state uncertainty of the full system, including all vehicles and all inter-vehicle correlations. For the decentralized algorithm, the measurement uncertainty is inflated by a similar $H_j P_{jj} H_j^T$ term. This term represents the additional measurement uncertainty due to the fact that the measurement is made to a vehicle with an uncertain state and does not include any information regarding inter-vehicle state correlations. In order to account for the unknown covariance information, an extra term, ω^*, is introduced into the measurement update equations. This term is present in the calculation of the decentralized Kalman gain in Equation 2.45 and is not seen in the standard Kalman filter, in Equation 2.11.

To further investigate this, two edge cases for ω^* in Equation 2.45 will be explored in the same way that two edge cases were previously explored for Equation 2.11. In the case where $\omega^* = 0$ minimizes the cost function in Equation 2.43 and this value is plugged into Equations 2.44 and 2.45, the Kalman gain simplifies to $K = H^{-1}$. As previously discussed, this Kalman gain corresponds to perfect trust of the updating measurement. In the case where $\omega^* = 1$ minimizes the cost function, the Kalman gain simplifies to $K = 0$, or zero weighting of the measurement update. This ω^* term allows the algorithm to fuse measurements where unknown correlations exist between cooperating vehicle states without the advantage of the mathematical properties that automatically account for these correlations in centralized EKF cooperative navigation. In other words, this term provides a method to systematically "tune" the level at which the measurement is weighted in the state update.

A block diagram describing the decentralized cooperative navigation architecture is shown in Figure 2.5. Each of the vehicles passes IMU data along with inter-vehicle measurements (as available) to a decentralized processor. This decentralized navigator would

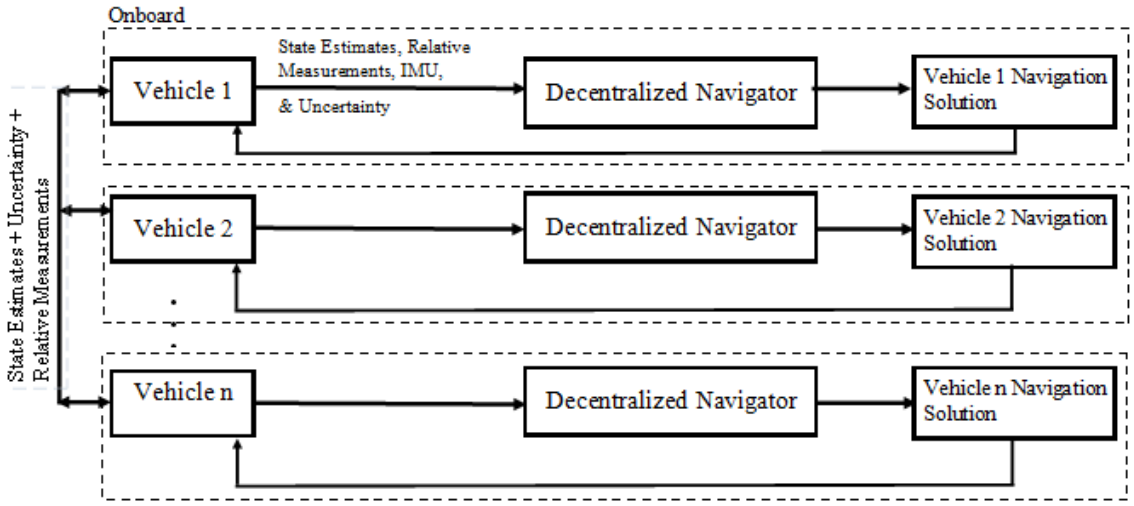

Figure 2.5: Decentralized Cooperative Navigation Block Diagram

typically be located on the vehicle itself. The navigator processes and fuses this information as described above and calculates the vehicle's navigation solution. The fact that this takes place on each vehicle reduces the amount of information that must be received, processed, and sent by any single processor, thus "distributing" the estimation process.

2.5 Filter Tuning

One last consideration that should be made concerning the practical application of these algorithms is filter tuning. In certain cases, especially for nonlinear systems or when process or sensor error characteristics are not fully known, the filter performance can be improved by scaling the values of the process and measurement covariance matrices, Q and R. Low $\frac{Q}{R}$ ratios will result in a slow responding filter with a high amount of lag that easily filters out noise. In system response terms, this filter has a low bandwidth. High $\frac{Q}{R}$ ratios will result in a filter that responds very quickly with very little lag, but is filters out noise poorly. This filter has a high bandwidth. In practical application, this ratio should be tuned in order to provide a balance between response speed and filtering. Additionally, for nonlinear systems, the initialization of the state estimate covariance matrix, P, can have an impact on estimator performance.

Figure 2.6 shows the estimation of a gyroscope bias for different filter tuning ratios. Because the measurement update is weighted more heavily in cases with a high $\frac{Q}{R}$, this could result in a biased or even an unstable filter if the measurement noise has too great of an effect on the estimation solution.

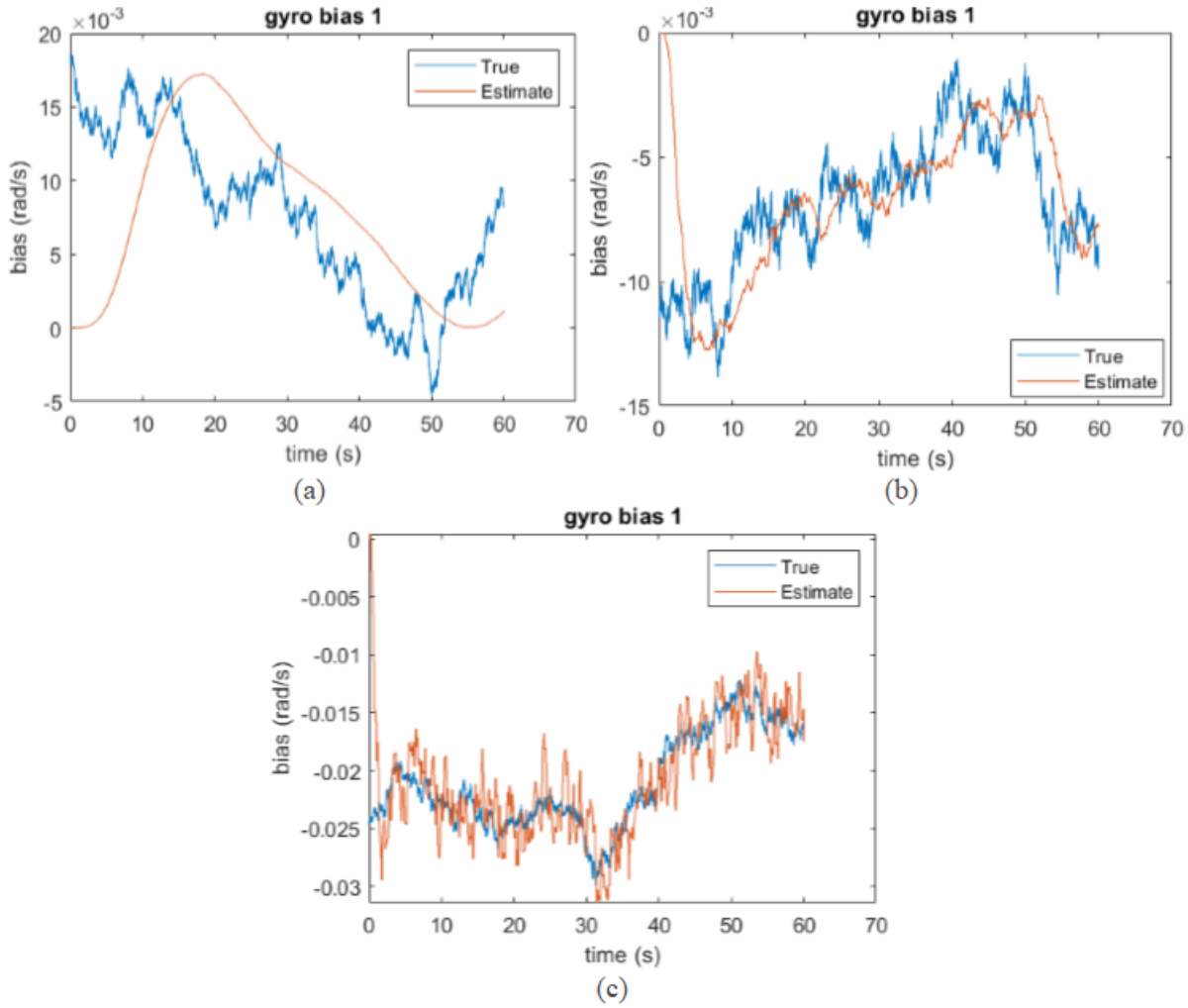

Figure 2.6: Filter Tuning: Gyro Bias Estimation (a)Q/R too low (stable but slow response) (b)Reasonable Q/R (c)Q/R too high (fast response but high noise and potential instability)

It is often necessary in practice to inflate the process or measurement noise covariance matrices above the corresponding error deviations [14]. This is because the filter's model of the system is only an approximation of the real system. This is especially true in cooperative navigation scenarios where the true states are not fully observable and the filter solution

cannot converge to true values. As the estimated solution drifts from the true solution, filter instability can result if care is not taken to tune these covariance values. This is also important for nonlinear systems such as the cooperative navigation algorithms studied in this work, as the linearization accuracy can begin to break down as the estimate drifts farther away from the true state. It can become necessary to tune $\frac{Q}{R}$ much lower than sensor error parameters indicate to prevent instability. The tuning process is typically done heuristically, by hand, and care should be taken in simulation to ensure the adequate performance of the selected tuning parameters.

2.6 Conclusion

This chapter introduced the centralized and decentralized cooperative navigation algorithms that are implemented later in this thesis. The kinematic vehicle model and navigation frame considerations were also discussed along with the measurement models used here. Lastly, general considerations such as inter-vehicle state correlations and filter tuning were discussed.

Chapter 3

Observability Analysis

One of the most important factors for the estimation algorithms introduced in Chapter 2 to obtain accurate estimates of the model states is state observability. Observability can be described as the phenomenon of being able to estimate the state of a model based on the measured outputs over a finite time window. In mathematical terms, given a system of the form Equation 2.1 and Equation 2.2, the system is observable at t_0 if the output history, $y(t)$, $t_0 \leq t \leq t_f \leq \infty$, is sufficient to reconstruct $x(t_0)$ [40].

3.1 Linear Observability Analysis

Linear system observability analysis is a well studied problem with relatively simple solutions. For a detailed discussion of these methods, see [4, 40].

3.1.1 Linear Observability Matrix

Perhaps the simplest method to analyze the observability of linear, time-invariant systems is by constructing the linear observability matrix. As seen in Equation 3.1, this matrix is a function of the linear state dynamics in the state matrix (A), and the measurement matrix (H). Here, n is the number of state variables.

$$O = \begin{bmatrix} H \\ HA \\ HA^2 \\ \cdots \\ HA^{n-1} \end{bmatrix} \tag{3.1}$$

The observability matrix, O, has full rank (n), if and only if the the model is observable.

3.1.2 Linear Observability Gramian

The linear observability Gramian can be applied to analyze the observability of linear, time-varying systems. Stengel [40] gives the observability Gramian matrix as:

$$O_{LOG}(t_0, t_f) = \int_{t_0}^{t_f} \Phi(t_0, \tau)^T H(\tau)^T H(\tau) \Phi(t_0, \tau) d\tau \tag{3.2}$$

Here, $O_{LOG}(t_0, t_f)$ is the linear observability Gramian from time t_0 to t_f and $\Phi(t_0, \tau)$ is the state transition matrix from time t_0 to τ. The system is observable if and only if the linear observability Gramian is non-singular. Additionally, if $O_{LOG}(t_0, t_f)$ is full rank (n), then it is also non-singular and the system is fully observable over the time period t_0 to t_f. While this matrix is formed for analysis of linear systems, it can also be used to analyze linearized nonlinear systems.

3.2 Nonlinear Observability Analysis

Determining the observability of a nonlinear system is less straightforward than determining the observability of a linear system. Herman and Krener's landmark paper [15] introduced important definitions and methods of analysis for nonlinear observability. In that paper, nonlinear systems observability is described as either *locally* observable, *weakly* observable or *locally weakly* observable. Formal definitions of these observability conditions are given in [15, 44]:

Definition 3.1 *A system is locally observable at x_0 if for every state in the neighborhood U of x_0 the set of points indistinguishable from x_0 by trajectories in U only consists of x_0 itself.*

Definition 3.2 *A system is weakly observable at x_0 if there exists an open neighborhood U of x_0 such that the only point in U that is indistinguishable from x_0 is x_0 itself.*

Definition 3.3 *A system is locally weakly observable at x_0 if there exists an open neighborhood U of x_0 such that for every open neighborhood V of x_0 contained in U, the set of points indistinguishable from x_0 by trajectories in V is x_0 itself.*

While it can be difficult to prove local and weak observability characteristics of a nonlinear system, local weak observability lends itself to an algebraic test based on the Lie derivative [15] that is shown in Section 3.2.1 of this thesis. Furthermore, even if nonlinear system states are not observable, they may be *partially* observable [14]. For example, a range measurement, represented by Equation 2.26 is a nonlinear combination of 3 states. Therefore, although all three of these states are not fully observable given a single range measurement, all three of the states may be partially observed. The degree at which each of these states is observed by this single measurement depends on the relative geometry of the two points that the range measurement is being taken between.

A state can be considered *well* observable if the measurement output changes significantly with small perturbations of that state. A state is *poorly* observable if a large perturbation of the state results in only a small change in measured output [26]. As Groves states in [14], "the position information along a given axis obtainable from a given ranging signal is maximized when the angle between that axis and the signal line of sight is minimized." If a range measurement is taken from any direction that is not aligned exactly with one of the coordinate axes or planes all three of the relative distances will be made partially observable. If a range from any point can be determined to three known points, the full 3-D position of that point is observable and can be calculated by trilateration.

One nonlinear observability analysis method is to linearize the system and perform a linear observability analysis [32, 30]. The simplicity of this method makes it an attractive option. Additionally, the linearized forms of the state matrix (A) and the measurement matrix (H) must already be computed for the estimation algorithm. However, this linearization makes the observability results local to the trajectory about which the system is linearized,

and no implications can be made about the observability of the system as a whole. It is important to note that the linearization should be performed about the *true* state rather than the estimated state [32]. This is because the purpose of this analysis is to determine whether or not a certain UAV maneuver results in an observable (or more observable) system.

3.2.1 Lie Derivative Observability Analysis

The Lie derivative method of determining nonlinear observability was introduced in [15]. This test is necessary and sufficient to demonstrate that a system is locally weakly observable. This method is applied to a system of the form described in Equations 2.1 and 2.2. The Lie derivatives of the system are taken as follows:

$$\mathscr{L}_f^0 h(x) = h(x) \tag{3.3}$$

$$\mathscr{L}_f^1 h(x) = \frac{\partial h(x)}{\partial x} \cdot f(x) \tag{3.4}$$

$$\mathscr{L}_f^2 h(x) = \frac{\partial \mathscr{L}_f^1 h(x)}{\partial x} \cdot f(x) \tag{3.5}$$

Higher order Lie derivatives are computed similarly. From these Lie derivatives, the observability matrix, O, is constructed.

$$O = \begin{bmatrix} \nabla \mathscr{L}_f^0 h(x) \\ \nabla \mathscr{L}_f^1 h(x) \\ \cdots \\ \nabla \mathscr{L}_f^{n-1} h(x) \end{bmatrix} \tag{3.6}$$

When applied to linear, time-invariant systems, this method reduces to the linear observability matrix described in Equation 3.1. Multiple authors have applied this method to analyze various cooperative navigation scenarios [37, 44, 2, 8]. However, because of the time-variant nature of the cooperative navigation scenarios to be investigated, an alternative

formulation of this observability matrix will be used in this work. This alternative observability matrix is also constructed in discrete time, which is more in line with the discrete filtering algorithms being used. This alternative formulation is calculated as:

$$O = \begin{bmatrix} \frac{\partial h(x(k))}{\partial x} \\ \frac{\partial h(x(k+1))}{\partial x}\Phi(k,k+1)) \\ \cdots \\ \frac{\partial h(x(t_f))}{\partial x}\Phi(k,t_f)) \end{bmatrix} \tag{3.7}$$

where $\Phi(k,\tau)$ represents the state transition matrix from time k to τ. The same rank condition can be applied to this matrix to test for system observability. This implementation was used in [7, 8]. Again, the similarity between this implementation and the linear observability matrix in Equation 3.1 should be noted. This method is also advantageous when the cooperative network topology is switching and not fixed as in [7, 8]. The network topology in this paper is assumed to be fixed in a fully connected manner. Another factor that makes this method attractive is its simplicity of implementation.

3.2.2 Empirical Observability Gramian Analysis

The construction of an *empirical* observability Gramian has also been suggested as a way to analyze the observability of nonlinear systems [27, 25, 26]. In this method, each state value is perturbed by some pre-defined amount, ϵ, in both a positive and negative direction and the change in output, Δy, is calculated.

$$\Delta y_i = h(x + \epsilon \boldsymbol{e}_i) - h(x - \epsilon \boldsymbol{e}_i) \tag{3.8}$$

where $\boldsymbol{e}_i$ are the standard basis vectors in $\mathbb{R}^n$, and Δy_i is the change in measurement caused by perturbing the ith state. The simulated, "ideal" measurements, with no noise or bias, are used in this analysis. A modified form of the empirical observability Gramian is used in this

thesis which includes the state transition matrix, Φ. This allows for observability analysis of states that are not directly observed by the measurements but are coupled to observed states through the model dynamics. Using these output differences and the state transition matrix, the empirical local observability Gramian can be calculated :

$$O_{EOG} = \int_{t_0}^{t_f} \Phi(t_0, \tau)^T [\Delta y_1 ... \Delta y_n]^T [\Delta y_1 ... \Delta y_n] \Phi(t_0, \tau) d\tau \tag{3.9}$$

Comparing Equation 3.9 and 3.2, it can be seen that the calculation of this empirical observability Gramian is very similar to the calculation of the linear observability Gramian. The empirical observability Gramian, however, eliminates the need to calculate Jacobian of the nonlinear measurement equations to get the measurement matrix, H. The empirical calculation of Δy_i using the nonlinear measurement models takes the place of the Jacobian matrix H. In cases with highly nonlinear measurements, this method can give more accurate results because the nonlinearities in the measurement model are approximated more accurately using this empirical method than by the linearized (Jacobian) method. The state transition matrix must still be calculated by linearization when using this method.

3.3 Cooperative Navigation Observability Tests

The concept of observable *states* and observable *modes* is discussed in [32]. In the case of a 30×30 observability matrix with a rank of rank 26, this rank deficiency indicates that the system has 26 observable modes and 4 unobservable modes. This is not the same thing as a system with 26 observable states and 4 unobservable states. Modes may be states or functions of states. Therefore, even though there may be 26 observable modes, some of these modes may be combinations of states. It may not be possible for the filter to separate 26 observable, individual states out of 26 observable modes. One major limitation in using the observability rank test is that this test only gives a binary yes/no answer to the question of observability [27]. As mentioned earlier, nonlinear observability can be very complex

and even if the full system is not completely observable, the system may still be partially observable. For these reasons, it is desirable to apply a method that indicates some metric of the quality of observability of each state.

So far, four methods to construct different forms of observability matrices have been presented:

1. Linear Observability Matrix
2. Linear Observability Gramian
3. Nonlinear Lie derivative Observability Matrix
4. Nonlinear Empirical Observability Gramian

A matrix rank test has been suggested to analyze the observability of each matrix. This rank test, however, provides little more information than a binary yes or no to system observability. Since the cooperative navigation problem in question has inherent observability problems and is not fully observable in most cases, a method to provided further, qualitative information of state observability is desired. One such method described in [2, 26] is to consider the condition number of the observability matrices. The condition number, C, of a matrix is the ratio of its largest singular value to its smallest singular value.

$$C = \frac{\sigma_{max}}{\sigma_{min}} \tag{3.10}$$

Where σ_{max} and σ_{min} are the largest and smallest singular values of a matrix respectively. The condition number can be calculated in MATLAB using the function *cond()*. This condition number also indicates the sensitivity of the matrix inverse operation to small changes in input. As previously discussed, high sensitivity to small changes in input (i.e. low condition number) represents good system observability. Matrices with condition numbers that are close to 1 are considered well conditioned and invertible. Systems with well conditioned observability matrices are considered more observable than systems with higher condition

numbers. An unobservable system's observability Gramian condition number will approach ∞ and will not be invertible.

This qualitative test of observability still does not fully solve the issue of analyzing the observability of a cooperative navigation scenario with some unobservable states, as the presence of even one unobservable state will result in a condition number that approaches ∞. To examine the observability of a subset of system states, a sub-matrix of the overall observability Gramian matrix corresponding to the desired states can be extracted and analyzed [26]. For example, since the NED position of UAV 1 are the first 3 states in Equation 2.20, the first 3×3 block diagonal matrix in the resulting observability Gramian can be used to analyze the observability of these states. In cases where an absolute position update (eg. GPS) is available to UAV 1, the resulting condition number of this observability Gramian sub-matrix is 1. This is the expected result, as the GPS measurement makes the UAV position fully observable.

3.4 Dilution of Precision

Dilution of Precision (DOP) is a concept that is closely related to the observability concepts discussed thus far. DOP is a parameter that is typically used to quantify the effect of satellite-receiver geometry on the quality of the GNSS position, velocity, and timing (PVT) estimates. In this thesis, DOP will be calculated between cooperating vehicles and used to analyze the quality of cooperative navigation estimation. DOP is calculated by Equation 3.11.

$$DOP = (H^T H)^{-1} = \begin{bmatrix} D_{x1}^2 & & \\ & \ddots & \\ & & D_{xn}^2 \end{bmatrix} \tag{3.11}$$

where H is the measurement matrix and D_{xi} is the DOP value corresponding to the ith state. These DOP values are then used to calculate the uncertainty of a given state as a

function of measurement uncertainty by Equation 3.12.

$$\sigma_{xi} = D_{xi}\sigma_{meas} \tag{3.12}$$

High DOP values correspond to poor quality state estimates (poor observability) while low DOP values correspond to high quality state estimates (good observability).

where σ_{xi} is the standard deviation of the uncertainty of the ith state and σ_{meas} is the standard deviation of the measurement uncertainty. Position dilution of precision (PDOP) can be analyzed as a whole by combining the DOP values from each position direction as in Equation 3.13.

$$D_P = \sqrt{D_N^2 + D_E^2 + D_D^2} \tag{3.13}$$

where D_P is the PDOP, D_N, D_E, and D_D are the DOP in the north, east, and down directions respectively.

3.5 UAV Maneuvers to Improve Observability

As suggested in [6, 7, 29, 31, 34, 38], relative UAV geometry and maneuver can be used to improve the observability and subsequently the state estimation accuracy in cooperative navigation systems. A range measurement taken from different relative orientations in 3-D space can give information on any of the three relative position states. If this relative orientation is varied in time, then different parts of the relative position can be observed as the relative orientation changes. This same phenomenon also holds true for range-rate and relative bearing measurements if the vehicles are equipped with sensors to measure these parameters. For this reason, a UAV maneuver that allows for a constantly changing relative orientation is desired. In [2], Arrichiello describes the condition where the relative position and velocity vectors between two vehicles are orthogonal and have the same magnitude as having optimal observability characteristics (the condition number of the observability Gramian is minimized).

The simplest way to generate this type of motion is a maneuver in which cooperating UAVs are guided in "spiral" paths around a common center. Similarly, [7] shows that for small robots operating in a planar environment, circular robot paths result in reduced estimation error. Increasing the frequency of this circling resulted in further improvements in estimation accuracy. Moreover, [31] also states that sinusoidal trajectories improve navigation accuracy over straight trajectories for vehicles navigating with an IMU and camera, and that further improvements can be made by increasing the frequency and amplitude of the oscillations. Motivated by these results, "spiral" trajectories of varying frequency will be investigated to determine their effect on observability and estimation accuracy in cooperative navigation. Figure 3.1 shows a comparison of straight UAV paths, low frequency spiral UAV paths, and high frequency spiral UAV paths. To maintain a safe distance between UAVs, a spiral radius of 20 meters is maintained in this work.

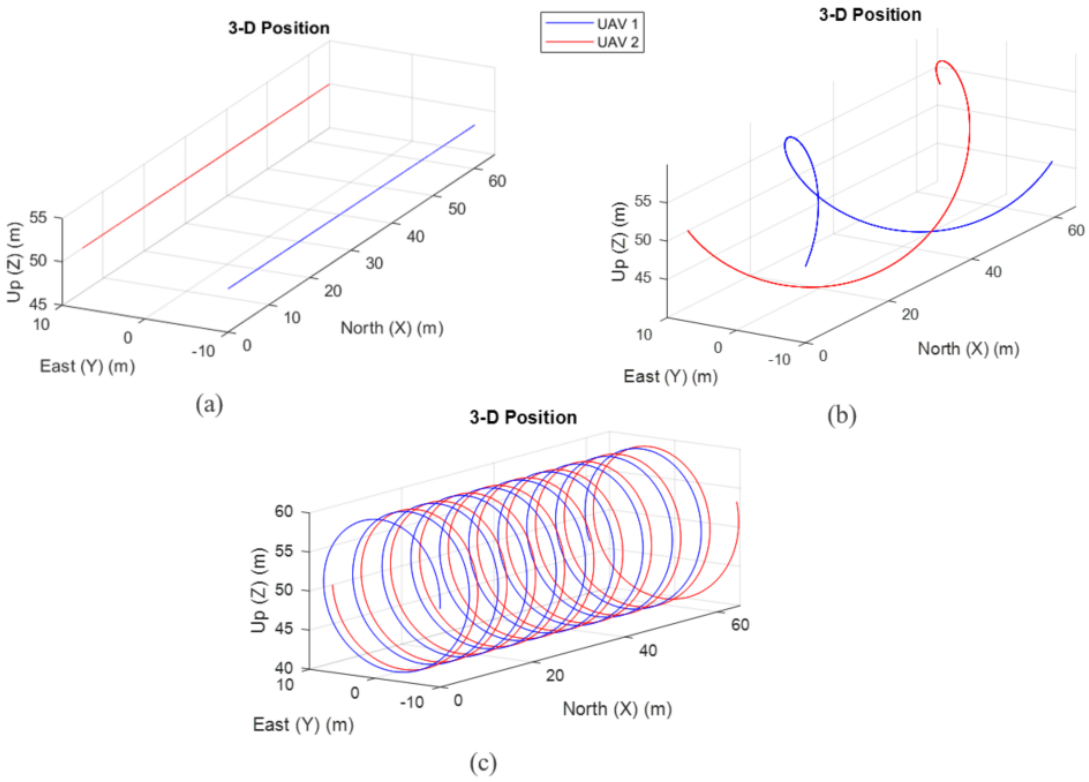

Figure 3.1: UAV Spiral Maneuvers: (a) straight path, (b) low frequency spiral path, and (c) high frequency spiral path

3.6 Observability Simulations

Simulations of various cooperative navigation scenarios undergoing a 60 second GPS outage were performed in order to analyze their observability characteristics. As previously noted, it is important to perform these observability analyses over the true vehicle trajectory, not over the estimated trajectory. First, a comparison of multiple analysis methods was performed to validate the methods for this system. Figure 3.2 shows the results of the observability rank test and the observability Gramian condition number test performed on a scenario where 2 UAVs performing a spiral maneuver at 1 revolution per minute had access to relative range, range-rate, and bearing measurements. As can be seen in the rank test

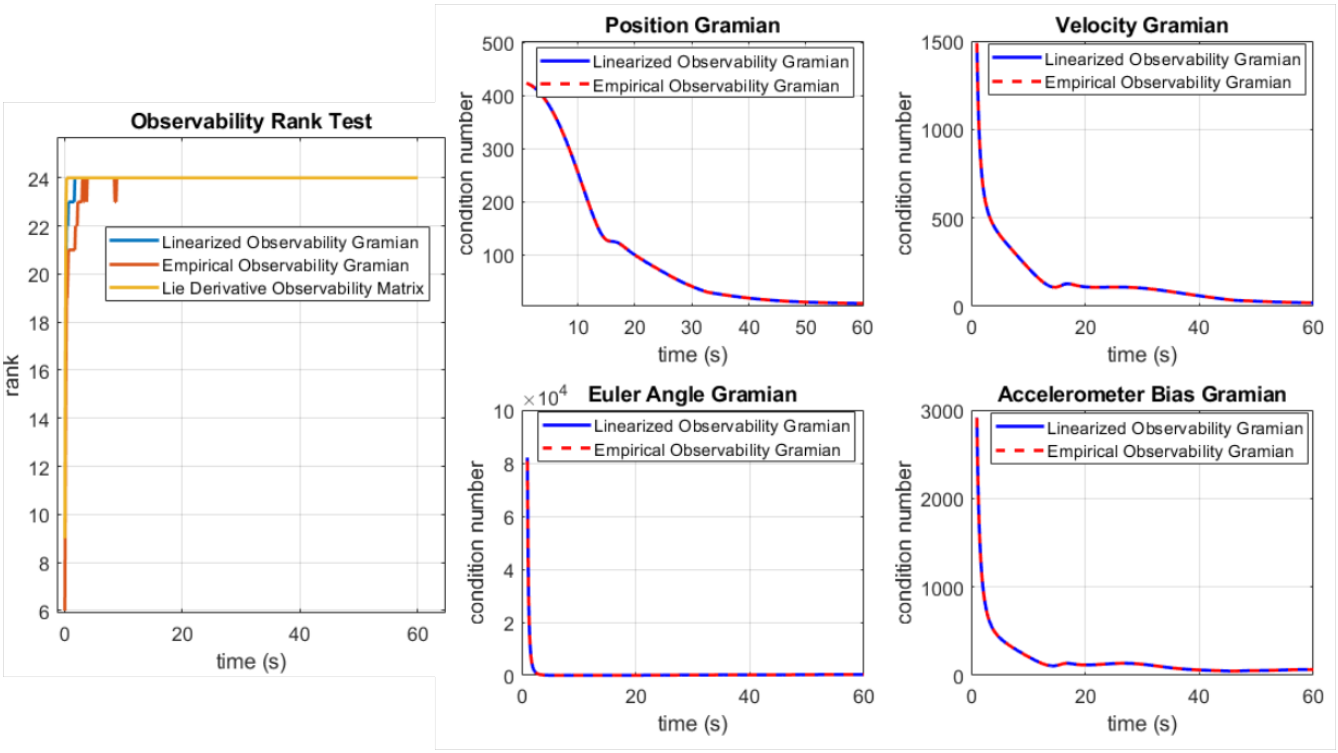

Figure 3.2: Observability methods validation, including: rank test and condition number test of linear and empirical observability Gramians

plot, the Lie derivative observability matrix, the linearized observability Gramian, and the empirical observability Gramian all quickly converge to a rank of 24. This indicates that the system has 24 observable modes with these measurements and vehicle maneuver. This is

below full rank (for cooperative navigation with 2 UAVs full rank is 30), indicating that the system is not fully observable. To determine the level at which each state is observed, the condition number of selected state block diagonal portions of the observability Gramian is calculated and plotted in Figure 3.2. As can be seen in the figure, the linearized and empirical observability Gramian condition numbers are virtually identical. The fact that both of these analysis methods agree is a good indication that the reported values accurately represent the system's observability characteristics. For each of the vehicle states, the Gramian condition number starts at a relatively high value and decays as measurement information becomes available and the system observability is benefited by the inter-UAV maneuver.

3.6.1 UAV to UAV Observability

The effect of the UAV maneuver on the position portion of the Gramian condition number when only relative range is available between 2 UAVs can be seen in Figure 3.3. As

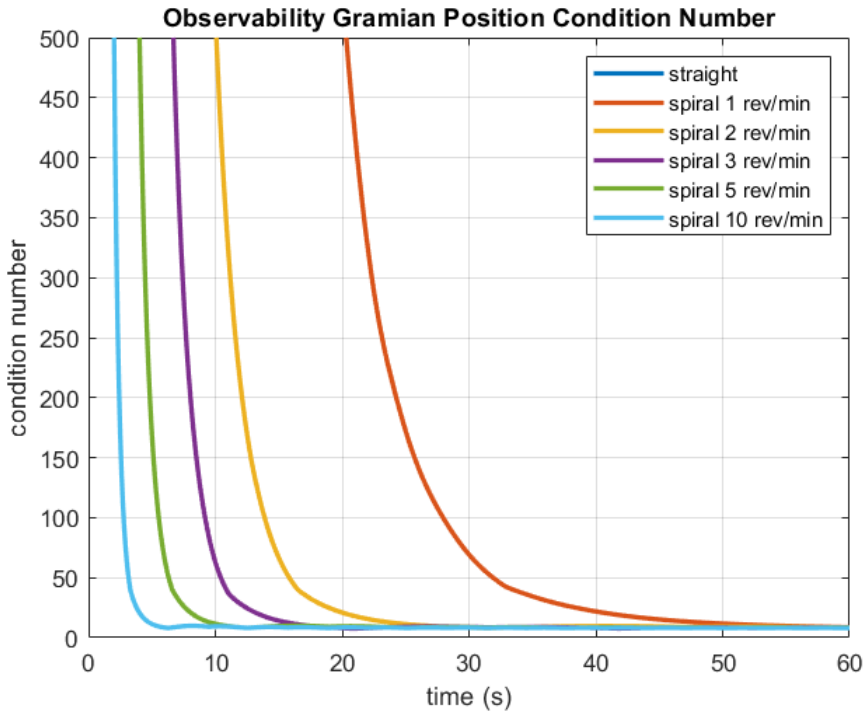

Figure 3.3: Position Gramian condition number with relative range measurement for different maneuvers

the figure shows, the condition number of the Gramian is very high at the beginning of the simulation before settling to a steady-state value. Higher frequency UAV maneuver's result in the condition number settling more quickly. It should also be noted that the position condition number for the straight maneuver (no inter-UAV motion) does not appear on this plot because it is unobservable, with a condition number on the order of 10^{18}. This is because the relative range measurement only provides meaningful position information along its line-of-sight, and when no deviation is made in the inter-UAV geometry, relative position is completely unobserved in the other two position directions, leaving the overall position Gramian unobservable. In the cases with the relative UAV maneuver, as the measurements are taken from different relative orientations, the position Gramian becomes better and better conditioned. With respect to the vehicle motion, each of the lines shown in Figure 3.3 are approximately equivalent. When the vehicles have completed 1/4 of a revolution, the condition number is roughly equal to 1900. When the vehicles have completed 1/2 of a revolution, the condition number is roughly equal to 70.

Considering this important note, each of the spiral maneuvers is approximately equivalent with the time at which certain levels of observability are reached being the only difference. The speed at which these states become more observable is important because while they are unobservable from cooperative measurements at the beginning of the simulated 60 second GPS outage, the INS solution has not had time to drift from the true vehicle state. After a period of time, when the INS solution begins to drift farther from truth, the states become more observable from the relative measurements. If this measurement observability occurs sooner, the INS biases will be better estimated sooner, further limiting the amount of estimation error from INS drift. The condition number for various measurement availability as a function of spiral maneuver completion is shown in Figure 3.4. As seen in the figure, the only measurement combinations that do not result in a condition number approaching infinity at 0 percent maneuver completion are "range + bearing" and "range + range-rate + bearing" (these lines are roughly the same). This indicates that without any maneuver,

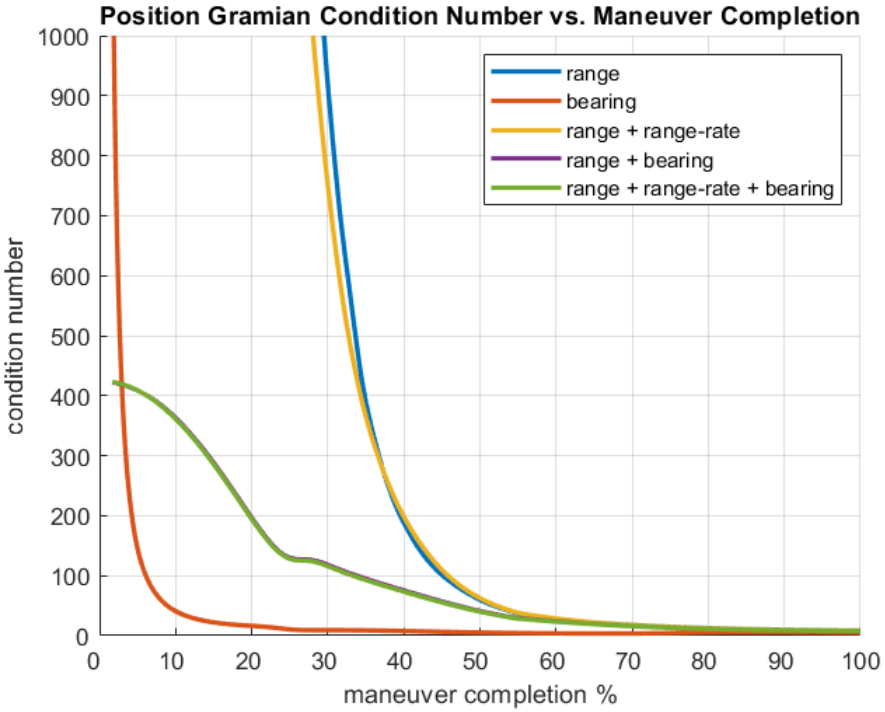

Figure 3.4: Position Gramian condition number vs maneuver completion for different measurement availability, UAV to UAV

cooperative navigation with either of these two combinations of measurements will have position modes that are fairly well observable. Intuitively, this make sense, because a relative position can be determined with the combination of relative range and bearing information. The other three measurement combinations shown in this plot (range only, bearing only, and range + range-rate) have unobservable position modes in the absence of maneuvers. In the relative bearing only case, this condition number quickly decays to smaller values which indicates that even small amounts of vehicle maneuver result in position observability for this measurement. In the case where range or range and range-rate are the available cooperative measurements, the condition number decays more slowly to smaller values indicating that more vehicle maneuvering is necessary to achieve position state observability.

DOP was also calculated and plotted in time to study cooperative navigation observability. Figure 3.5 shows the DOP values for the North, East, and Down positions of a UAV cooperatively navigating with different measurement availabilities. The plots in Figure 3.5

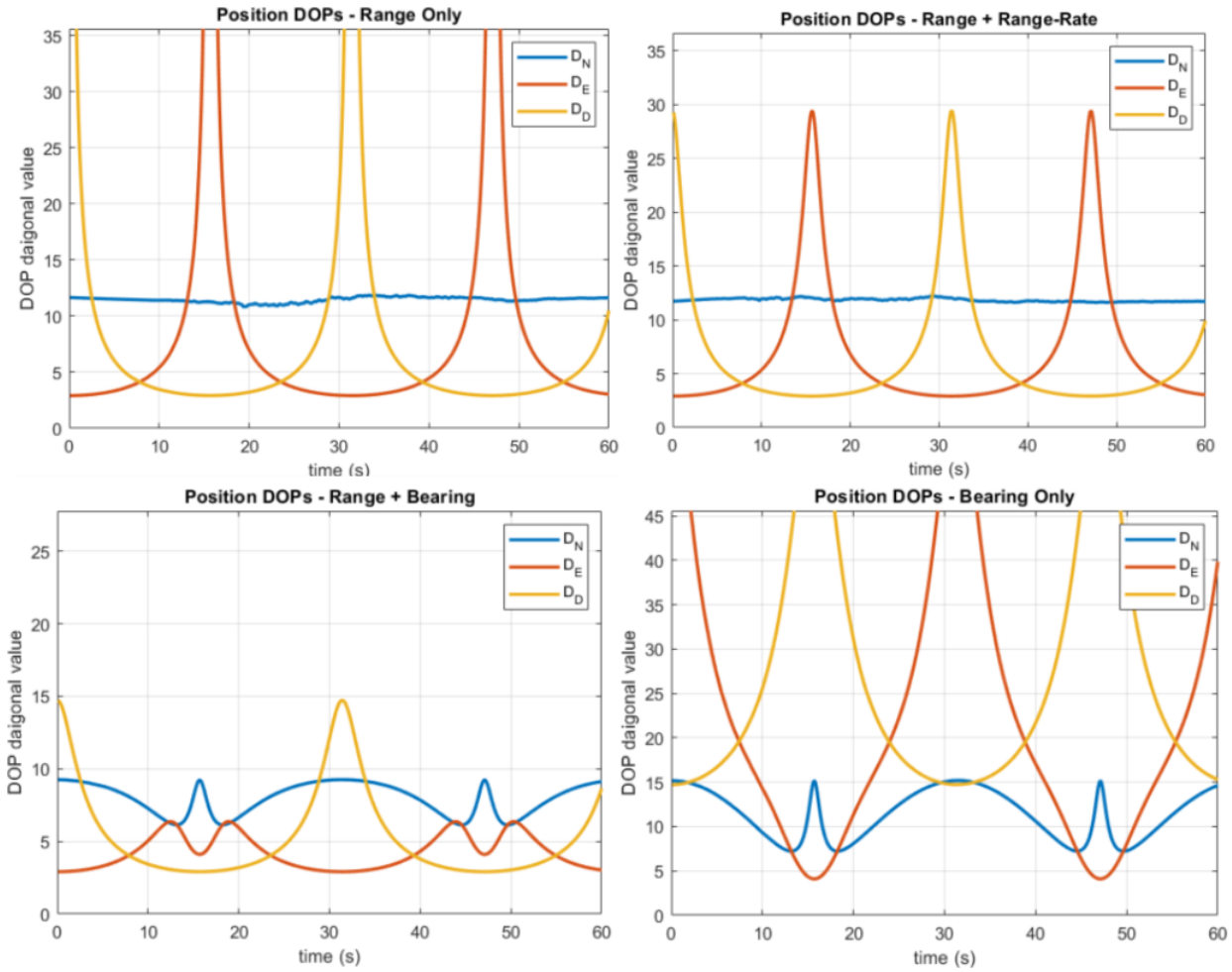

Figure 3.5: DOP values for 2 UAVs navigating with different measurement availabilities (1 "observation cycle")

were generated from a scenario in which UAVs performed 1 spiral maneuver per minute. The plotted DOP values for one full maneuver can be said to represent one "observation cycle" (i.e. the UAVs have traveled through every relative position that will be achieved by this maneuver). The periodic nature of the UAV maneuver results in DOP values that are also periodic in nature. It can be seen in the figure that when range is the only co-operative measurement available to the UAVs, there is a peak in DOP in both the East and Down directions that occurs periodically. This peak corresponds to the point in the maneuver where the line-of-sight is perpendicular to that direction. This demonstrates the fact that range measurements only provide information along the line-of-sight. In the upper

right plot showing DOP when range and range-rate are available measurements, it can be seen that the addition of range-rate measurements provides little difference from the range only case, except for the peaks are lessened in magnitude. In both of these two cases, the DOP for the north direction stays relatively constant throughout the run. This is because there is very little relative motion that changes the line-of-sight in this direction. The plot showing position DOPs with only relative bearing measurements available demonstrates the complimentary nature of range and bearing measurements. In the range-only case, DOP maximums for the East and Down direction occur at the instants where that DOP value is minimized for cooperative navigation with bearing only measurements. Therefore, when both relative range and relative bearing measurements are possible, the position DOP values stay relatively low, regardless of relative positioning, demonstrating this favorable behavior.

3.6.2 UAV to UGV Observability

The observability characteristics of scenarios in which UAVs and UGVs cooperatively navigate is also considered here. In terms of relative measurement observability, the primary difference between this case and the UAV to UAV case is the possible relative inter-vehicle motion for the group. Because the UGV is constrained to operate on the ground, the inter-vehicle spiral shown in Figure 3.1 is not possible. The same level of maneuverability is possible for the UAV, but the UGV cannot perform maneuvers because is is constrained to the roadway surface that it is assumed to be traveling on. Some line-of-sight variation is possible here, however the variation is much more limited than in the UAV to UAV case in which a full 360 degrees of variation was achievable.

The condition number for various measurement availability as a function of UAV spiral maneuver completion is shown in Figure 3.6. Note that when compared to Figure 3.4, these position Gramian values are much higher, as expected. Again, these results indicate that the combination of relative range + relative bearing allows observability regardless of inter-vehicle geometry and maneuver. For the case where relative bearing measurements are the

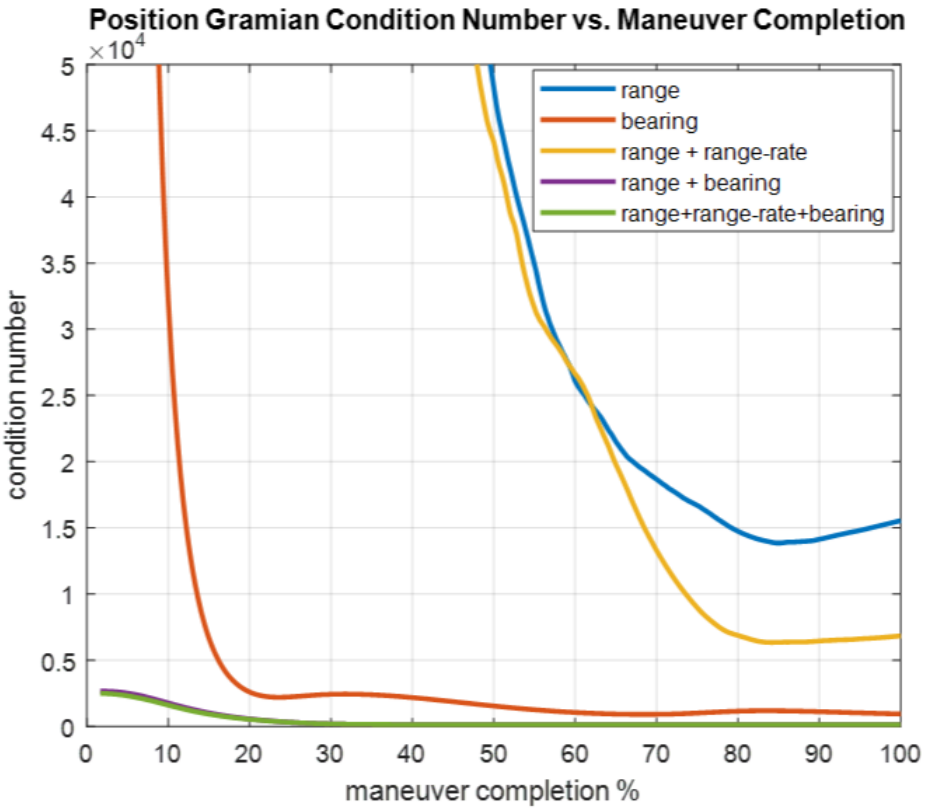

Figure 3.6: Position Gramian condition number vs maneuver completion for different measurement availability, UAV to UGV

only available measurement, the observability Gramian becomes better conditioned after a relatively small amount of vehicle maneuver completion. In the case of range-only or range + range-rate measurements, the position Gramian decays only after a much larger amount of the vehicle maneuver is completed, and even after they reach steady-state, the values are significantly higher than they are in the case where bearing measurements are available. This would seem to indicate that it is difficult to observe relative position with range-only or range + range-rate measurements even in cases with a rapid UAV maneuvers. This result will be further tested in the next chapter of this thesis.

Figure 3.7 shows the DOP values for the North, East, and Down positions of a UAV cooperatively navigating with different measurement availabilities to a UGV for one full maneuver completion. Note that as shown before, the higher DOP values indicate poorer

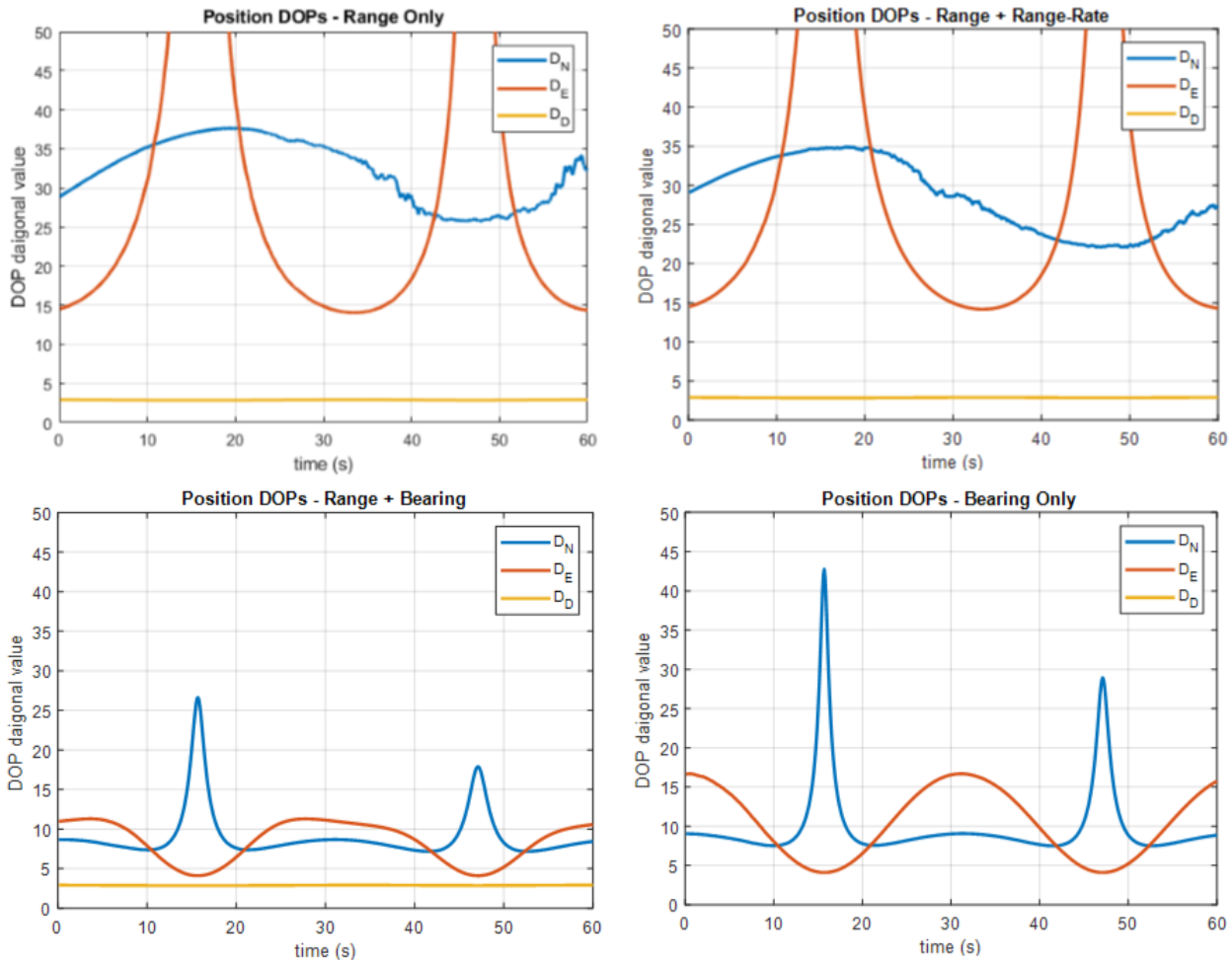

Figure 3.7: DOP values for 1 UAV and 1 UGV navigating with different measurement availabilities (1 "observation cycle")

observability than in the UAV to UAV cooperative navigation case. This is again due to the less favorable inter-vehicle geometry between the UAV and the UGV.

3.7 Conclusion

This chapter introduced observability analysis methods and used these methods to analyze the observability characteristics of a few cooperative navigation scenarios. The observability resulting from UAV to UAV and from UAV to UGV scenarios was investigated in terms of the observability Gramian condition number and in terms of DOP. More favorable

geometry can be achieved through vehicle maneuver between cooperating UAVs than with a single cooperating UAV and UGV. The analysis here predicts better relative navigation for cooperative groups involving multiple UAVs than for cooperative groups involving only a single UAV and UGV. However, ground vehicles also present their own unique benefits which were not considered in this analysis including the possibility of incorporating more accurate INS and the use of digital elevation models to constrain their vertical position error to an absolute reference. Additionally, cooperative groups involving multiple UAVs in addition to a UGV could potentially take advantage of the favorable inter-UAV geometry as well as the unique UGV benefits.

For faster spiral rates, the number of "observation cycles" that occur during the 1 minute GPS outage will be increased along with the frequency at which the relative position between the cooperating UAVs in any given direction is made more observable by favorable geometry. Stated another way, the intervals of time in which the relative position in a given direction cannot be observed are decreased. Therefore, the interval of time in which the drifting INS solution must be depended on in that direction is also decreased. This results in more accurate relative positioning and more accurate accelerometer bias estimation. In order to validate these results and test these hypotheses, simulations of various cooperative navigation scenarios are tested in the next chapter.

Chapter 4

Evaluation of Cooperative Navigation Methods

The various cooperative navigation scenarios introduced in the previous chapter were evaluated in a simulation environment developed in MATLAB. In each of the scenarios, varied frequency UAV spiral maneuvers (discussed in Section 3.4) as well as different measurement availability were tested in order to determine the most beneficial maneuver/measurement combinations that result in the most improvement in state estimation accuracy while limiting communication and computational loads and maneuver control effort. Estimator architectures (centralized EKF and decentralized CI) were also compared for the 2 UAV scenario. For each of the following scenarios, Monte Carlo simulations (varying IMU and measurement errors) were performed to determine estimation accuracy over the course of a simulated 60 second GPS outage for either the entire group or part of the group. Each vehicle was initialized with accurate navigation state estimates with sub-meter level positioning uncertainty. The UAVs and UGVs traveled with a constant velocity of 1 m/s in the North direction for the each of the simulation runs. The UAV East and Down direction velocities were varied in order to perform the spiral maneuver. In every scenario, the cooperative group is assumed to be traveling together in formation from a common start location to a common goal location. The dead-reckoned, IMU-only navigation solution is used as the baseline for comparison to the cooperative navigation solution. The mean IMU-only relative and absolute position errors for the simulated UAVs and UGVs is shown in Table 4.1.

Table 4.1: IMU-only mean end-of-run absolute and relative position errors (m)

Relative Position Error		**Absolute Position Error**	
UAV - UAV	85.3	UAV	55.9
UAV - UGV	59.2	UGV	5.3

4.1 Scenario: 2 UAVs

The first scenario involves two UAVs. The maneuver type "Straight Path" is represented in Figure 4.1 (a) and Figure 4.1 (b) is an example of the "Spiral Path." The axes shown in

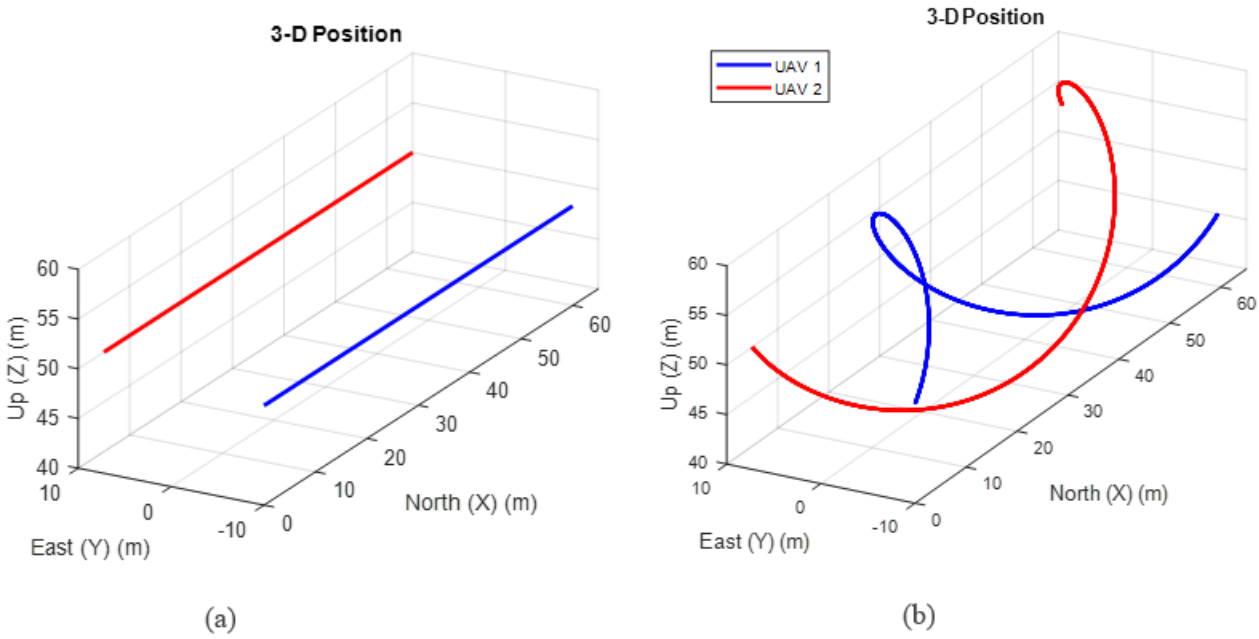

Figure 4.1: 2 UAV simulation scenarios (a) straight path (b) spiral path

the figure are North (X), East (Y), and Up (Z). While the UAVs are operating in an NED frame, the Up direction is equivalent to the negative Down direction and is shown instead of negative Down for clarity. The UAVs nominally fly at 50 m altitude with 0 in the Up/Down direction being considered a flat earth surface.

In many cooperative navigation scenarios, none of the cooperative vehicles have access to absolute position information from GPS. In this case, the cooperative solution will grow unbounded in time due to the INS drift. However, there are still benefits from cooperation in the case where no absolute position information is available. Firstly, the average rate at which this absolute position error growth occurs is decreased. Figure 4.2 shows a comparison between the dead-reckoned (IMU-only) navigation solution position error and the cooperative navigation position error growth over 60 seconds where no GPS information is

available for two cooperating UAVs. This specific plot is for cooperation with relative-range

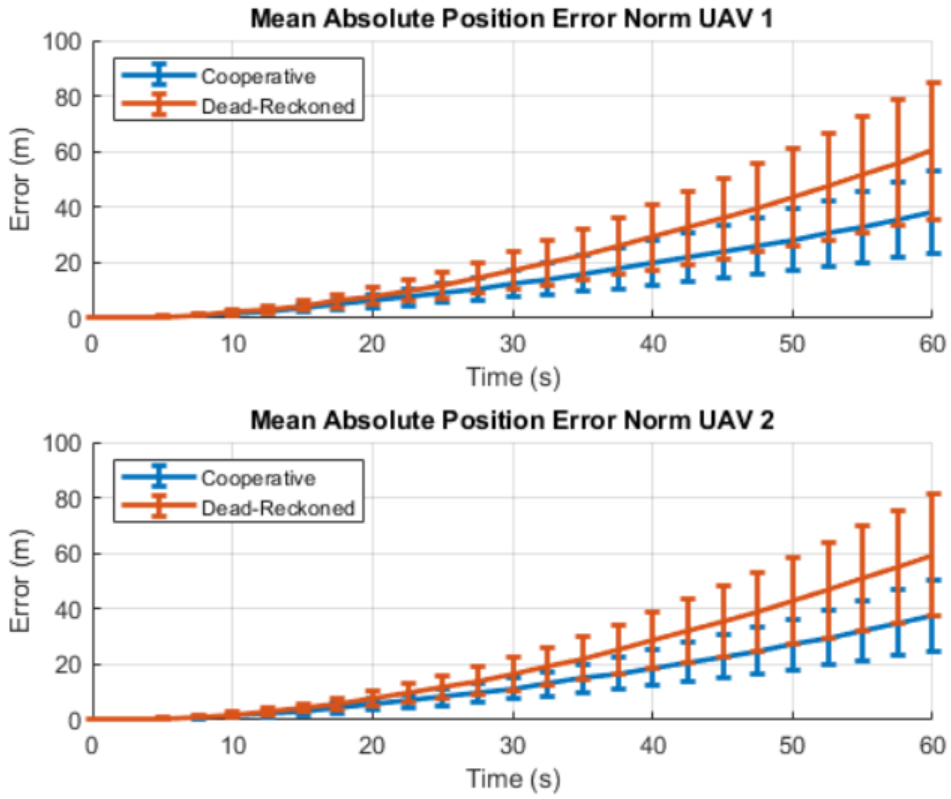

Figure 4.2: Typical cooperative navigation position error growth with no GPS

only measurements and a UAV spiral rate of 1 revolution per minute. The improvement is consistent to some degree for any type of cooperative measurement with any maneuver in both centralized and decentralized architectures. This data was generated by averaging the position error results of a Monte Carlo analysis with the error bars representing the one standard deviation bound on position error. The reduction in positioning error is in effect a result of an "averaging" in position error that occurs between cooperating vehicles that are dead-reckoning drifting INS solutions. Figure 4.3 shows an example of this "averaging" effect on the position solution for two UAVs that are cooperating via relative range and bearing measurements. Considering that the IMU errors causing the drift are random variables with zero mean, an averaging of the resulting dead-reckoned errors results in a reduction in absolute position error. In Figure 4.3, the non-cooperative IMU-only solution for UAV 1 drifts to the right while UAV 2's IMU-only navigation solution drifts to the left. When cooperation

is introduced, the averaging of these two errors results in a fairly accurate positioning result in the East direction. In the North direction, both IMU solutions predict that the UAVs travel a greater distance than they actually travel. In this case the "averaging" effect still occurs, but with a smaller reduction in absolute position estimation error.

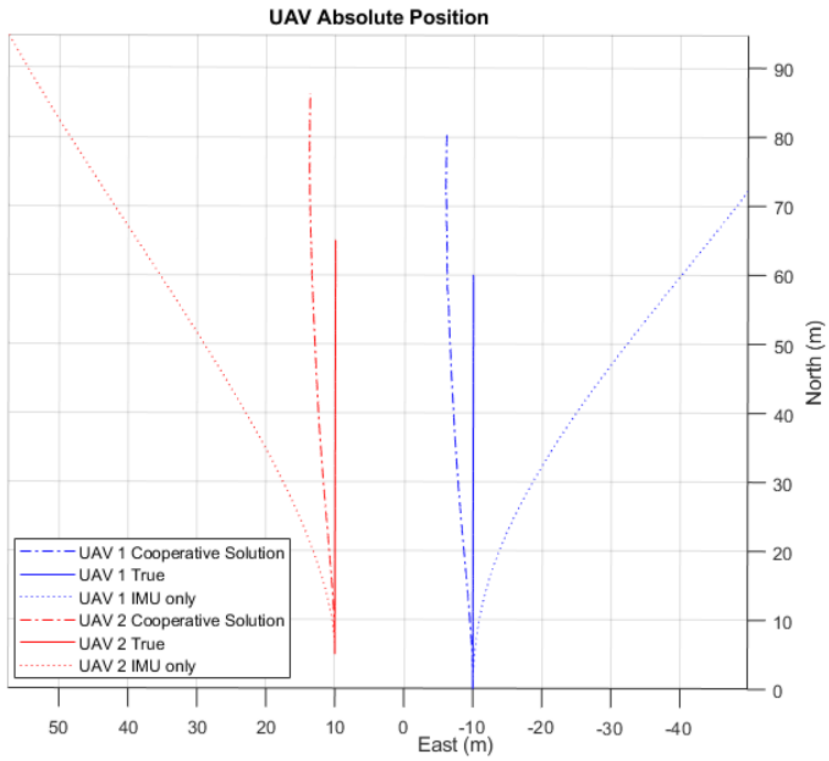

Figure 4.3: Absolute position in North-East plane in the case of 2 UAV cooperation with relative range and bearing but no access to GPS

A second benefit of cooperative navigation in the case where no absolute position information is available is that even though the absolute position estimate is drifting unbounded, the relative position may be accurately estimated. This is also evident in Figure 4.3. It can clearly be seen that while the cooperative solution absolute positioning estimate has a significant amount of error, the relative position of the two UAVs is very accurate when compared to their true relative positions. Figure 4.4 shows both absolute and relative position errors for two UAVs navigating cooperatively with relative bearing measurements and a UAV spiral rate of 2 revolutions per minute. Plotted are the Monte Carlo average errors. An important phenomenon to note from this figure is the cyclic nature of the relative position errors. This

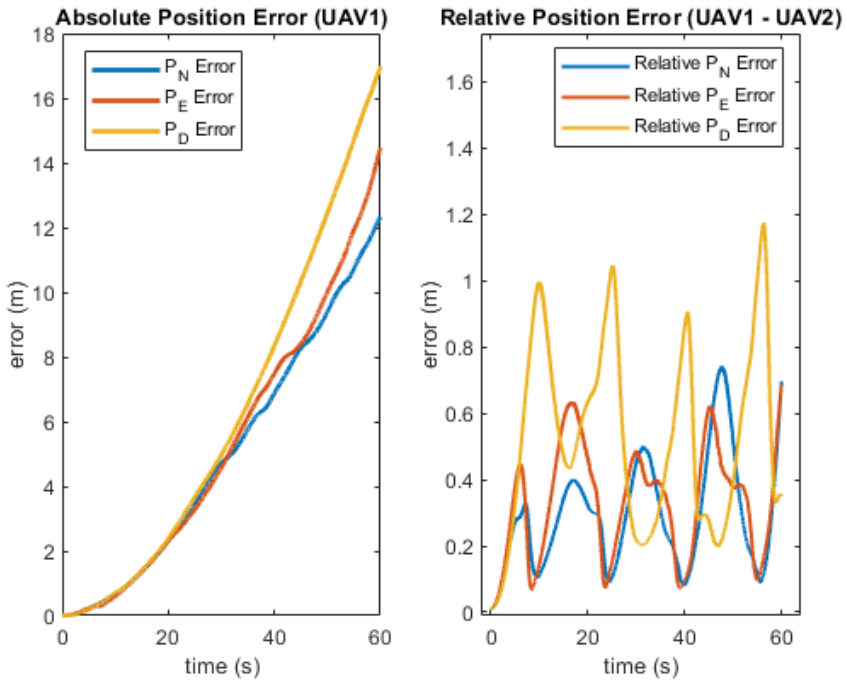

Figure 4.4: Absolute vs. relative positioning accuracy without absolute position reference

is a result of the UAV spiral maneuver being performed. Relative position is more observable in certain directions than others as the UAVs have different relative orientations throughout the maneuver. This effect can be seen mathematically in the position DOP values and as elements of the measurement matrix (H) change throughout the maneuver. As relative position become more observable in any given direction, the measurement is able to reduce the error in that direction. As the maneuver continues and that state becomes less observable, the error begins to grow again as there is no measurement that can effectively correct the drifting navigation solution in that direction.

Figure 4.5 shows the absolute position error norm for a case where relative bearing measurements are the only available cooperative measurement for both the straight UAV path and the spiral maneuver at 1 revolution per minute. The mean error and error standard deviation is slightly lower for the case with the maneuver, however the difference is minimal. The relative position error for this case is shown in Figure 4.6. Here, there is a dramatic difference in relative position error between the case with no maneuver and the case with

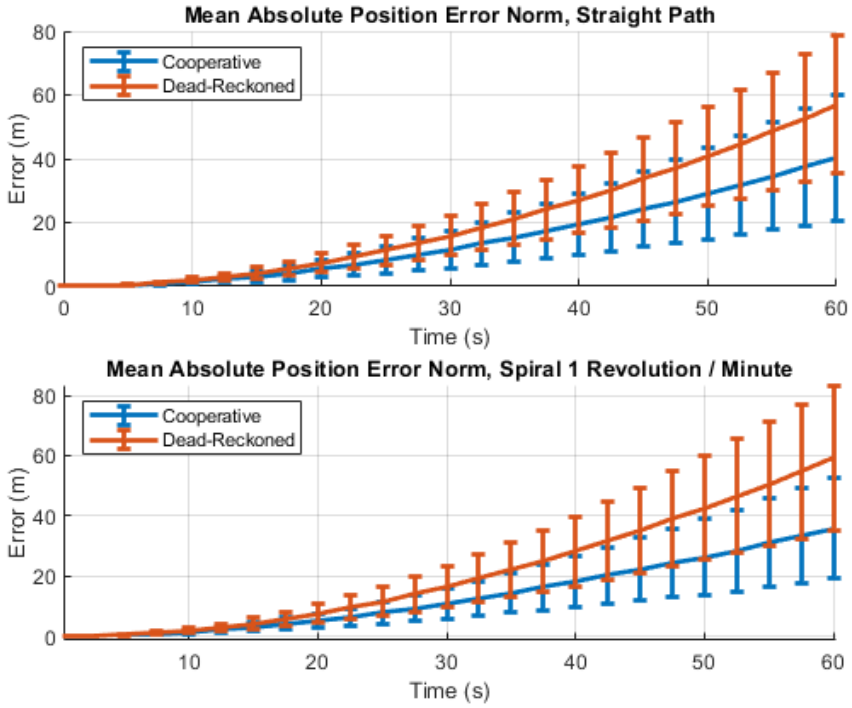

Figure 4.5: Absolute position error with relative bearing only, straight and spiral maneuver at 1 rev/min

the 1 spiral per minute maneuver. This is the result that was predicted by the observability analysis shown in Figure 3.4. It should also be noted that in the case where the UAVs travel along a straight path, the relative positioning error in the East direction grows much more quickly than the error in the North or Down directions. This is a result of the bearing-only measurement characteristics paired with the straight path formation geometry. Relative bearing measurements provide no positioning information along the line-of-sight of the two vehicles. As seen in Figure 4.1, the line-of-sight for these two UAVs is almost directly along the East axis. Therefore, the relative position error along this axis grows much faster than the error in the other directions as seen in Figure 4.6. Similarly, relative range measurements only provide useful position information along the inter-vehicle line-of-sight. In the case where vehicles are able to measure both relative range and relative bearing, the relative position between two vehicles is well observable in all three directions. When this is the case, further

vehicle maneuvers will provide little benefit because it is no longer necessary to change the inter-vehicle geometry to better observe any of the three relative position directions.

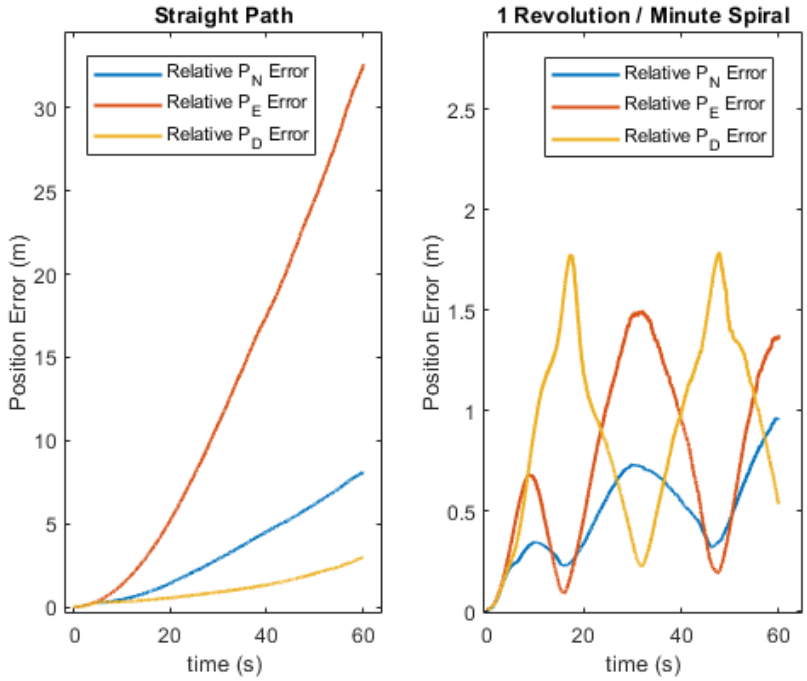

Figure 4.6: Relative position error with relative bearing only, straight and spiral maneuver at 1 rev/min

Figure 4.7 shows the Monte Carlo, mean relative position error for the UAVs using a centralized EKF at the end of the 60 second run. Each point on this plot represents the results of one Monte Carlo simulation. In the case where no absolute position is available to either UAV, the overall, absolute error will continue to grow as in Figure 4.2. In the case where one UAV is able to obtain absolute position information from either GPS or an alternative positioning method, the error values shown in Figure 4.7 are relative to a UAV with known absolute location and can therefore also be considered absolute position errors for the vehicle without a GPS fix. As can be seen in the figure, relative bearing-only provides the worst performance when there is no relative UAV maneuver, but dramatically improves to match the best-performing measurement combinations when there is even a slow UAV spiral maneuver that changes the relative UAV geometry. This is the same effect that

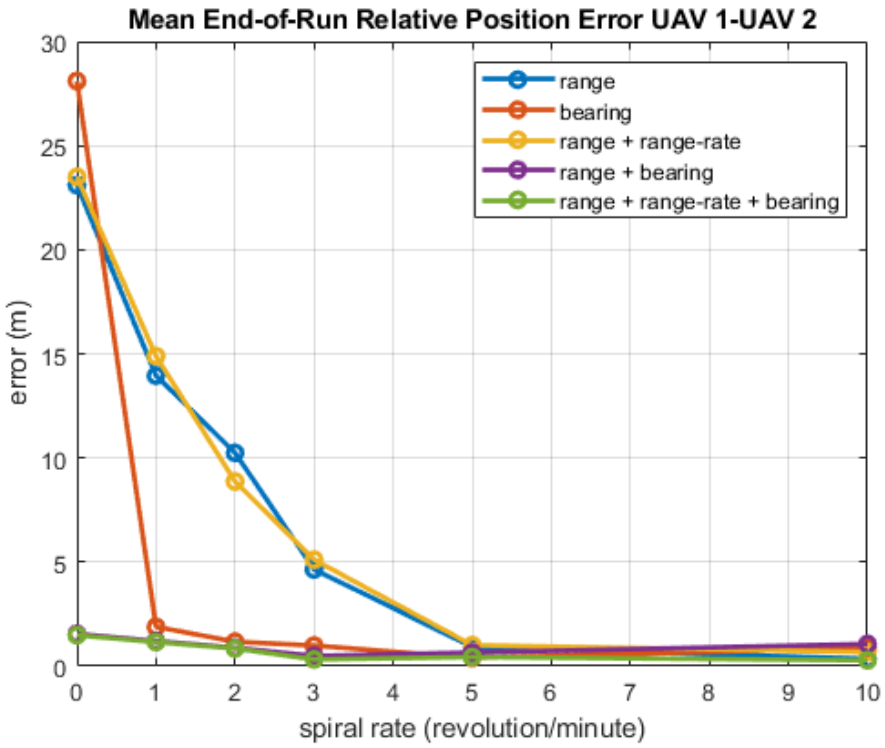

Figure 4.7: Monte Carlo end-of-run position errors for varied measurement and UAV maneuver, centralized EKF, 2UAVs

was predicted by the observability analysis and shown in Figure 4.6. These Monte Carlo analysis results also agree with the observability analysis in that augmenting relative range measurements with relative range-rate provides little, if any, improvement in relative position estimation. Cooperative navigation positioning accuracy tends to improve gradually as the spiral rate is increased when range only and range with range-rate are measured. When both relative range and bearing measurements are taken, no vehicle maneuver is needed to achieve less than 3 meters of relative positioning error at the end of run.

Figure 4.8 shows this same data for the decentralized Covariance Intersection algorithm. The position errors for the decentralized CI algorithm and the centralized EKF algorithm are almost identical. It was found here that it is possible to tune the measurement weighting in this algorithm to provide virtually identical results to the centralized filter. However, this resulted in inconsistent covariance estimates in many cases. Additionally, the tunings and scalings required to achieve this performance for this algorithm proved to be highly heuristic.

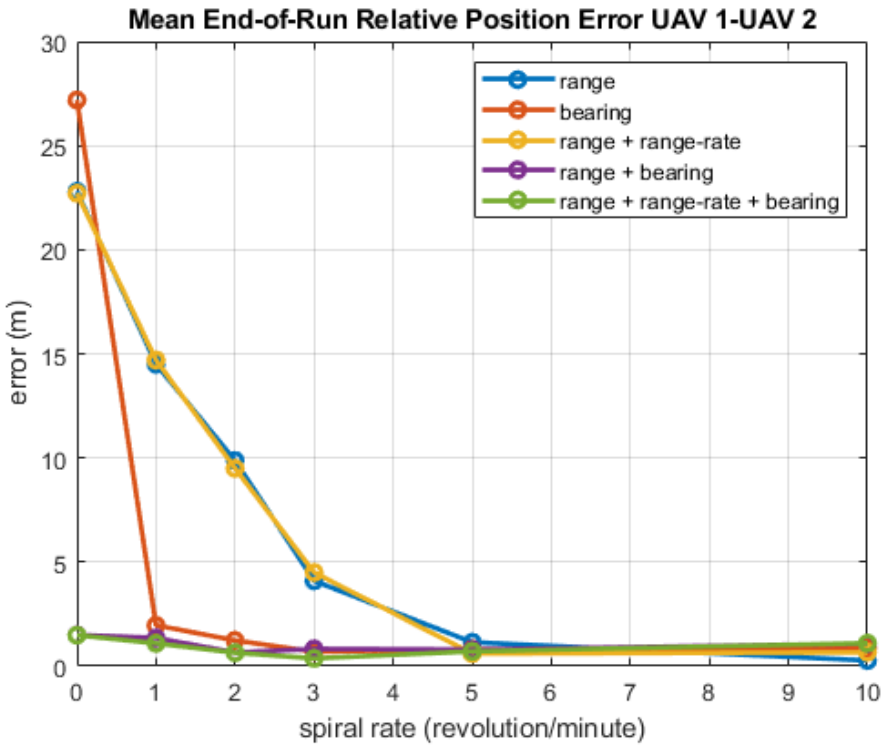

Figure 4.8: Monte Carlo end-of-run position errors for varied measurement and UAV maneuver, decentralized CI, 2UAVs; CI tuned for accurate positioning, ignoring covariance bounds

Many of these tuning factors for this algorithm are discussed in [19]. A trade-off between accurate covariance bounding and estimation accuracy was found to be an issue of primary concern for this algorithm. To achieve the centralized algorithm's level of state estimation accuracy, the covariances had to be tuned below realistic expectations of estimation uncertainty. This can be seen in Figure 4.9, for the case with relative ranging only and no vehicle maneuver. As shown in the figure, the CI 1 standard deviation position estimates are an order of magnitude smaller than the Monte Carlo uncertainty while the EKF accurately estimates this uncertainty bound. In application, this inaccurate uncertainty estimate is undesirable because too much confidence is placed in the inaccurate navigation solution. While the primary purpose of the CI estimation algorithm is to inflate the decentralized covariance values to account for the unknown correlation terms, in order to achieve estimation accuracy

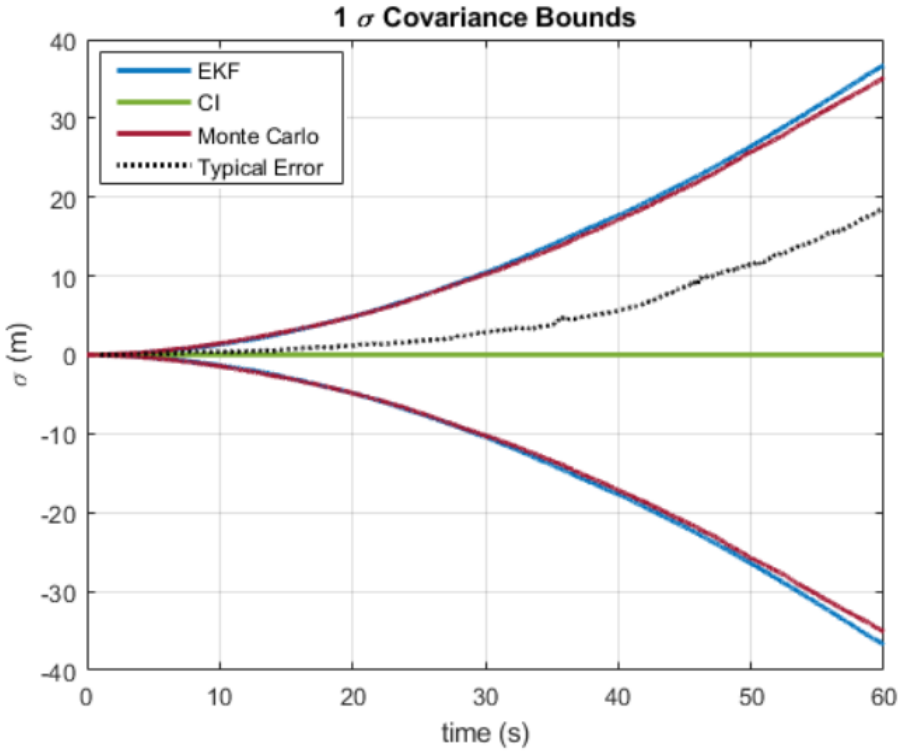

Figure 4.9: 1 σ uncertainty bounds for position error, EKF and CI compared to actual Monte Carlo result, relative ranging only with no UAV maneuver; CI tuned for accurate positioning, ignoring covariance bounds

comparable to the centralized filter this uncertainty had to be tuned to levels inconsistent with the Monte Carlo results.

To compensate for this issue, the CI algorithm was also tuned to allow the estimated covariance to accurately bound the Monte Carlo predicted uncertainty. The covariance estimate for this tuning of the decentralized CI algorithm and the centralized EKF covariance estimate are shown in Figure 4.10 along with the Monte Carlo uncertainties for the case with relative range only and no vehicle maneuver. Note that the Monte Carlo uncertainty for the CI algorithm is now larger than the Monte Carlo uncertainty for the centralized EKF because the CI tuning required to bound this error causes a reduction in positioning accuracy (i.e. there is more uncertainty). Figure 4.11 shows the mean end-of-run position error values for this case. This figure shows a decrease in positioning performance resulting from the use of decentralized estimation while maintaining covariance bounding. As shown in the

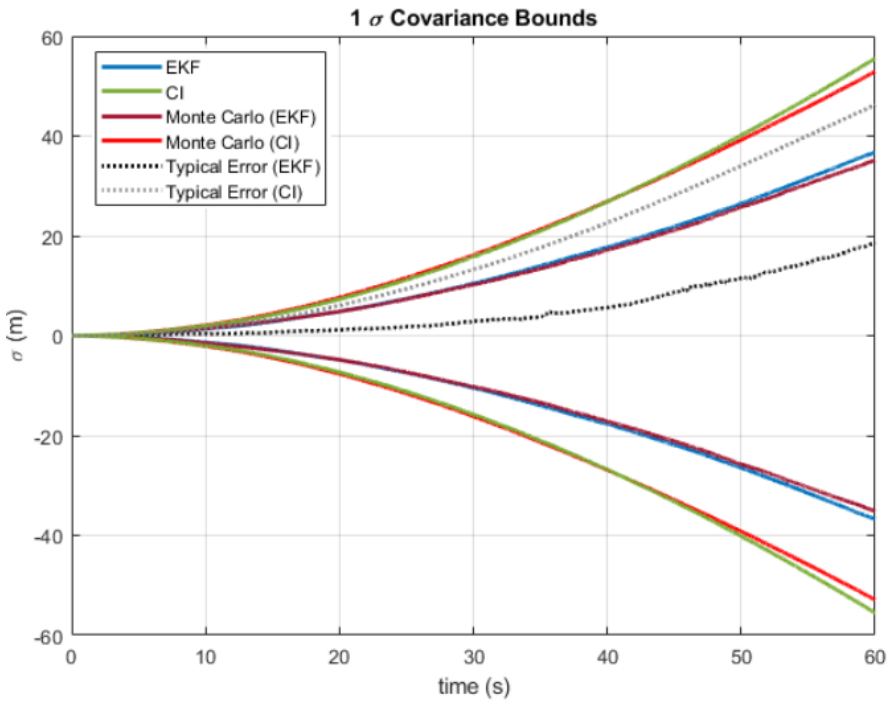

Figure 4.10: 1 σ uncertainty bounds for position error, EKF and CI compared to actual Monte Carlo result, relative ranging only with no UAV maneuver; CI tuned to maintain accurate covariance bounds

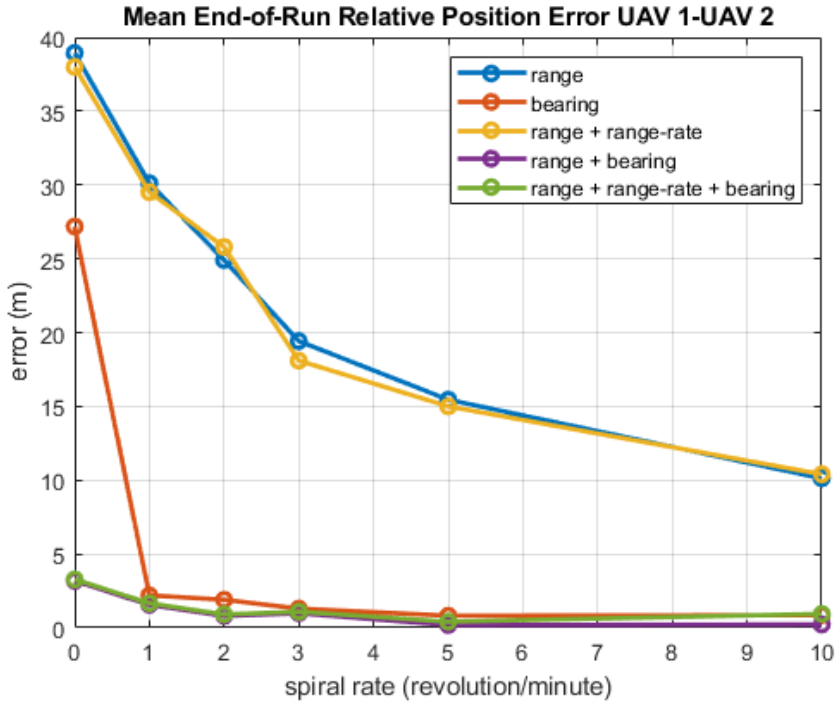

Figure 4.11: Monte Carlo end-of-run position errors for varied measurement and UAV maneuver, decentralized CI, 2UAVs; CI tuned to maintain accurate covariance bounds

figure, the relative position estimates for this tuning are only slightly worse when relative bearing measurements are available. When relative range or relative range and range-rate are the only inter-vehicle measurements, there is a significant decrease in relative positioning accuracy when maintaining accurate covariance estimates.

In other works, [19, 20, 21], that demonstrate consistent covariance estimation of the CI filter for decentralized cooperative navigation, a similar reduction in positioning accuracy from 15% to over 100% was shown depending on the scenario, tuning factors, and measurement availability. For these reasons, only the centralized result will be shown for the remaining cases. A potential avenue for future work would be to determine if similar positioning accuracies for the decentralized algorithm are possible while maintaining consistent covariance estimates, with either the CI algorithm or an alternative decentralized algorithm.

When accurate relative position estimates are possible (errors are kept within 1 to 2 meters, see Figures 4.7 and 4.8), the accelerometer and gyro biases are partially observable. The degree to which these states can be estimated depends on the level of excitation provided from the accelerometer and gyro biases (these biases must differ between the two vehicles) as well as the relative positioning accuracy. Figure 4.12 shows a representative example of accelerometer and gyro bias estimates for the case with two UAVs with accurate relative positioning estimates (i.e. only 1 to 2 meters of relative error). As can be seen in the figure, these states are not completely observable in this case, as the estimates do not always fully converge to the true values. This is especially apparent in the gyro bias 1 and gyro bias 3 directions.

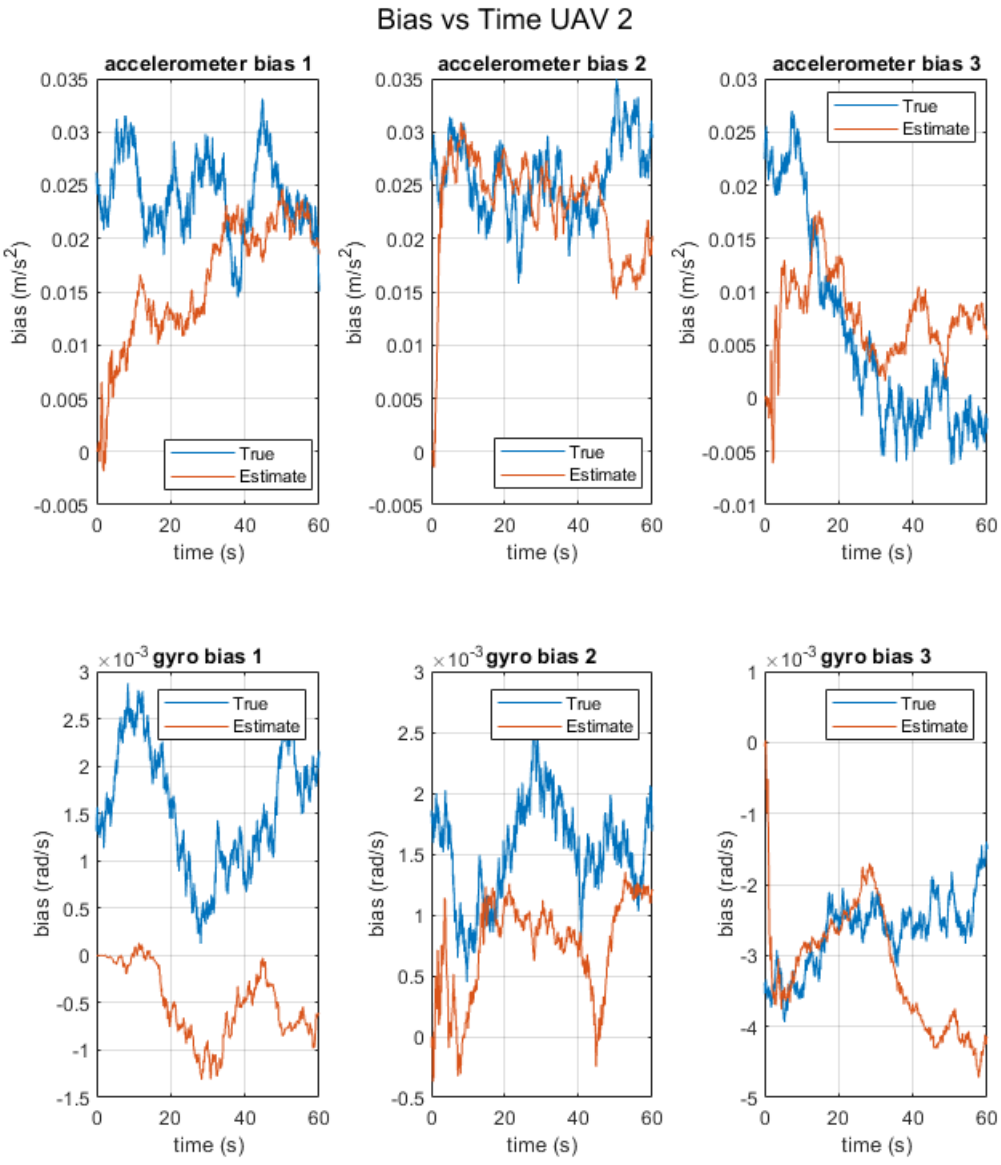

Figure 4.12: Accelerometer and gyro bias estimation for case with two cooperating UAVs and accurate relative position estimates

4.2 Scenario: 3 UAVs

The second simulated scenario involves three UAVs navigating cooperatively. This scenario is shown in Figure 4.13. This scenario is intended to show the effect of adding an

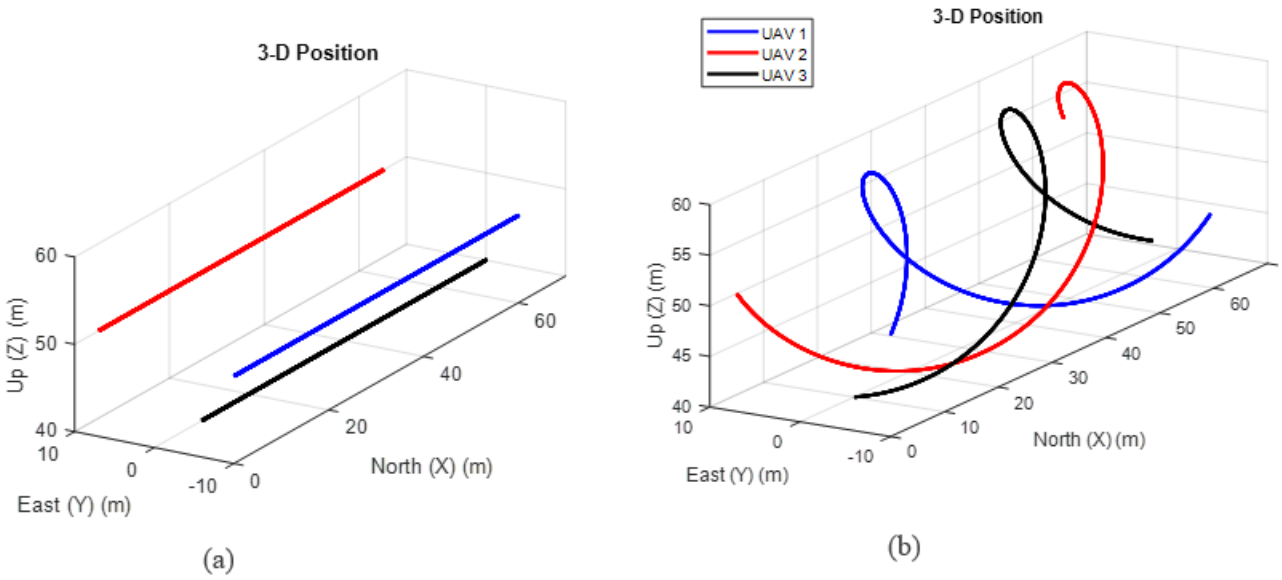

Figure 4.13: 3 UAV simulation scenarios (a) straight path (b) spiral path

additional vehicle to the cooperative group when compared to the first scenario.

Sharma introduced the concept of a relative position measurement graph (RPMG) in [34]. In this graph, the nodes represent vehicles while the edges between nodes represent relative measurements between those vehicles. Figure 4.14 compares the RPMG between the cooperative navigation scenario with two vehicles versus the scenario with three vehicles. The additional UAV in this scenario allows for more relative measurement information to be available to the group. Three relative measurements may now be taken between vehicles as opposed to only one relative measurement in the scenario with two UAVs. Abstracting this phenomenon to a case with n vehicles gives Equation 4.1.

$$number\ relative\ measurements = \frac{n(n-1)}{2} \tag{4.1}$$

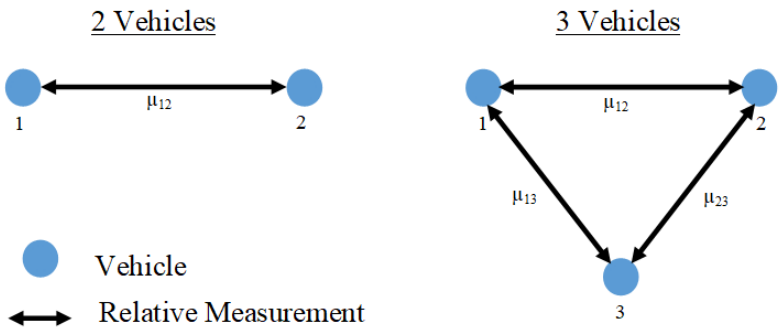

Figure 4.14: RPMG for both 2 and 3 vehicle scenarios

It should be noted that this equation assumes a fully connected graph (i.e. each node is connected to every other node in the group). These additional relative measurements result in improved relative positioning. The additional information from the extra IMU also slightly improves the absolute positioning accuracy of the group, as an additional measurement with random bias and noise is effectively being averaged into the cooperative solution (as seen in Figure 4.3).

Figure 4.15 demonstrates the added benefit of the additional UAV to the average absolute cooperative positioning solution resulting from this "averaging" effect. The two plots on the left half of the figure represent the absolute position error norm for a cooperative group of two UAVs, assuming relative positioning with less than roughly 3 m of error. As shown in the figure, the mean absolute position error for the dead-reckoned IMU solution is around 55 m while the mean absolute position error for the cooperative solution is about 36 m. The three plots on the right half of the figure represent the absolute position error norm for a cooperative group of three UAVs with the same relative positioning accuracy. The mean absolute position error for the dead-reckoned IMU solution here is also about 55 m, as expected since this error is for the uncooperative case. The mean absolute position error for the cooperative navigation solution for this case is 29 m. This is almost a 20 % reduction in absolute position error compared to the case with only two vehicles. A similar reduction in absolute position error growth was seen across all 3 UAV simulation runs with

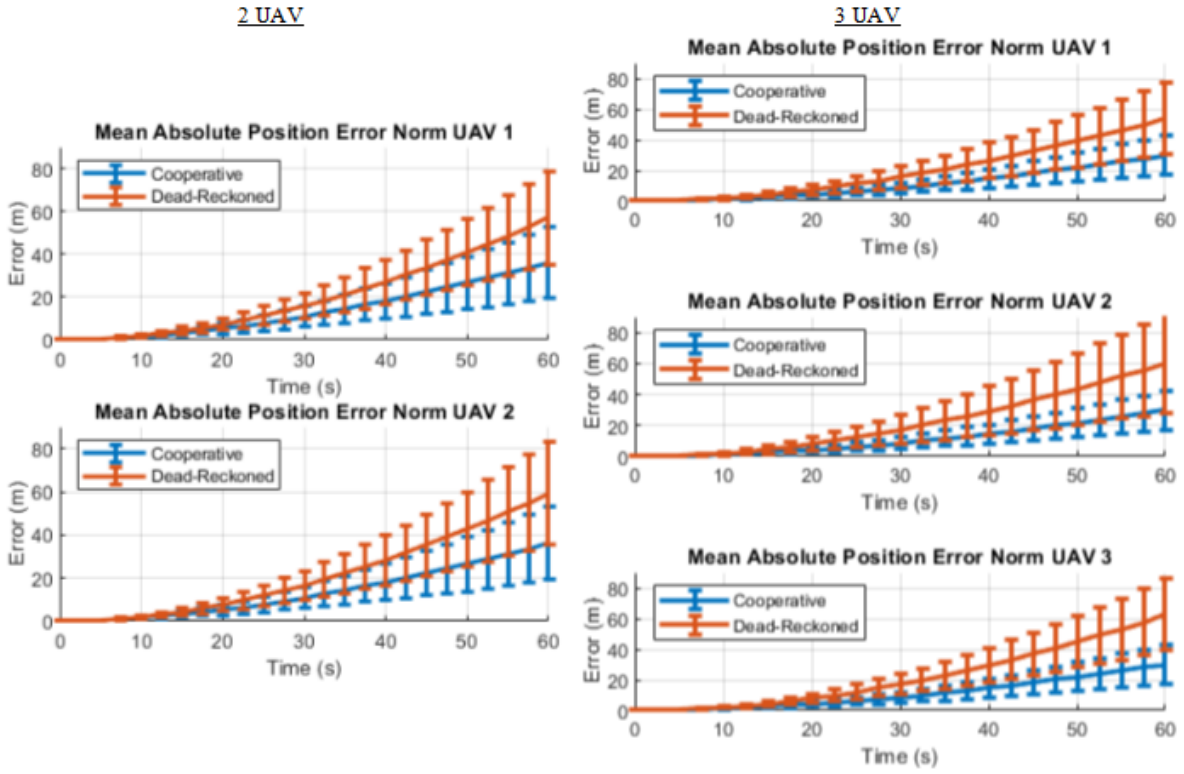

Figure 4.15: Comparison of absolute position growth (assuming accurate relative positioning) for a group of 2 UAVs vs 3 UAVs with no absolute reference

low relative positioning error. Assuming that all IMU biases are randomly distributed with zero mean, continued reductions in absolute position error are expected as the size of the cooperative group increases. An investigation into the absolute positioning of larger "swarms" of cooperating vehicles would be another interesting avenue of future work.

This phenomena also allows the accelerometer and gyro biases to be estimated, even without any form of absolute reference. A representative example of accelerometer and gyro bias estimates for a case with 3 UAVs that are accurately able to estimate their relative positions is shown in Figure 4.16.

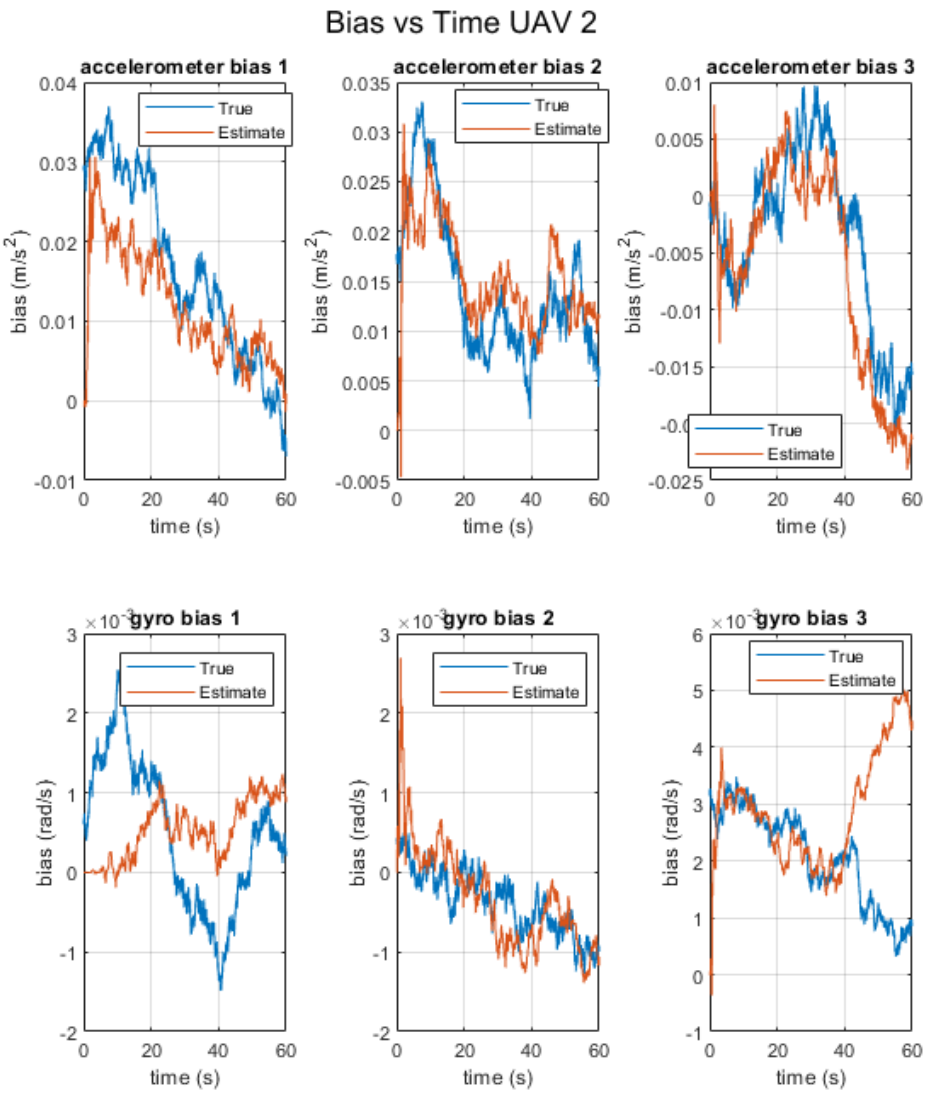

Figure 4.16: Accelerometer and gyro bias estimates with accurate relative positioning but no absolute reference, 3 UAVs

As shown in the figure, each of the accelerometer bias estimates (initialized at 0), converge to the true bias values relatively well. There are some observability issues, especially in the gyro bias estimates, as can be seen in the lack of convergence in the gyro bias 1 and gyro bias 3 direction estimates. Comparing this figure to Figure 4.12 again illustrates the additional benefit of the extra inertial sensor in the cooperative group. These bias estimates are better than the 2 UAV case because this additional sensor (with assumed random bias) provides additional excitation for the observability of these states.

Figure 4.17 shows the Monte Carlo, mean end-of-run position error for UAV 2 relative to UAV 1 for this scenario for the centralized filter. Comparing this figure to Figure 4.7, this

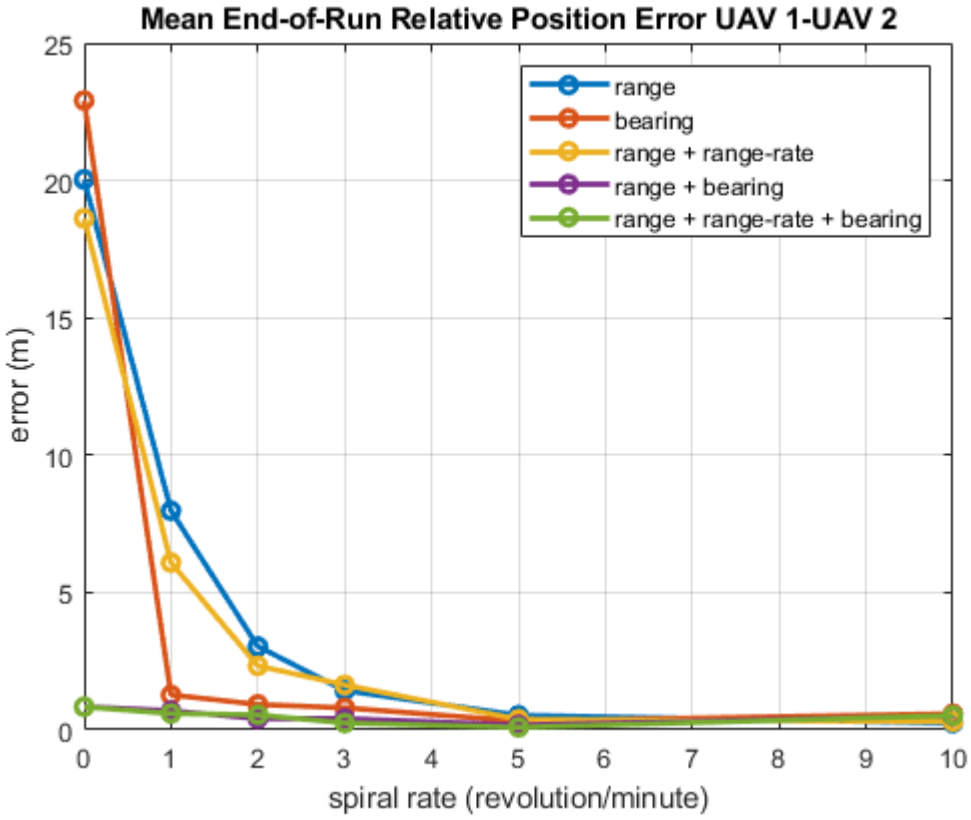

Figure 4.17: Monte Carlo end-of-run position errors for varied measurement and UAV maneuver, centralized EKF, 3 UAVs

scenario demonstrates the improvement in relative positioning accuracy resulting from an additional UAV in the cooperative group. Note that the relative positioning error is smaller for cases with no vehicle maneuver and converges to zero more quickly as the UAV spiral is added. Results with range and bearing are similar to the 2 UAV scenario.

4.3 Scenario: 1 UAV - 1 UGV

The third scenario involves 1 UGV operating on a flat ground below a single UAV. This scenario is intended to show the potential synergistic effects of cooperative navigation between UAVs and UGVs that result from their heterogeneous navigation capabilities. As

mentioned in Chapter 2, because of the different size and weight constraints on the UGV, this thesis assumes that the UGV is equipped with a higher quality, "intermediate" grade IMU as opposed to the lower quality "tactical" grade IMU equipped to the UAVs. Whereas dead reckoning the tactical grade IMU resulted in about 60 meters of error on average at the end of a 60 second run, dead reckoning the intermediate grade IMU resulted in roughly 5 meters of error on average at the end of a 60 second run. The UGV is also able to update its absolute position in the vertical direction by the use of digital elevation models.

The scenario is shown in Figure 4.18. Because of the physical limitations of the maneu-

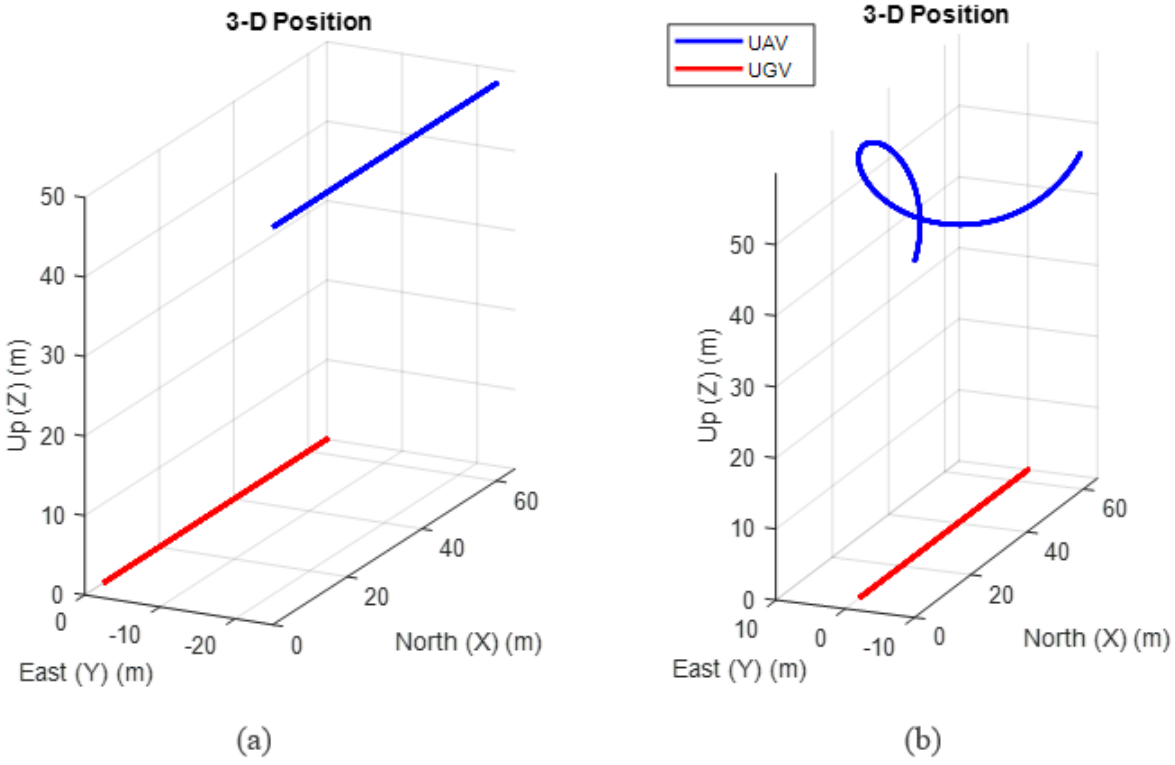

Figure 4.18: 1 UAV 1 UGV Simulation Scenarios (a) straight path (b) spiral path

verability of the vehicles in this scenario, the same levels of inter-vehicle relative motion are not possible with this type of cooperative group.

The mean, end-of-run relative positioning error between the two vehicles is shown in Figure 4.19. As in the previously simulated scenarios, UAV maneuver improves relative

positioning accuracy. However, because of the lower level of inter-vehicle position excitation that is possible with a group consisting of one ground vehicle and one air vehicle, the error reduction is not as dramatic as in the all UAV simulation cases. This further validates the analysis shown in Figure 3.6. Again, there is no improvement due to UAV maneuver when both range and bearing measurements are available.

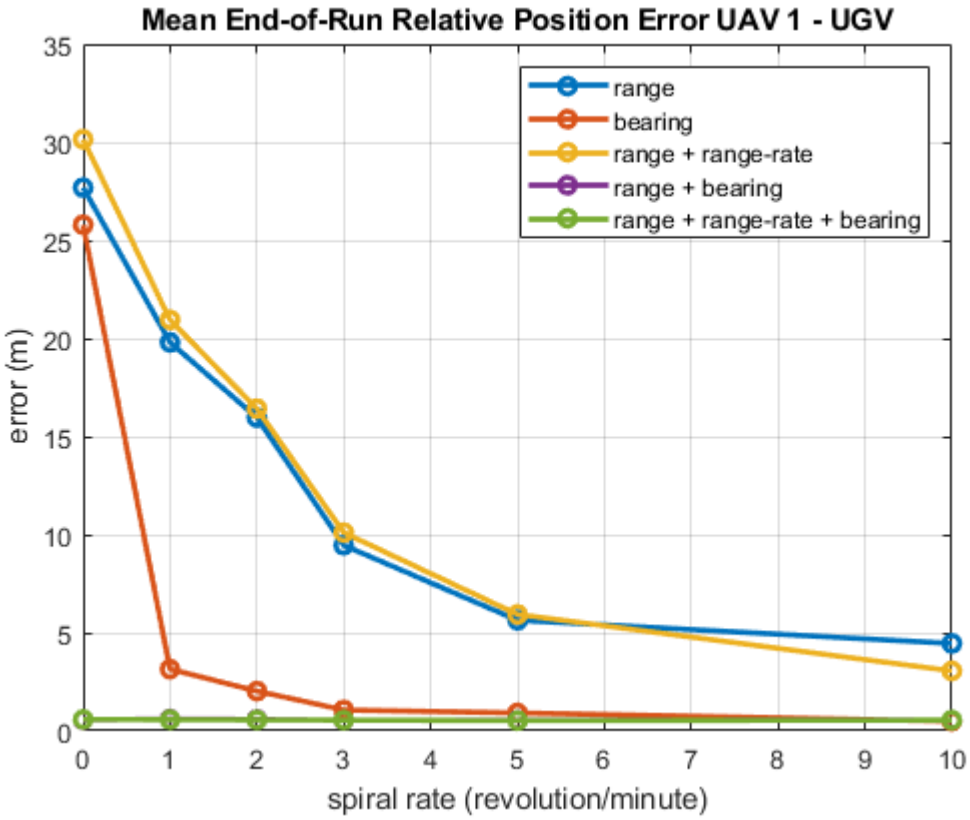

Figure 4.19: Monte Carlo end-of-run position errors for varied measurement and UAV maneuver, centralized EKF, 1 UAV 1 UGV

While it is more difficult to accurately estimate the relative position of the two vehicles in this scenario, if the relative position can be accurately estimated, the UAV's absolute position estimate and accelerometer and gyro estimates benefit greatly from this coupling with the UGV. This is because, as discussed earlier, the UGV is equipped with a more accurate IMU, with smaller biases. This accurate IMU will allow the less accurate UAV IMU to estimate its biases better than in the previous cases where all IMUs had similar

error characteristics. An example of this more accurate bias estimation is shown in Figure 4.20.

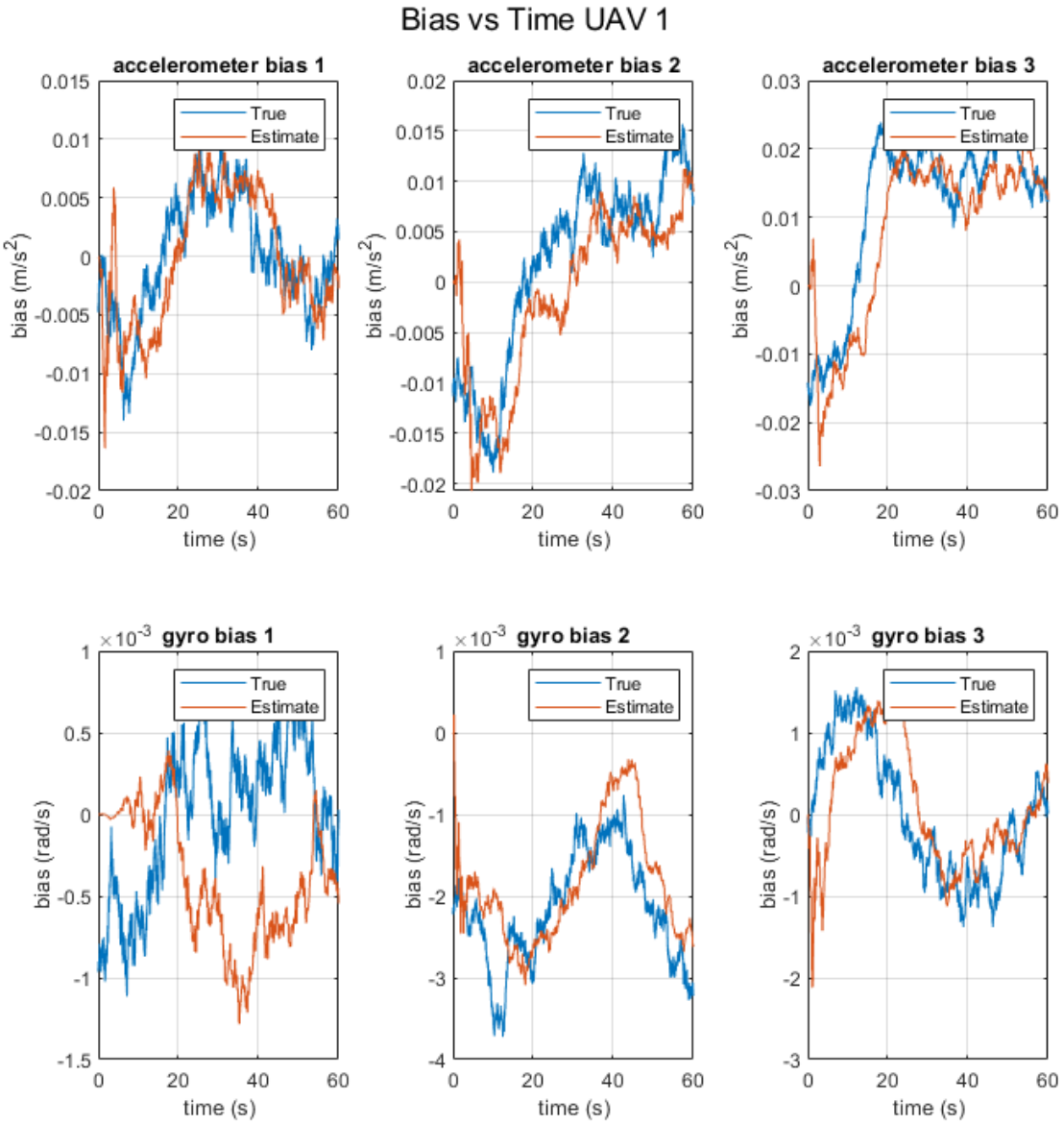

Figure 4.20: Accelerometer and gyro bias estimates with accurate relative positioning but no absolute reference, 1 UAV & 1 UGV case

4.4 Additional IMU Bias Estimation Analysis

To further investigate the IMU bias estimation errors, the IMUs were also modeled with constant biases. This was done to more clearly show the bias estimate convergence to truth (or lack thereof) in the three cases described above. Figure 4.21 shows the IMU bias estimates for the case with two cooperating UAVs with relative range and bearing measurements. As shown in the figure, the IMU bias estimates begin to converge to the true

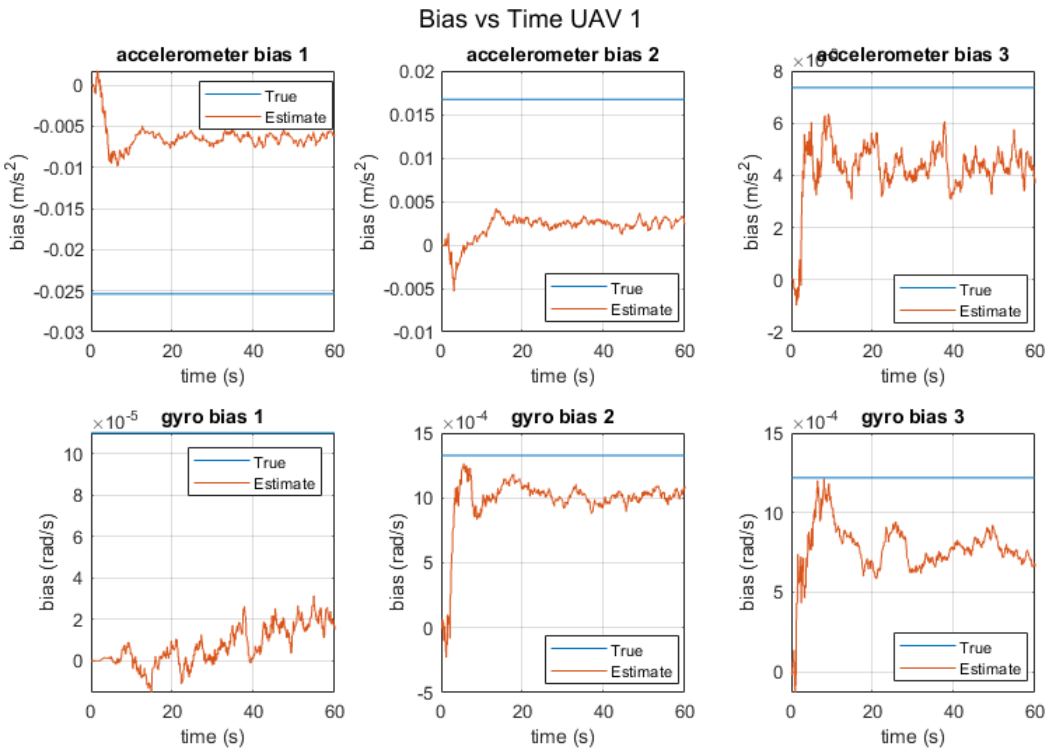

Figure 4.21: Static IMU bias estimation for 2 UAVs with relative range and bearing measurements

bias in almost every direction. However, there is steady-state error in every case. There is also a significant amount of noise in the estimates. Additionally, the "gyro bias 1" direction (roll) is completely unobservable. This is a result of a lack of measurement observability and limited excitation in the roll direction. Figure 4.22 shows the effect of adding an additional UAV to the cooperative group on the IMU bias estimates (the 3 UAV case). Comparing Figure 4.22 to 4.21 demonstrates the improvement in bias estimation from the additional

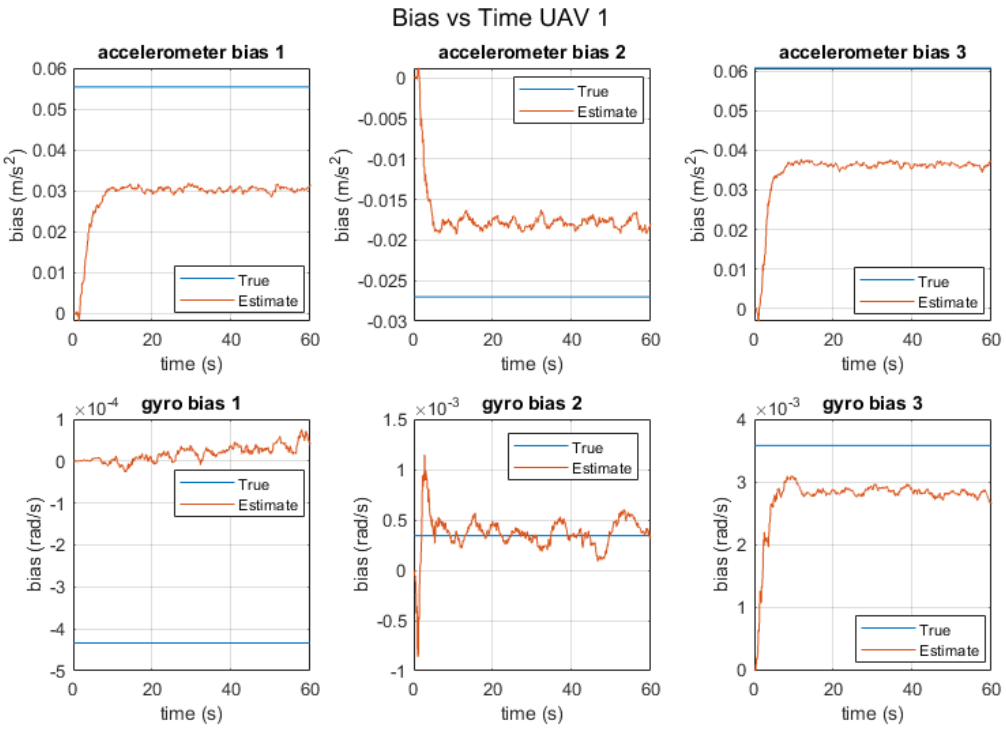

Figure 4.22: Static IMU bias estimation for 3 UAVs with relative range and bearing measurements

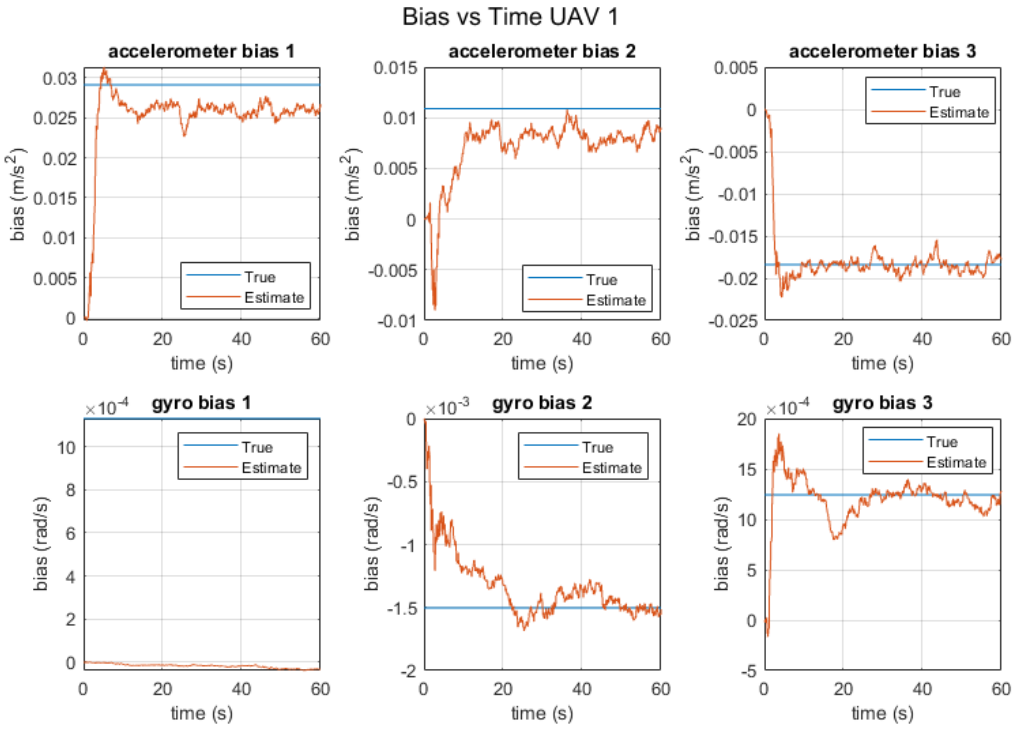

Figure 4.23: Static IMU bias estimation for 1 UAV + 1 UGV with relative range and bearing measurements

UAV in the cooperative group. Here, the bias estimates have slightly less steady-state error and includes less noise.

Figure 4.23 shows the UAV IMU bias estimation for cooperation between one UAV and one UGV with relative range and bearing measurements. Here, the IMU bias estimation contains very little steady state error in every axis except for the unobservable "gyro bias 1." Again, this is the result of cooperation with the higher quality UGV IMU.

In order to examine the average bias estimation error over a large number of runs, a Monte Carlo analysis was performed for static bias estimation in these three scenarios. Figure 4.24 shows the Monte Carlo average bias estimation error for all three cooperative group types over the 60 second simulation. These results further confirm the bias estimation

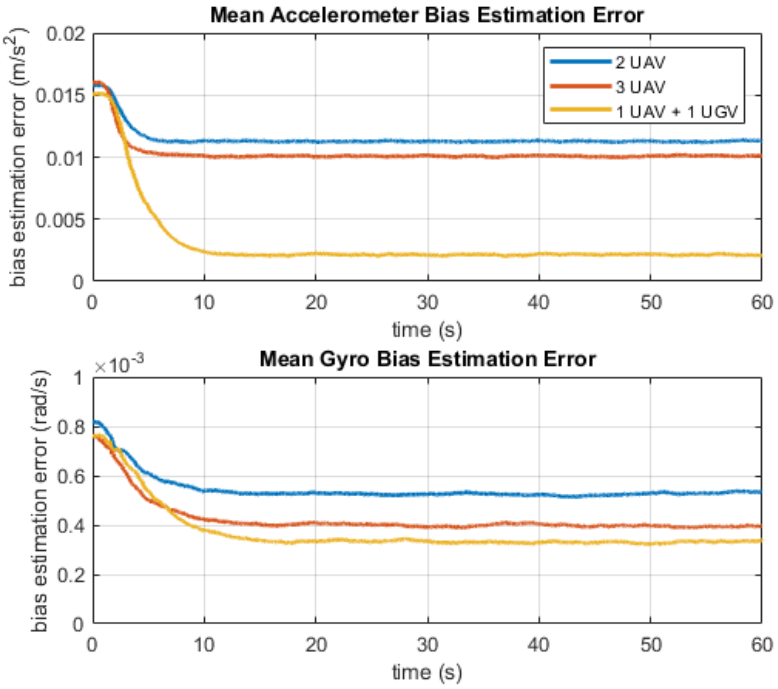

Figure 4.24: Monte Carlo mean IMU bias estimation error

results discussed earlier. The addition of a third UAV equipped with the same low quality tactical IMU as the first two UAVs provides improvement in the bias estimation. The addition of the higher quality IMU to the cooperative group allows for even more significant reductions in bias estimation error.

4.5 Scenario: 2 UAVs - 1 UGV

The last scenario involves 1 UGV operating on a flat ground below 2 UAVs. This scenario is intended to investigate whether adding an additional cooperating UAV will allow for improved relative positioning between the UAVs and the UGV to improve upon the results of the 1 UAV, 1 UGV scenario. This scenario is also intended to investigate the potential synergistic effects of cooperative navigation between UAVs and UGVs when compared to the the first scenario with only 2 UAVs. This scenario is shown in Figure 4.25.

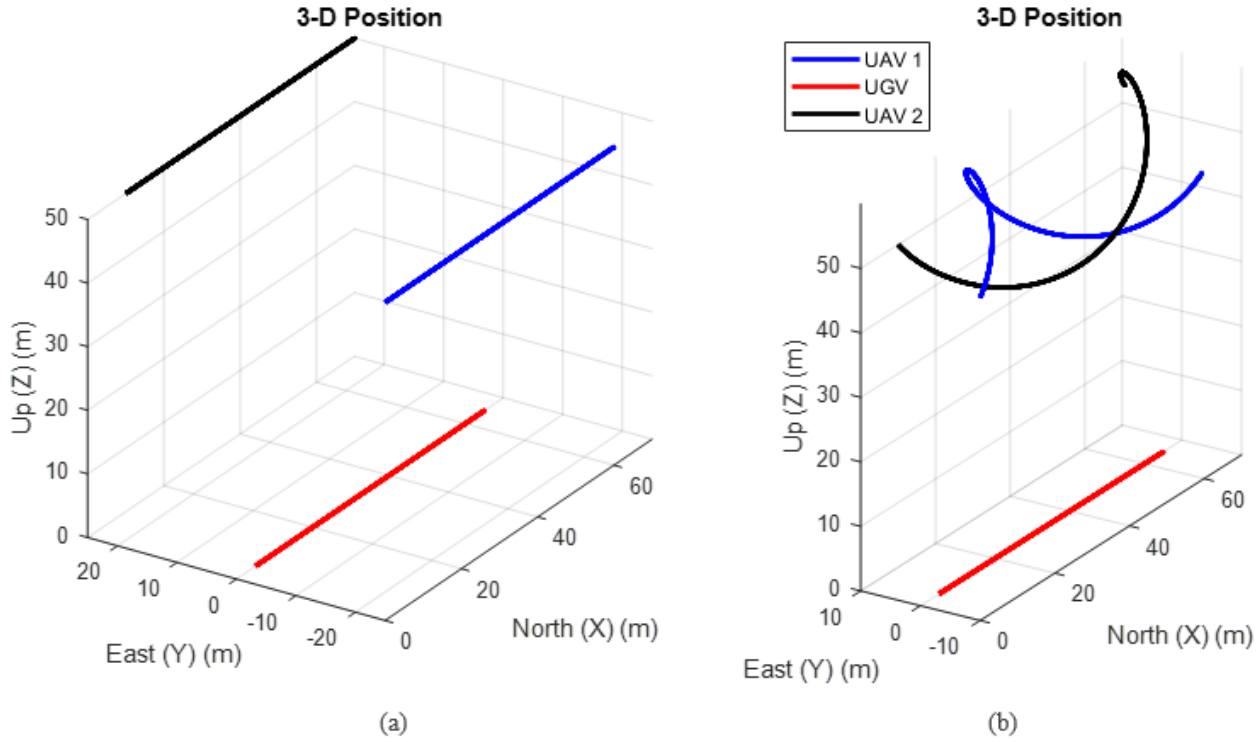

Figure 4.25: 2 UAV 1 UGV Simulation Scenarios (a) straight path (b) spiral path

The relative positioning error between UAV 1 and UAV 2 for this scenario is shown in Figure 4.26. The relative positioning error between UAV 1 and the UGV for this scenario is shown in Figure 4.27. These two figures demonstrate very similar results within this type of cooperative group with the UAV-to-UAV relative positioning having slightly less error than the UAV-to-UGV relative positioning. This is due to the difference in relative

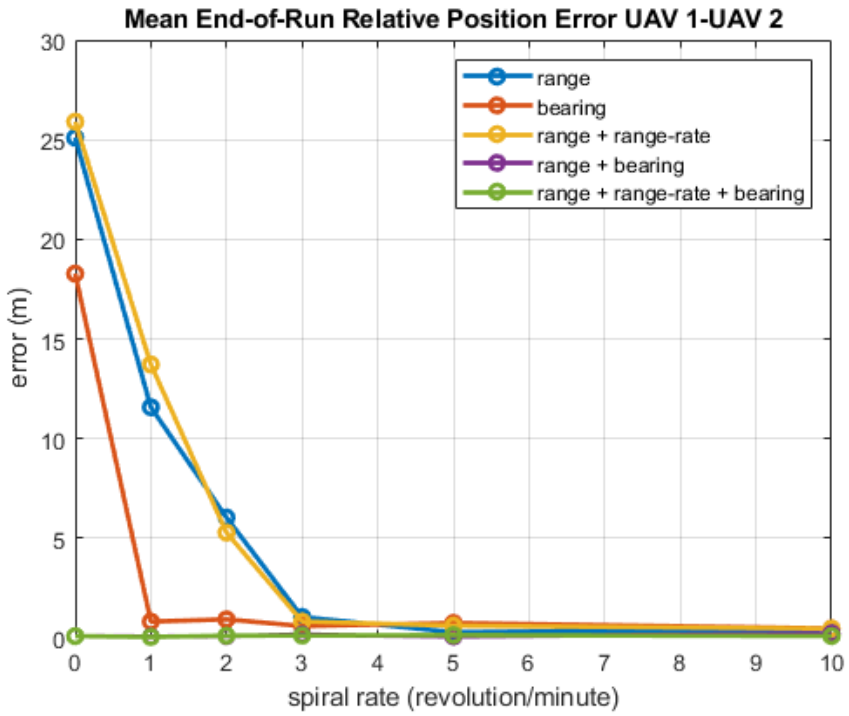

Figure 4.26: Monte Carlo end-of-run position errors between UAV 1 and UAV 2 for varied measurement and UAV maneuver, centralized EKF, 2 UAVs 1 UGV

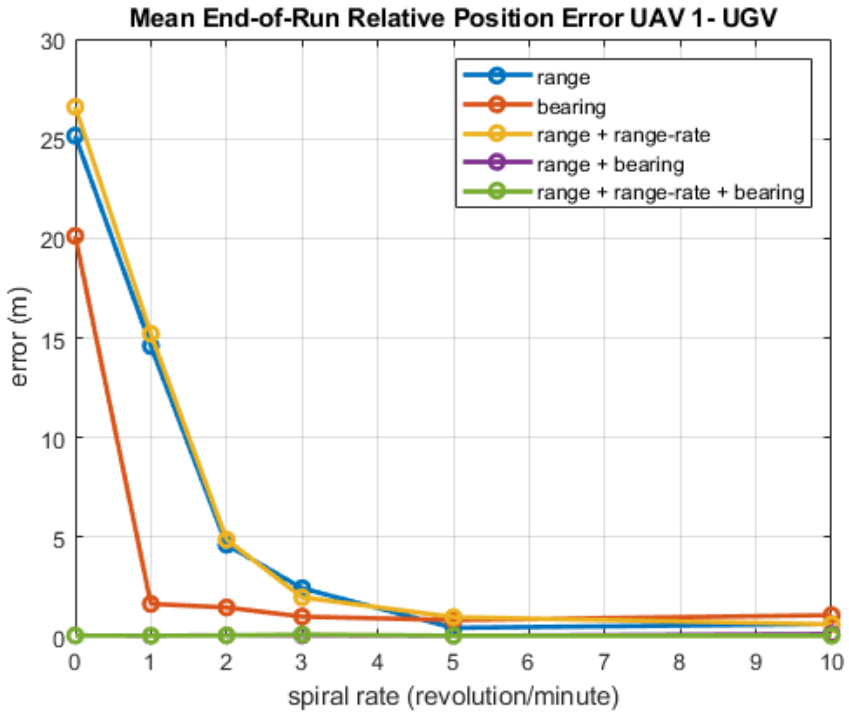

Figure 4.27: Monte Carlo end-of-run position errors between UAV 1 and UGV for varied measurement and UAV maneuver, centralized EKF, 2 UAVs 1 UGV

position observability between these two vehicle types as discussed earlier as a result of the inter-vehicle relative position excitation. Comparing these results to the single UAV - UGV results shown in Figure 4.19 demonstrates the increased relative positioning accuracy that the additional UAV adds to the cooperative group.

While the relative positioning accuracy for this group is slightly worse than the relative positioning for the 3 UAV cooperative group as a result of the reduced inter-vehicle position excitation, additional benefits are seen through cooperation with the UGV. As previously discussed, the UGV simulated here is assumed to be equipped with a higher quality INS and to have access to digital elevation map information. This results in the UGV having a much more accurate absolute position estimate than the UAVs. The UGV absolute position in the vertical direction is bounded by the digital elevation map while the INS drift in the North and East direction increases at a slower rate than the UAV INS solution. Figure 4.28 shows

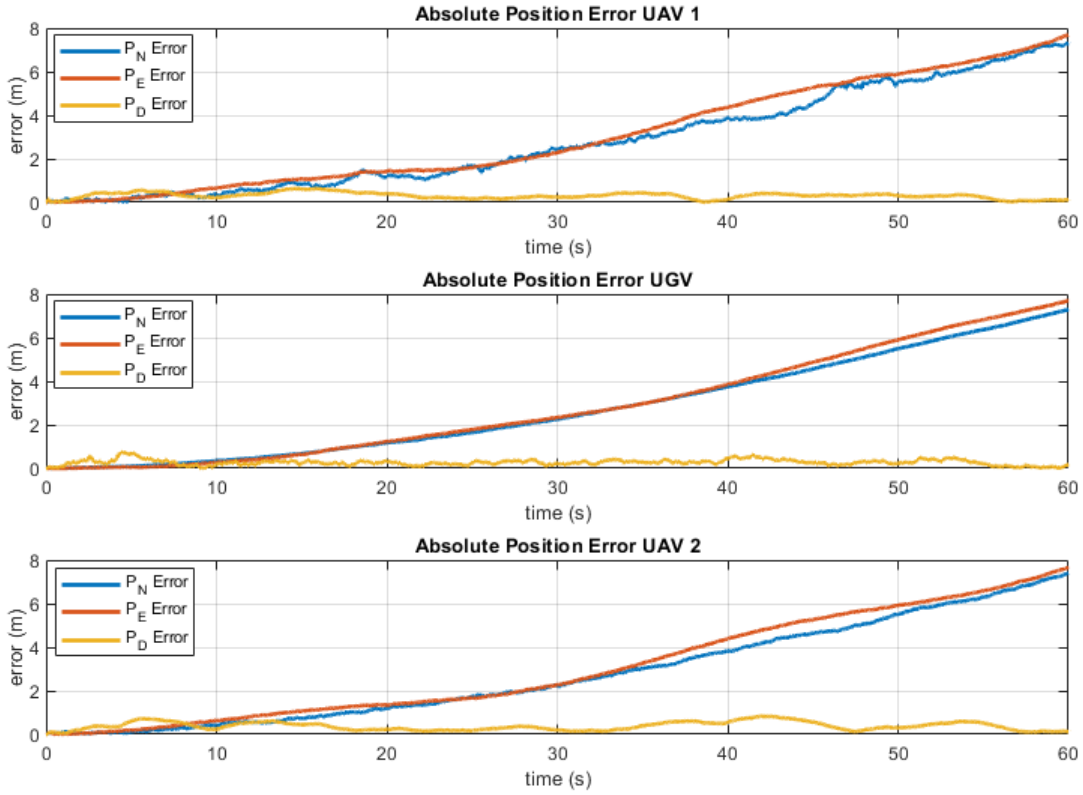

Figure 4.28: Absolute position error for 2 UAV and UGV cooperative group with accurate relative positioning, relying on UGV positioning (IMU & DEM)

the absolute position error growth of an entire cooperative group consisting of 2 UAVs and 1 UGV in a case where accurate relative positioning is able to be obtained. Note that the position error growth characteristics of all three vehicles in the group match those of the UGV. In the absence of this cooperation, the absolute position growth of the UAVs would grow to 55 meters on average, as shown in Table 4.1.

In the case where GPS signals to the ground vehicle are obstructed, but at least one of the UAVs are able to obtain an accurate GPS fix, the UAV can act similar to a GPS "pseudolite" and provide accurate GPS positioning to all other vehicles in the group through cooperative navigation. The absolute positioning errors for this scenario are shown in Figure 4.29. Note that all three vehicles have the same absolute position error characteristics of the most accurate vehicle in the group (i.e. the UAV with the GPS fix).

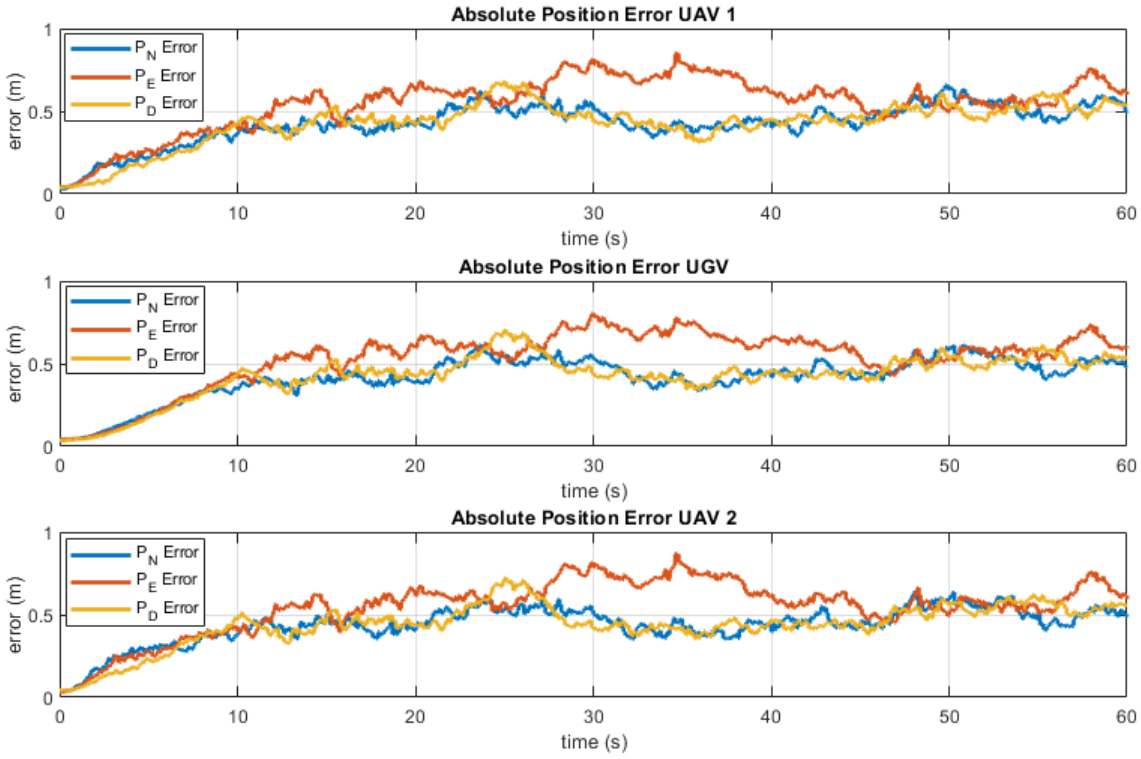

Figure 4.29: Absolute position error for 2 UAV and UGV cooperative group with accurate relative positioning, relying on GPS fix of single UAV

4.6 Conclusions

In this chapter, four scenarios of cooperative navigation were simulated in an environment developed in MATLAB. Each scenario provided results that demonstrated different aspects and potential use cases for cooperative navigation.

The first scenario demonstrated the performance of both centralized and decentralized cooperative navigation algorithms for a small team of two UAVs performing varied levels of a spiral maneuver. Both algorithms produced similar results, with almost no difference in the relative positioning accuracy of the centralized algorithm over the decentralized algorithm. The main drawback of the decentralized algorithm here is that the filter tuning and uncertainty scaling required to obtain sufficient weighting of the measurement update caused the predicted uncertainty (covariance) from the CI algorithm to not be representative of the actual uncertainty. This tuning was also highly heuristic in many cases. Tuning the decentralized algorithm to allow for covariance consistence resulted in decreased positioning accuracy. As a result, for the small vehicle groups traveling in close proximity studied in this work, a centralized approach is recommended. As the size of the cooperative group increases and/or communication distances increase the centralized approach may become less feasible. Decentralized estimation approaches merit future work for these types of scenarios.

It was shown that the increase in observability provided by the spiral maneuver allowed for significant improvements in relative positioning accuracy, depending on the rate of the spiral maneuver and the available cooperative measurements. With both relative range and bearing measurements, the cooperative maneuver was not necessary, as the vehicles were able to accurately estimate relative positions without any vehicle maneuver.

The second scenario, which included a cooperative team of three UAVs, demonstrated the increase in relative positioning performance that adding an additional UAV provided to the overall solution. The additional relative measurement information along with the additional IMU data allowed for improvements in the relative and absolute positioning accuracy of the cooperative team.

The third scenario introduced cooperation between a UAV and a UGV. This scenario demonstrated the complementary nature of cooperative navigation between UAVs and UGVs. The UGV's more accurate IMU information along with its ability to maintain accurate positioning in the vertical direction through the use of digital elevation models greatly improved the absolute positioning accuracy of the UAV when the two vehicles were able to accurately estimate their relative positions. However, relative positioning was more difficult in this case because the relative geometry could not be varied as in the case with multiple UAVs.

The last scenario, which included two UAVs and a UGV, demonstrated the effect of adding an additional UAV when compared to the third scenario (1 UAV, 1 UGV) and the effect of adding a UGV when compared to the first scenario (2 UAVs). The overall relative positioning accuracy between vehicles in this type of group was better than either of the other scenarios with only two vehicles and only slightly worse than the best case with three UAVs. The main benefit with this type of group was the heterogeneous mixture of navigation capabilities of the vehicles in the group. In the case where no vehicles obtained an accurate GPS fix, the absolute position error of the group was limited to the error growth of the UGV which had a more accurate IMU and access to DEM information. In the case where at least one of the UAVs was able to obtain a GPS fix, all vehicles in the group benefited with the same absolute positioning error as the UAV with GPS, assuming that the vehicles were able to accurately estimate their relative positions.

Chapter 5

Experimental Results

In addition to the simulated studies shown in Chapter 4, an experimental data set was collected and post processed in MATLAB in order to validate the simulation results with experimental data.

5.1 Experimental Set-up and Hardware

Two Tarrot X8 octocopters were used to collect experimental data. These UAVs were equipped with Vectornav VN-100 IMUs and Here + GPS receivers along with Time Domain P440 UWB modules to measure inter-vehicle ranges. One of these UAVs is shown in Figure 5.1.

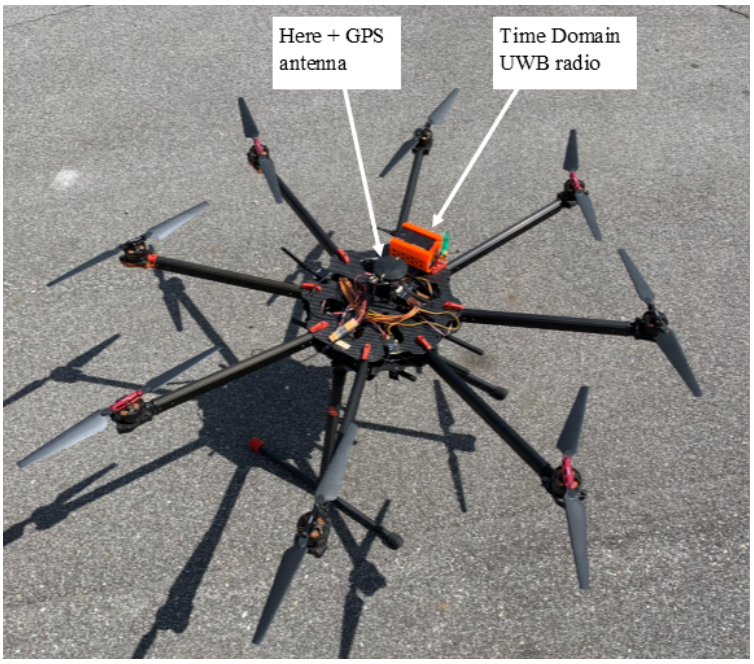

Figure 5.1: Tarrot X8 octocopter with UWB modules and GPS antenna

An Autonomous Stuff Lincoln MKZ was used as the ground vehicle for data collections. The MKZ was equipped with a high quality IMU and GPS receiver as well as a Time Domain P440 UWB module for inter-vehicle ranging. All three of the vehicles used for data collection are shown in Figure 5.2.

Figure 5.2: Vehicles used for data collection

Data was collected at the National Center for Asphalt Technology (NCAT) facility located near Auburn, Alabama. Data, including IMU outputs for all vehicles (100 Hz), GPS positions for all vehicles (2 Hz), and inter-vehicle ranges (10 Hz) were collected and post-processed in MATLAB to analyze the algorithm results. The GPS measurements were primarily used as truth data, but were also assumed to be known for select vehicles in certain data-processing runs to demonstrate the effect of a single vehicle in the cooperative group obtaining an absolute position fix. Relative bearing measurements were simulated based on the GPS truth positions of the vehicles at 2 Hz. These measurements could be taken from camera-based techniques as in [6] or from a UWB antenna array. The data was collected in real-time by a centralized processor (located on the ground vehicle) running a Robot Operating System (ROS) network. The fact that this data collection was performed in a centralized manner without encountering communication problems related to bandwidth

limits provides validation of the feasibility of centralized cooperative navigation for vehicle groups of this size. Therefore, the centralized EKF estimation architecture was used for this experimental study. The processor clocks were synchronized at the beginning of the data collection to minimize timing and latency issues when processing the data. Figure 5.3 was captured during one of the data collection runs on the NCAT skid pad.

Figure 5.3: Data Collection on NCAT skid pad with 2 UAVs and 1 UGV

5.2 Results

Figure 5.4 shows the NED GPS truth positions of the vehicles during the experiment. As shown in the figure, the vehicles began their path on the near side of the skid pad with the UAVs taking off in the vertical direction. The UAVs then began a dynamic maneuver similar to the simulated spiral maneuvers. The rate of this maneuver was slower than the simulated spirals due to maneuverability and control limits on these UAVs. The UGV traveled a straight path, similar to the simulated scenarios. The total horizontal distance traveled by the vehicles in the experiment was about 75 meters, similar to the simulations.

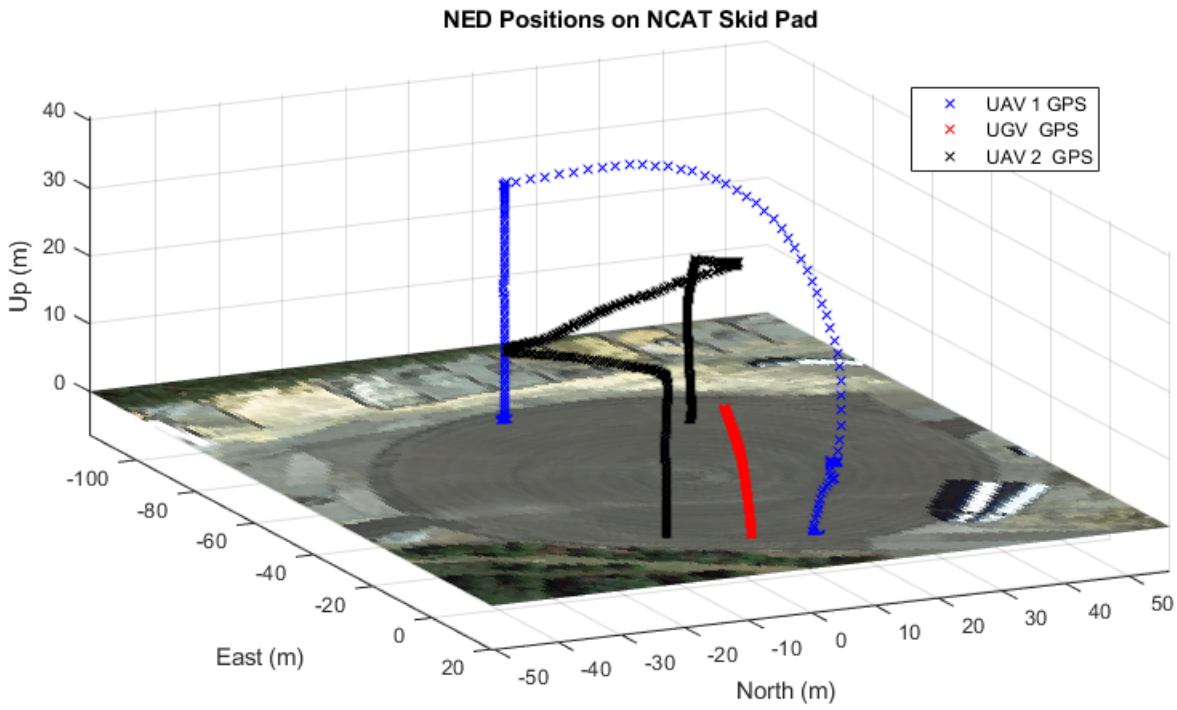

Figure 5.4: GPS truth positions for data collection trajectories

The experiment lasted 145 seconds, including two 20 second periods of static data collection, at the beginning and end of the run.

5.2.1 IMU Measurement Errors

Due to the fact that the UAVs used in this work operate by spinning 8 rotor blades at high speeds, there was a relatively large amount of vibration present on the octocopters during the experiment. This vibration added a significant amount of error and noise to the IMU measurements taken from these vehicles. The raw IMU specific force measurements for a portion of the run is shown in Figure 5.5. Note that there is only a small amount of measurement noise at the beginning of this data since this portion of the data was collected in static conditions. The high noise begins when the octocopter blades start spinning at the 33 second mark. This noise spans from +20 m/s^2 to -40 m/s^2 at certain points in the data run.

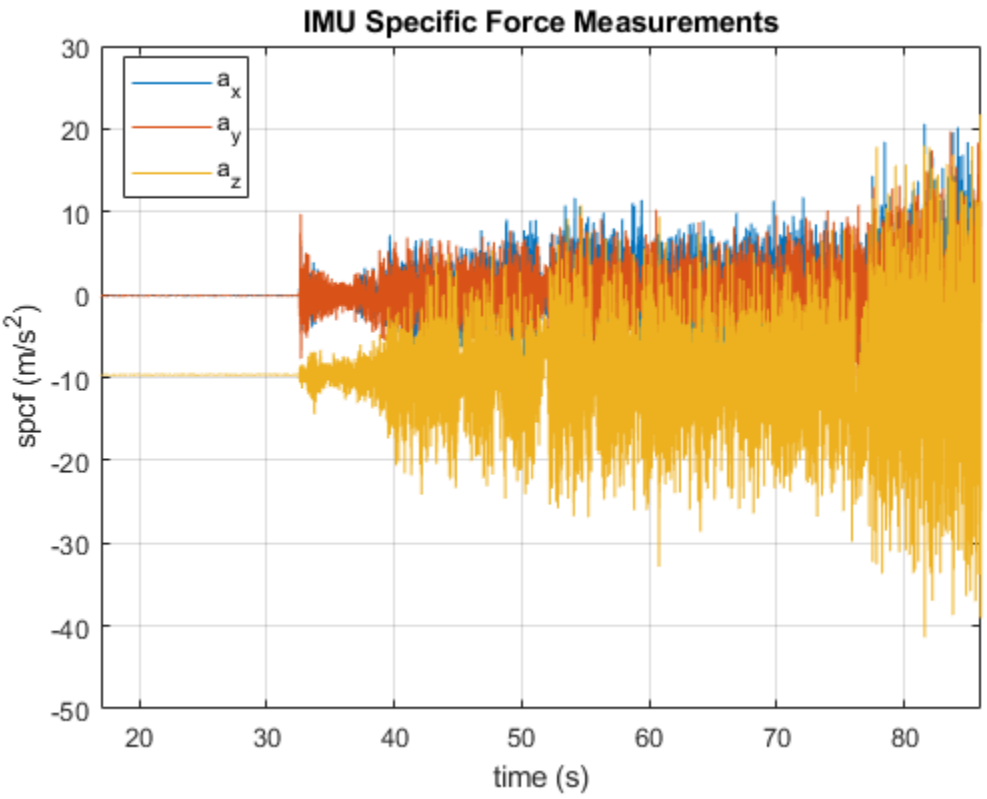

Figure 5.5: IMU noise due to UAV vibration

Mechanizing this noisy data produced a position solution with over 1 km of error after less than 100 seconds. A variety of methods were attempted to compensate for this noise issue. First, rubber isolators were installed to mechanically dampen some of these vibrations. Next, low-pass filtering of the raw data was performed. Neither of these methods, however, produced IMU data that would give a reasonable positioning solution. In [14], Groves discusses various aspects of vibration-induced IMU errors and notes that MEMS (Micro-ElectroMechanical) IMUs (such as the VN-100 IMU used here) are particularly vulnerable to these vibrational errors.

To further attempt to compensate for these errors, a Kalman filter was also implemented to estimate the body frame angular velocities and accelerations using the raw IMU measurements aided with GPS velocity and flight computer attitude. The idea here was to produce better "semi-simulated" IMU measurements that would mimic a slightly more accurate IMU

than the actual raw measurements but still produce realistic mechanization error characteristics in the navigation solution. Unfortunately, this method also failed to produce sufficient estimates of the IMU measurements to produce a reasonable positioning solution.

Ultimately, IMU measurements for the UAVs were simulated by numerically differentiating the GPS velocity measurements, rotating these values into the body frame (using the flight computer attitude solution), and adding bias and noise from the IMU error model in Equation 2.21. These simulated IMU measurements produced reasonable mechanized, IMU-only navigation solutions with 50 to 80 meters of positioning error at the end of run, similar to those simulated in the previous chapter. Another potential avenue for future work could be to investigate IMU mechanization methods in high vibration environments.

Due to much less vibratory nature of a ground vehicle rolling across a smooth surface and the fact that the UGV IMU was of a higher quality than the UAV IMUs, the mechanized, IMU-only solution for the ground vehicle was produced by mechanizing the actual IMU measurements. This solution resulted in about 6 meters of end-of-run positioning error, similar to the simulated case.

5.2.2 Positioning Results

The relative position error for different combinations of relative measurements for all three vehicles is shown in Figure 5.6. The absolute position error is shown in Figure 5.7. Overall, these experimental positioning errors show similar results to the simulation studies. The relative aiding measurements were able to slow the rate of growth of both absolute and relative positions. Relative position became completely observable given a relative range and bearing measurement. With the addition of an absolute reference to only one of the vehicles in this case, all vehicles were able to accurately estimate their absolute positions. Given the UAV maneuver performed during this test, the relative positioning error reduction rate for each combination of relative measurements is similar to the simulated results. The absolute positioning results also demonstrate similar error characteristics to the simulations.

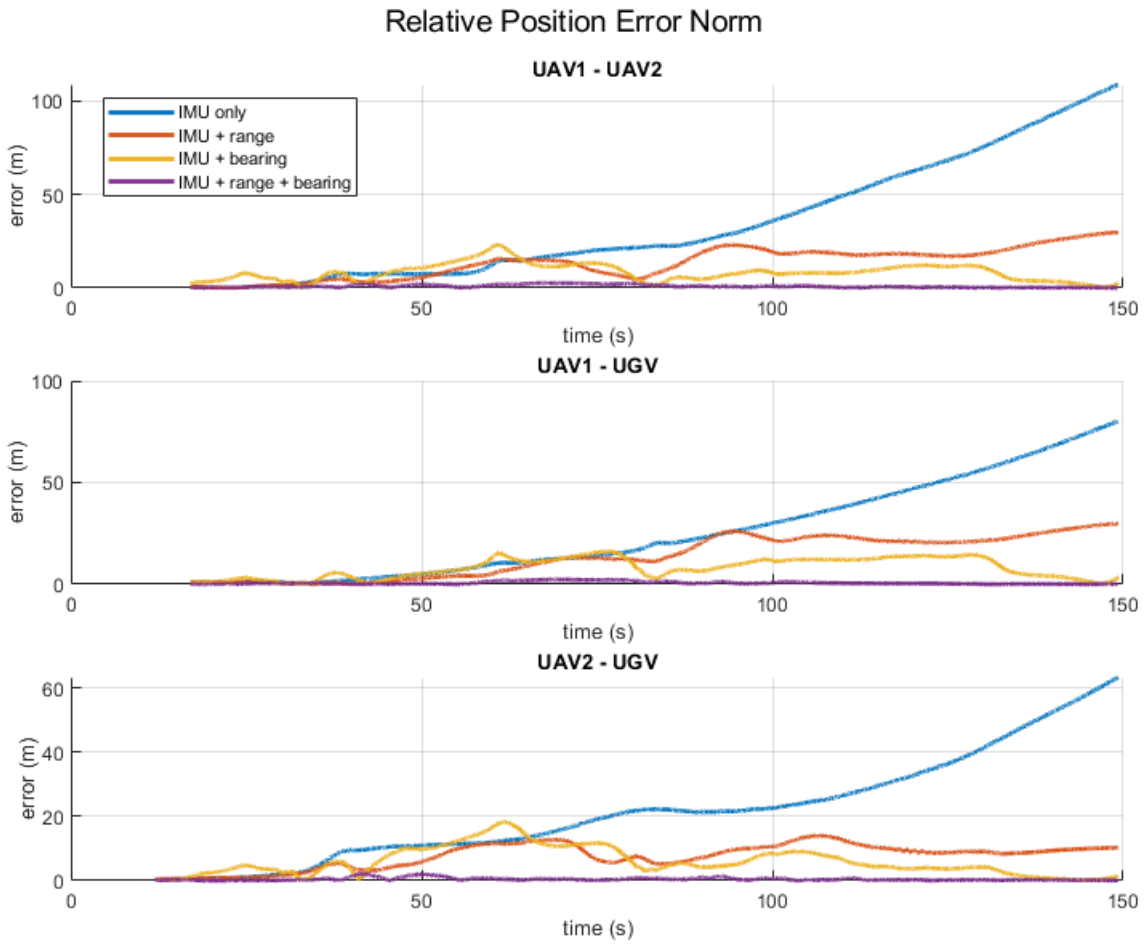

Figure 5.6: Relative Position errors during experimental run

Table 5.1 shows the end-of-run relative position errors from Figure 5.6, and Table 5.2 shows the end-of-run absolute position errors from Figure 5.7. The results from these tables show similar results to the Monte Carlo simulation analysis shown in Figures 4.26 and 4.27. Aiding the IMU-only navigation solution with relative range measurements resulted in a significant reduction in relative position error that matches the simulated results very closely. The results here show a 50 to 70 % reduction in relative positioning error when only cooperative ranging is used for a cooperative group of this type. This is almost exactly the rate of relative position error reduction seen in the simulated scenario for a "spiral rate" between 0 and 1 revolution per minute which is roughly the rate of the experimental maneuver in this test.

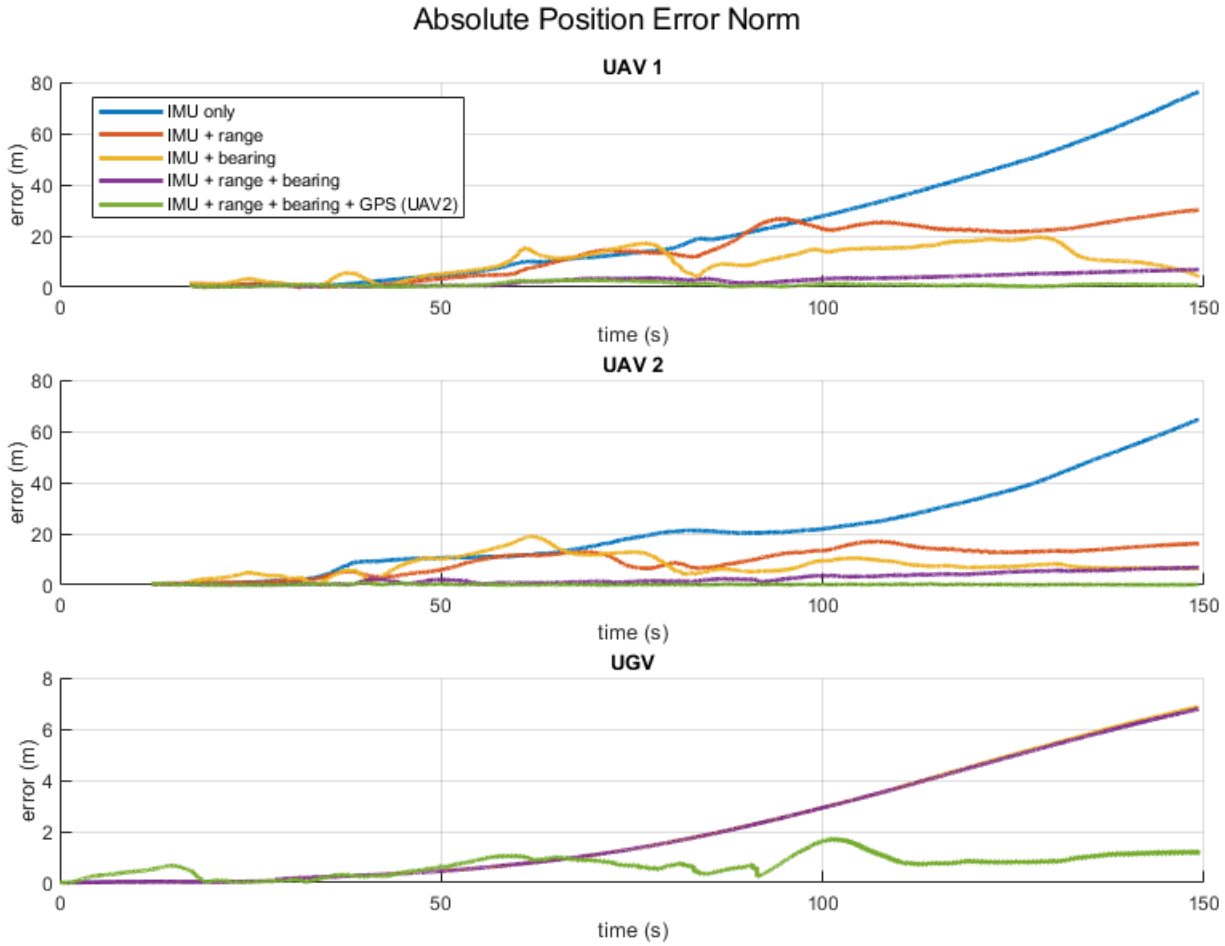

Figure 5.7: Absolute Position errors during experimental run

Aiding the IMU with relative bearing measurements and the UAV maneuver performed in this experimental test provided even more of an improvement in relative positioning. The relative positioning error by the end of the run with this measurement was below 3 meters. This result agrees very closely with the simulation study. Even small amounts of relative position excitation result in accurate relative position estimates with relative bearing measurements. As in simulation, measurements of both relative range and relative bearing resulted in the relative positions becoming fully observable.

With its more accurate IMU solution, the UGV's absolute position received little benefit from the cooperative measurements in every case except for when one of the UAVs was provided absolute position updates from GPS. This result also matches the simulations.

Table 5.1: Experimental end-of-run relative position errors (m)

Navigation Measurements	**UAV 1 - UAV 2**	**UAV 1 - UGV**	**UAV 2 - UGV**
IMU-only	108.7	80.2	63.3
IMU + range	29.6	23.0	10.3
IMU + bearing	1.9	2.7	1.4
IMU + range + bearing	0.2	0.1	0.2

Table 5.2: Experimental end-of-run absolute position errors (m)

Navigation Measurements	**UAV 1**	**UAV 2**	**UGV**
IMU-only	76.3	64.7	6.8
IMU + range	30.0	16.2	6.8
IMU + bearing	6.6	5.9	6.8
IMU + range + bearing	6.9	6.8	6.8
IMU + range + bearing + GPS (UAV 2)	1.0	0.9	1.1

This more accurate position reference did, however, provide significant improvements in the absolute positioning of the UAVs when GPS was unavailable. When the relative positioning error to the UGV was held under 2 meters, the absolute positioning of both of the UAVs were held at the level of the UGV plus or minus the 2 meters of relative position error. A similar effect was seen when relative range and bearing measurements were provided along with GPS measurements to UAV 2. With meter-level positioning provided to UAV 2 and sub-meter relative positioning to this vehicle, the absolute positions of the other two vehicles were held to meter-level accuracy.

By the end of the experimental run, as seen in Tables 5.1 and 5.2, the absolute and relative position error of UAV 1 was slightly larger than the error of UAV 2 in the "IMU + range" and "IMU + bearing" cases. The positioning of UAV 1 was likely less accurate as a result of a combination of a slightly poorer IMU-only positioning solution and reduced position observably experienced by this vehicle from its relative position to the other two vehicles during the experiment.

5.2.3 Observability Analysis

To further investigate UAV 1's slightly poorer positioning accuracy when compared to UAV 2, the observability characteristics discussed in Chapter 3 were analyzed for these runs. Figure 5.8 shows the position Gramian condition number for the relative range measurement only case. As shown in the figure, the condition number for UAV 1 starts much higher than the condition number for the other vehicles, and in the zoomed view, UAV 1's condition number remained the highest during the majority of the dynamic portion of the test.

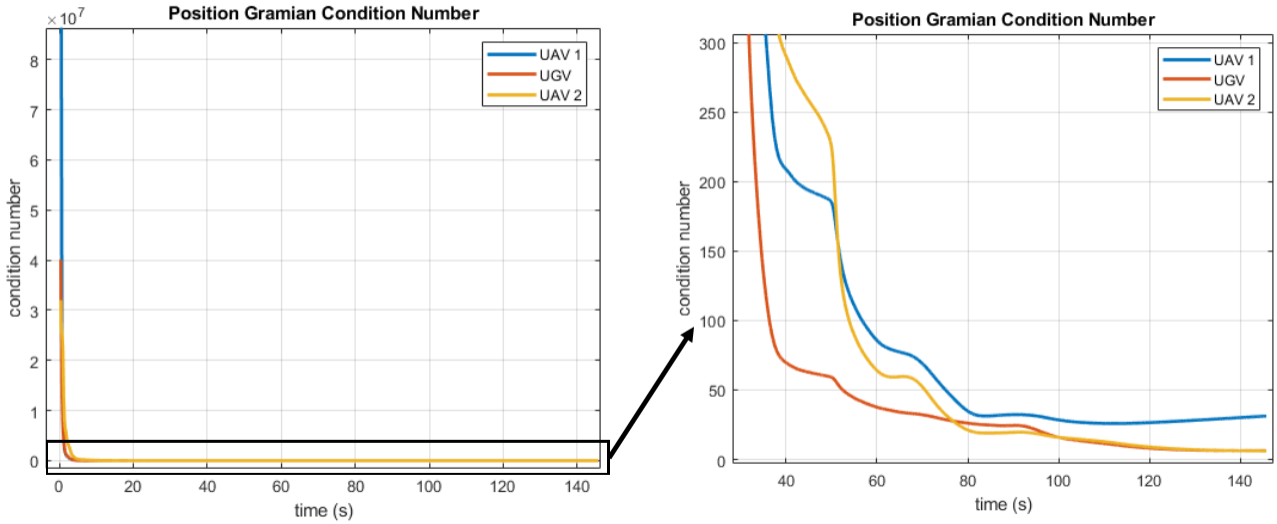

Figure 5.8: Position Gramian condition numbers - relative range only, with zoomed view

Figure 5.9 shows the same position condition number but for the case with relative bearing measurements only. It can be seen here that the condition number for UAV 1 remains the highest for the majority of the test. Additionally, comparing the condition numbers shown for the range aiding measurement in Figure 5.8 and for the bearing aiding measurement in Figure 5.9, the condition number values for the case with relative bearing measurements are significantly lower. This analysis agrees with the positioning error analysis that the relative bearing measurement provides better position observability and estimation accuracy.

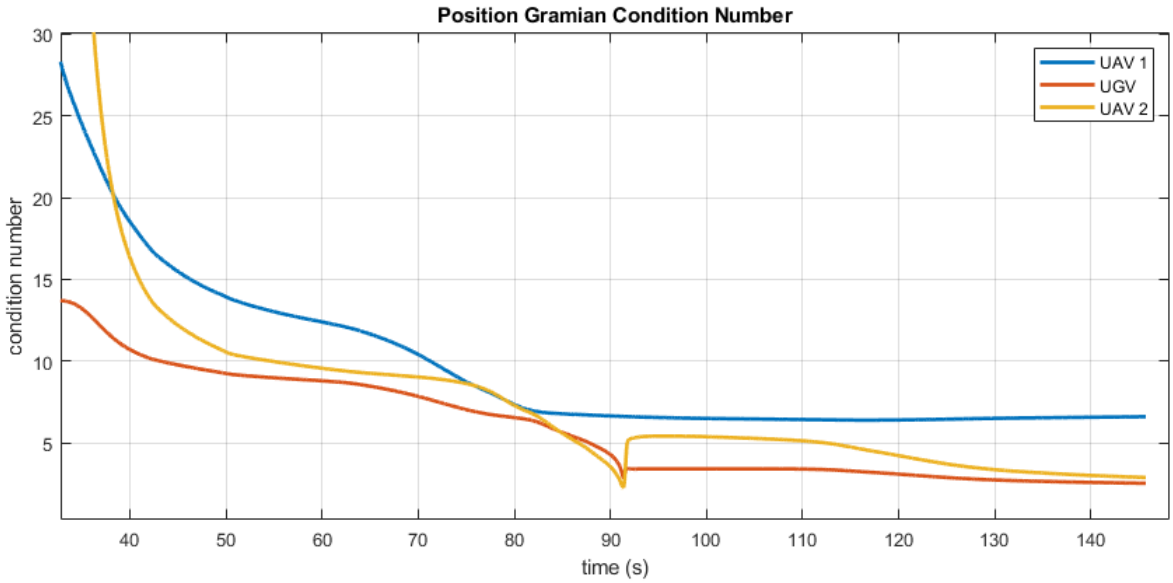

Figure 5.9: Position Gramian condition numbers - relative bearing only

5.3 Conclusions

The experimental results presented in this chapter provide validation of the simulated results presented in Chapter 4. Similar levels of error reduction in both relative and absolute positioning error were seen in both simulation and real-world experiment. This experiment also provided further validation for the use of a centralized cooperative navigation algorithm for small vehicle groups. Furthermore, the observability analysis techniques shown in Chapter 3 were used to analyze the experimental results, showing a similar correlation to estimation error as demonstrated in Chapters 3 and 4.

Chapter 6

Conclusions and Future Work

6.1 Summary

Chapter 1 began this thesis by introducing background information and the motivation for investigating the cooperative navigation problem. Various applications of small autonomous vehicles and their navigation systems were described. The concepts of GPS denied navigation and INS drift were also introduced. Cooperative navigation was chosen as a solution to these problems because of the increasingly wide usage of groups of cooperating autonomous vehicles to complete various missions. Cooperative navigation also requires little additional hardware other than relative measurement sensors and some form of dedicated short range communication (which may already be in place in many applications). This chapter also introduced centralized vs. decentralized estimation architectures, a few ideas to further leverage cooperative navigation, prior work, and thesis contributions.

Chapter 2 introduced the models, algorithms, and other concepts that were heavily relied on for the remainder of the thesis. Namely, a brief overview of the Kalman Filter and Extended Kalman Filter was given along with the NED IMU mechanization used for the time update portion of the algorithm and the measurement models used for the measurement update portion of the algorithm. Where the Extended Kalman Filter was used for cooperative navigation in the centralized case, the Covariance Intersection algorithm was used in the decentralized case. This algorithm was also introduced along with other considerations such as filter tuning.

Chapter 3 discussed observability concepts, observability issues in cooperative navigation, and showed results from some observability simulations. A high degree of similarity

between the linear and empirical forms of the observability Gramian was shown, and performing a condition number test on block-diagonal elements of this Gramian was suggested as a method to analyze the effects of vehicle maneuver and varying measurement availability on cooperative navigation observability. Position dilution of precision calculations were also shown as a method to analyze the quality of observability.

Chapter 4 detailed the simulations performed to evaluate various cooperative navigation methods. Simulations of four types of cooperative groups were considered (2 UAVs, 3 UAVs, 1UAV & 1UGV, 2 UAVs & 1UGV). Each scenario demonstrated distinct aspects of cooperative navigation. First, the case with 2 UAVs was simulated to demonstrate many of the basic characteristics of a simple application of cooperative navigation. For example, the "averaging" of random inertial sensor errors through the knowledge of relative position was shown to reduce the rate of absolute position error growth even in the absence of any absolute position reference. Relative positioning accuracy for varied relative measurements and varied vehicle maneuvers for this case was also shown for both centralized and decentralized algorithms. It was shown that virtually equivalent mean error results are achievable for both the centralized and decentralized algorithms. However, to obtain decentralized results that match the results of the centralized filter, tuning of the measurement covariance was performed that caused the filter's estimated uncertainty not to accurately match the actual uncertainty. For the decentralized case, this introduced a trade-off between accurate covariance estimation and accurate mean error estimation. Decentralized results that maintained accurate covariance bounding were also shown, but these results demonstrated an increase in positioning error compared to the centralized results. The 2 UAV case was also used as a basis for comparison for the other simulation scenarios. The 3 UAV case demonstrated improvements in absolute positioning estimation resulting from the "averaging" of a third randomly biased inertial sensor, assuming that the vehicles were able to accurately estimate their relative positions. This case also demonstrated an improvement in relative positioning accuracy that results from additional measurements shown in the RPMG. The scenario

involving 1 UAV and 1 UGV began to illustrate the advantages of having a heterogeneous mixture of navigation capabilities within a cooperative group. However in this case, as predicted by the observability analysis in chapter 3, the lack of relative maneuverability between the UAV and the UGV caused difficulties in estimating the relative positions of the vehicles in certain cases. The scenario with 2 UAVs and 1 UGV demonstrated the advantages of a heterogeneous cooperative group along with the added relative position observability provided by the second UAV. In this case, the error growth of the entire group was constrained to the level of the best available INS, assuming that the vehicles were able to accurately estimate their relative positions. Additionally, through the UGV's use of digital elevation models, the error in the vertical direction for all vehicles was constrained through this absolute reference. In the case where accurate GPS measurements were available to at least one vehicle in the group, all vehicles were able to constrain their position error to the GPS error, assuming accurate relative positioning.

Chapter 5 showed the experimental validation of the simulated cooperative navigation studies. The experimental hardware setup and data collection methodology was described. The experimental results demonstrated similar characteristics to the simulated results. Relative and absolute errors were reduced by similar amounts in the experiment when compared to the simulation. Relative position error was reduced from over 100 meters to sub-meter accuracy, depending on relative measurement availability. Absolute error was also reduced from over 70 meters to meter-level accuracy depending on measurement availability. Additionally, further validation for the recommendation of a centralized navigation filter for small vehicle groups was provided.

6.2 Conclusions

This thesis investigated a variety of cooperative navigation scenarios from which a few primary conclusions can be drawn. First, this thesis demonstrated a few methods to analyze the observability of cooperative navigation scenarios. An observability Gramian condition

number test was suggested to examine observability characteristics of the scenarios studied here.

Next, combinations of cooperative measurement availability and a spiral class of UAV maneuver with varied frequency were studied to determine the conditions in which accurate relative positioning is possible between four different types of cooperative groups (2 UAVs, 3 UAVs, 1UAV & 1UGV, 2 UAVs & 1UGV). It was shown that accurate relative positioning is possible with only relative range measurements, if sufficient vehicle maneuvers are performed. Relative range-rate measurements added little to the relative positioning accuracy of the vehicles in most cases. With relative bearing measurements only, accurate relative positioning was shown for even slow rates of the inter-vehicle spiral maneuver. If range and bearing measurements were both available to the vehicles, then no maneuver was necessary to observe the relative positions of the vehicles.

In the case where the cooperative vehicles were able to accurately estimate their relative positions, a few implications on the absolute positioning of the vehicles were drawn. First, if any vehicle in the group was able to accurately localize itself to an absolute reference, then all vehicles in the group benefited with those same error characteristics. This absolute reference could include GPS positioning in all three coordinate directions or DEM positioning in only the vertical direction in the case where a UGV was present. The vehicles also benefited with the error characteristics of the most accurate INS in the group (assuming that one INS was known to be of a higher accuracy than others in the group). The vehicles were also able to estimate inertial measurement biases even without an absolute reference. This bias estimation was improved as additional vehicles were added to the group and if a high quality IMU was present in the group. Absolute positioning was also significantly improved in these cases even in the absence of any absolute reference.

Centralized and decentralized estimation architectures for cooperative navigation were also examined and compared. While the centralized architecture has been suggested because of the fact that it retains more uncertainty information within the filter, this method can

place a high computational and communicational load on the centralized processor. The decentralized architecture can reduce this load. It was found that nearly equivalent mean error results could be achieved for both architectures if the navigation filters were properly tuned. However, to achieve these mean error results with the decentralized algorithm, the error covariance had to be tuned in such a way that resulted in estimated state covariance that did not accurately represent the actual navigation state uncertainty. An alternative tuning approach that resulted in better uncertainty bounding was also shown. This approach resulted in significant increases in relative positioning error when relative range was the only available measurement and only a slight increase in error if relative bearing measurements were taken.

Ultimately, based on the results shown in this work, this thesis recommends the use of both relative range and relative bearing measurements to obtain accurate relative positioning if possible or a combination of either range-only or bearing-only measurements and sufficient vehicle maneuver to achieve accurate relative positioning of cooperative vehicles. This thesis also recommends the combination of vehicles equipped with heterogeneous navigation capabilities in cooperative groups. This strategy would allow the entire group to reap the benefits of a wide variety of navigation capabilities that are spread throughout the group. If any one vehicle is able to accurately localize itself to an absolute reference, by any means, then the entire group could share that accurate navigation capability. Finally, based on these results, a centralized architecture is suggested for small cooperative groups of this type. This is primarily due to the fact that this architecture allowed for accurate uncertainty estimates in a variety of conditions that was not achieved with the same accuracy with the decentralized architecture. This recommendation for these applications of small cooperative groups is further prompted by ever-improving communication utilities such as DSRC that have been shown to handle the communication bandwidth requirements for the cooperative navigation of these types of small groups [19].

6.3 Future Work

Many avenues of future work could be taken to build on the work in this thesis. The following list contains a few of these avenues including both continuations of the work presented here and related alternative areas of cooperative navigation research.

- Create a full "closed loop" cooperative navigation - cooperative guidance algorithm that commands specific vehicle maneuvers, takes additional measurements, or includes a path planning strategy when necessary to limit relative position estimation error growth.

- Additional research into more "optimal" vehicle maneuvers to improve observability. Potentially through the use of a search algorithm or machine learning techniques.

- Additional investigation into the correlation between the condition number observability tests and the resulting estimation errors.

- Further consideration of switching or non-fully connected communication topology, as in [7]. This could include an examination of data outages and cooperative navigation integrity during these outages.

- Further refine the tuning methods used for the Covariance Intersection algorithm to improve the covariance bounding of the estimate errors.

- Investigate alternative decentralized cooperative navigation algorithms such as Bounded Covariance Inflation or others.

- Improve upon experimental studies done here by including a UWB antenna array (or another method) to measure relative bearing.

- Perform real-time implementation of the cooperative navigation algorithms described here to further validate their real-world practicality.

- Investigate IMU mechanization methods on highly vibratory platforms.
- Investigate the effects of larger "swarms" of cooperating vehicles to determine the limits of absolute positioning accuracy due to IMU error "averaging," without an absolute reference.
- Investigate cooperative navigation using alternative cooperative guidance laws designed to complete specific missions.
- Further investigate model-aided cooperative navigation strategies as in [1].
- Combine cooperative navigation methods shown here with other alternative navigation methods (i.e. visual, signal-of-opportunity, map-aided [10], magnetic field based methods, etc.) for a more comprehensive GPS denied navigation strategy.

Bibliography

[1] D. M. W. Abeywardena, "Model-Aided State Estimation for Quadrotor Micro Aerial Vehicles," PhD dissertation, University of Technology, Sydney, February 2015.

[2] F. Arrichiello, G. Antonelli, A. P. Aguiar, and A. Pascoal, "Observability metric for the relative localization of AUVs based on range and depth measurements: Theory and experiments," in 2011 IEEE/RSJ International Conference on Intelligent Robots and Systems, Sep. 2011, pp. 3166–3171, doi: 10.1109/IROS.2011.6094466.

[3] K. M. Brink, "Multi-agent relative pose estimation: approaches and applications," in Open Architecture/Open Business Model Net-Centric Systems and Defense Transformation 2018, May 2018, vol. 10651, p. 106510D, doi: 10.1117/12.2303749.

[4] W. L. Brogan. Modern Control Theory, Second Edition. Prentice Hall, 1985.

[5] F. Causa and G. Fasano, "Adaptive Cooperative Navigation Strategies for Complex Environments," in 2020 IEEE/ION Position, Location and Navigation Symposium (PLANS), Portland, OR, USA, Apr. 2020, pp. 100–111, doi: 10.1109/PLANS46316.2020.9110125.

[6] F. Causa, A. R. Vetrella, G. Fasano, and D. Accardo, "Multi-UAV formation geometries for cooperative navigation in GNSS-challenging environments," in 2018 IEEE/ION Position, Location and Navigation Symposium (PLANS), Monterey, CA, Apr. 2018, pp. 775–785, doi: 10.1109/PLANS.2018.8373453.

[7] A. Chakraborty, S. Misra, R. Sharma, and Clark. N. Taylor, "Observability Conditions for Switching Sensing Topology for Cooperative Localization," Un. Sys., vol. 05, no. 03, pp. 141–157, Jul. 2017, doi: 10.1142/S2301385017400039.

[8] A. Chakraborty, S. Misra, R. Sharma, K. M. Brink, and C. N. Taylor, "Cooperative Localization: Challenges and Future Directions," in Cooperative Localization and Navigation, 1st ed., C. Gao, G. Zhao, and H. Fourati, Eds. CRC Press, 2019, pp. 493–519.

[9] A. Chakraborty, C. N. Taylor, R. Sharma, and K. M. Brink, "Cooperative localization for fixed wing unmanned aerial vehicles," in 2016 IEEE/ION Position, Location and Navigation Symposium (PLANS), Apr. 2016, pp. 106–117, doi: 10.1109/PLANS.2016.7479689.

[10] R. Cofield, "MACIN: Map-Aided Cooperative Inertial Navigation for Ground Vehicles," Master's Thesis, Auburn University, May 2020.

[11] F. de Ponte Müller, "Survey on Ranging Sensors and Cooperative Techniques for Relative Positioning of Vehicles," Sensors, vol. 17, no. 2, p. 271, Jan. 2017, doi: 10.3390/s17020271.

[12] D. Gebre-Egziabher, R. C. Hayward, and J. D. Powell, "Design of multi-sensor attitude determination systems," IEEE Transactions on Aerospace and Electronic Systems, vol. 40, no. 2, pp. 627–649, Apr. 2004, doi: 10.1109/TAES.2004.1310010.

[13] S. Gleason and D. Gebre-Egziabher, editors. GNSS Applications and Methods. Artech House Publishers, 685 Canton Street Norwood, MA 02062, 2009.

[14] P. D. Groves, Principles of GNSS, intertial, and multisensor integrated navigation systems. Artech House, 2013.

[15] R. Hermann and A. Krener, "Nonlinear controllability and observability," IEEE Transactions on Automatic Control, vol. 22, no. 5, pp. 728–740, Oct. 1977, doi: 10.1109/TAC.1977.1101601.

[16] G. Indiveri, D. De Palma, and G. Parlangeli, "Single Range Localization in 3-D: Observability and Robustness Issues," IEEE Transactions on Control Systems Technology, vol. 24, no. 5, pp. 1853–1860, Sep. 2016, doi: 10.1109/TCST.2015.2512879.

[17] S. J. Julier and J. K. Uhlmann. "A Non-divergent Estimation Algorithm in the Presence of Unknown Correlations." In Proceedings of the American Control Conference, June 1997.

[18] R. E. Kalman, "A New Approach to Linear Filtering and Prediction Problems," Transactions of the ASME - Journal of Basic Engineering, 82 (Series D), pp.35-45, 1960.

[19] H. Mokhtarzadeh, "Correlated-Data Fusion and Cooperative Aiding in GNSS-Stressed or Denied Environments," PhD dissertation, University of Minnesota, September 2014.

[20] H. Mokhtarzadeh and D. Gebre-Egziabher, "Performance of networked dead reckoning navigation system," IEEE Trans. Aerosp. Electron. Syst., vol. 52, no. 5, pp. 2539–2553, Oct. 2016, doi: 10.1109/TAES.2016.150180.

[21] H. Mokhtarzadeh and D. Gebre-Egziabher, "Cooperative Inertial Navigation," Navigation, vol. 61, no. 2, pp. 77–94, 2014, doi: 10.1002/navi.60.

[22] A. I. Mourikis and S. I. Roumeliotis, "Performance analysis of multirobot Cooperative localization," IEEE Transactions on Robotics, vol. 22, no. 4, pp. 666–681, Aug. 2006, doi: 10.1109/TRO.2006.878957.

[23] J. M. Passerieux and D. V. Cappel, "Optimal observer maneuver for bearings-only tracking," IEEE Transactions on Aerospace and Electronic Systems, vol. 34, no. 3, pp. 777–788, Jul. 1998, doi: 10.1109/7.705885.

[24] M. G. Petovello et al., "Demonstration of Inter-Vehicle UWB Ranging to Augment DGPS for Improved Relative Positioning," JGPS, vol. 11, no. 1, pp. 11–21, Jun. 2012, doi: 10.5081/jgps.11.1.11.

[25] N. D. Powel and K. A. Morgansen, "Empirical observability Gramian rank condition for weak observability of nonlinear systems with control," in 2015 54th IEEE Conference on Decision and Control (CDC), Dec. 2015, pp. 6342–6348, doi: 10.1109/CDC.2015.7403218.

[26] J. A. Preiss, K. Hausman, G. S. Sukhatme, and S. Weiss, "Simultaneous self-calibration and navigation using trajectory optimization," The International Journal of Robotics Research, vol. 37, no. 13–14, pp. 1573–1594, Dec. 2018, doi: 10.1177/0278364918781734.

[27] J. Qi, K. Sun, and W. Kang, "Optimal PMU Placement for Power System Dynamic State Estimation by Using Empirical Observability Gramian," IEEE Transactions on Power Systems, vol. 30, no. 4, pp. 2041–2054, Jul. 2015, doi: 10.1109/TPWRS.2014.2356797.

[28] S. Reece and S. Roberts, "Robust, low-bandwidth, multi-vehicle mapping," in 2005 7th International Conference on Information Fusion, Jul. 2005, vol. 2, pp. 8 pp.-, doi: 10.1109/ICIF.2005.1592009.

[29] I. M. Rekleitis, G. Dudek, and E. E. Milios, "Multi-robot cooperative localization: a study of trade-offs between efficiency and accuracy," in IEEE/RSJ International Conference on Intelligent Robots and Systems, Sep. 2002, vol. 3, pp. 2690–2695 vol.3, doi: 10.1109/IRDS.2002.1041676.

[30] I. Rhee, M. F. Abdel-Hafez, and J. L. Speyer, "Observability of an integrated GPS/INS during maneuvers," IEEE Transactions on Aerospace and Electronic Systems, vol. 40, no. 2, pp. 526–535, Apr. 2004, doi: 10.1109/TAES.2004.1310002.

[31] A. J. Rutkowski, J. E. Barnes, and A. T. Smith, "Path planning for optimal cooperative navigation," in 2016 IEEE/ION Position, Location and Navigation Symposium (PLANS), Apr. 2016, pp. 359–365, doi: 10.1109/PLANS.2016.7479721.

[32] J. Ryan, "A Fully Integrated Sensor Fusion Method Combining a Single Antenna GPS Unit with Electronic Stability Control Sensors," Master's thesis, Auburn University, August 2011.

[33] J. Selikoff, "Coupling GPS/INS and IMM Radar Tracking Algorithms for Precise Collaborative Ground Vehicle Navigation," Master's thesis, Auburn University, December 2018.

[34] R. Sharma, "Observability based control for cooperative localization," in 2014 International Conference on Unmanned Aircraft Systems (ICUAS), May 2014, pp. 134–139, doi: 10.1109/ICUAS.2014.6842248.

[35] R. Sharma, R. W. Beard, C. N. Taylor, and S. Quebe, "Graph-Based Observability Analysis of Bearing-Only Cooperative Localization," IEEE Transactions on Robotics, vol. 28, no. 2, pp. 522–529, Apr. 2012, doi: 10.1109/TRO.2011.2172699.

[36] R. Sharma, S. Quebe, R. W. Beard, and C. N. Taylor, "Bearing-only Cooperative Localization: Simulation and Experimental Results," J Intell Robot Syst, vol. 72, no. 3–4, pp. 429–440, Dec. 2013, doi: 10.1007/s10846-012-9809-z.

[37] R. Sharma and C. Taylor, "Cooperative navigation of MAVs In GPS denied areas," in 2008 IEEE International Conference on Multisensor Fusion and Integration for Intelligent Systems, Aug. 2008, pp. 481–486, doi: 10.1109/MFI.2008.4648041.

[38] V. O. Sivaneri, "UGV-TO-UAV Cooperative Ranging for Robust Navigation in GNSS-Challenged Environments," PhD dissertation, West Virginia University, 2018.

[39] E. G. Smith, "JTIDS: An Update". IEEE Aerospace and Electronic Systems Society Newsletter. Vol. 13, No. 3. March 1978.

[40] R.F. Stengel. Optimal control and estimation. Dover Pubns, 1994.

[41] J. H. Wall, "A Study of the Effects of Stochastic Inertial Sensor Errors," Master's thesis, Auburn University, August 2007.

[42] G. Welch and G. Bishop, "An Introduction to the Kalman Filter," p. 16, 2006.

[43] B. Yang and P. Dutta, "Cooperative Navigation for Small UAVs in GPS-Intermittent Environments," presented at the AIAA Aviation 2019 Forum, Dallas, Texas, Jun. 2019, doi: 10.2514/6.2019-3515.

[44] X. S. Zhou and S. I. Roumeliotis, "Robot-to-Robot Relative Pose Estimation From Range Measurements," IEEE Transactions on Robotics, vol. 24, no. 6, pp. 1379–1393, Dec. 2008, doi: 10.1109/TRO.2008.2006251.

Appendices

Appendix A

State Matrix, A, and Measurement Matrix, H, Elements

As described in Equation 2.20, and repeated here, the 15×1 state vector of the ith vehicle is formulated as:

$$\boldsymbol{x}_i = \begin{bmatrix} \boldsymbol{P}_{NED} \\ \boldsymbol{V}_{NED} \\ \boldsymbol{\Psi} \\ \boldsymbol{b_a} \\ \boldsymbol{b_g} \end{bmatrix} \tag{A.1}$$

where $\boldsymbol{P}_{NED}$ is the 3×1 NED-frame position vector of the vehicle, $\boldsymbol{V}_{NED}$ is the 3×1 NED velocity vector, $\boldsymbol{\Psi}$ is the 3×1 vector of "1-2-3" Euler Angles, and $\boldsymbol{b_a}$ and $\boldsymbol{b_g}$ are the 3×1 accelerometer and gyro biases of the vehicle's IMU, respectively.

Each element of the state matrix, A, is determined by taking the partial derivatives of the nonlinear state equations with respect to each state.

$$A_{i,j} = \frac{\partial f_i}{\partial X_j} \tag{A.2}$$

The nonlinear state equations (see Section 2.1) are repeated here:

$$\dot{\boldsymbol{P}}_{NED} = \boldsymbol{V}_{NED} \tag{A.3}$$

$$R_B^N = R_3(\psi)R_2(\theta)R_1(\phi)$$

$$= \begin{bmatrix} \cos(\theta)\cos(\psi) & -\cos(\phi)\sin(\psi)+\sin(\phi)\sin(\theta)\cos(\psi) & \sin(\phi)\sin(\psi)+\cos(\phi)\sin(\theta)\cos(\psi) \\ \cos(\theta)\sin(\psi) & \cos(\phi)\cos(\psi)+\sin(\phi)\sin(\theta)\sin(\psi) & -\sin(\phi)\cos(\psi)+\cos(\phi)\sin(\theta)\sin(\psi) \\ -\sin(\theta) & \sin(\phi)\cos(\theta) & \cos(\phi)\cos(\theta) \end{bmatrix} \tag{A.4}$$

$$\begin{bmatrix} \dot{V}_N \\ \dot{V}_E \\ \dot{V}_D \end{bmatrix} = R_B^N \begin{bmatrix} a_1 - b_{a1} \\ a_2 - b_{a2} \\ a_3 - b_{a3} \end{bmatrix} \tag{A.5}$$

$$\begin{bmatrix} \dot{\phi} \\ \dot{\theta} \\ \dot{\psi} \end{bmatrix} = \frac{1}{\cos(\theta)} \begin{bmatrix} \cos(\theta) & \sin(\phi)\sin(\theta) & \cos(\phi)\sin(\theta) \\ 0 & \cos(\phi)\cos(\theta) & -\sin(\phi)\cos(\theta) \\ 0 & \sin(\phi) & \cos(\phi) \end{bmatrix} \begin{bmatrix} g_1 - b_{g1} \\ g_2 - b_{g2} \\ g_3 - b_{g3} \end{bmatrix} \tag{A.6}$$

The bias states are estimated as first order processes (from first order Markov process, Equation 2.22):

$$\dot{b} = \frac{-1}{\tau_{bias}} b \tag{A.7}$$

A.1 System Matrix, A, Elements

$\frac{\partial f_{\dot{Pos}}}{\partial \boldsymbol{V}_{NED}}$ terms:

$$A_{1,4} = 1 \tag{A.8}$$

$$A_{2,5} = 1 \tag{A.9}$$

$$A_{3,6} = 1 \tag{A.10}$$

$\frac{\partial f_{\dot{vel}}}{\partial \Psi}$ terms:

$$A_{4,7} = (\cos(\phi)\sin(\theta)\cos(\psi) + \sin(\phi)\sin(\psi))(a_2 - b_{a2}) + (\cos(\phi)\sin(\psi) - \sin(\phi)\sin(\theta)\cos(\psi))(a_3 - b_{a3}) \quad \text{(A.11)}$$

$$A_{4,8} = -\sin(\theta)\cos(\psi)(a_1 - b_{a1}) + \cos(\theta)\sin(\phi)\cos(\psi)(a_2 - b_{a2}) + \cos(\phi)\cos(\theta)\cos(\psi)(a_3 - b_{a3}) \quad \text{(A.12)}$$

$$A_{4,9} = -\cos(\theta)\sin(\psi)(a_1 - b_{a1}) + (-\sin(\phi)\sin(\theta)\sin(\psi) - \cos(\phi)\cos(\psi))(a_2 - b_{a2}) + (\sin(\phi)\cos(\psi) - \cos(\phi)\sin(\phi)\sin(\psi))(a_3 - b_{a3}) \quad \text{(A.13)}$$

$$A_{5,7} = (-\sin(\phi)\cos(\psi) + \cos(\phi)\sin(\theta)\sin(\psi))(a_2 - b_{a2}) + (-\sin(\phi)\sin(\theta)\sin(\psi) - \cos(\phi)\cos(\psi))(a_3 - b_{a3}) \quad \text{(A.14)}$$

$$A_{5,8} = -\sin(\theta)\sin(\psi)(a_1 - b_{a1}) + \sin(\phi)\cos(\theta)\sin(\psi)(a_2 - b_{a2}) + \cos(\phi)\cos(\theta)\sin(\psi)(a_3 - b_{a3}) \quad \text{(A.15)}$$

$$A_{5,9} = \cos(\theta)\cos(\psi)(a_1 - b_{a1}) + (-\cos(\phi)\sin(\psi) + \sin(\phi)\sin(\theta)\cos(\psi))(a_2 - b_{a2}) + (\cos(\phi)\sin(\theta)\cos(\psi) + \sin(\phi)\sin(\psi))(a_3 - b_{a3}) \quad \text{(A.16)}$$

$$A_{6,7} = \cos(\phi)\cos(\theta)(a_2 - b_{a2}) - \sin(\phi)\cos(\theta)(a_3 - b_{a3}) \quad \text{(A.17)}$$

$$A_{6,8} = -\cos(\theta)(a_1 - b_{a1}) - \sin(\phi)\sin(\theta)(a_2 - b_{a2}) - \cos(\phi)\sin(\theta)(a_3 - b_{a3}) \quad \text{(A.18)}$$

$\frac{\partial f_{\dot{vel}}}{\partial \boldsymbol{b_a}}$ terms:

$$A_{4,10} = -\cos(\theta)\cos(\psi) \quad \text{(A.19)}$$

$$A_{4,11} = -\sin(\phi)\sin(\theta)\cos(\psi) + \cos(\phi)\sin(\psi) \quad \text{(A.20)}$$

$$A_{4,12} = -\sin(\phi)\sin(\psi) - \cos(\phi)\sin(\theta)\cos(\psi) \tag{A.21}$$

$$A_{5,10} = -\cos(\theta)\sin(\psi) \tag{A.22}$$

$$A_{5,11} = -\cos(\phi)\cos(\psi) - \sin(\phi)\sin(\theta)\sin(\psi) \tag{A.23}$$

$$A_{5,12} = -\cos(\phi)\sin(\theta)\sin(\psi) + \sin(\phi)\cos(\psi) \tag{A.24}$$

$$A_{6,10} = \sin(\theta) \tag{A.25}$$

$$A_{6,11} = -\sin(\phi)\cos(\theta) \tag{A.26}$$

$$A_{6,12} = -\cos(\phi)\cos(\theta) \tag{A.27}$$

$\frac{\partial f_{\dot{\Psi}}}{\partial \Psi}$ terms:

$$A_{7,7} = \cos(\phi)\tan(\theta)(g_2 - b_{g2}) - \sin(\phi)\tan(\theta)(g_3 - b_{g3}) \tag{A.28}$$

$$A_{7,8} = \sin(\phi)\sec(\theta)^2(g_2 - b_{g2}) + \cos(\phi)\sec(\theta)^2(g_3 - b_{g3}) \tag{A.29}$$

$$A_{8,7} = -\sin(\phi)(g_2 - b_{g2}) - \cos(\phi)(g_3 - b_{g3}) \tag{A.30}$$

$$A_{9,7} = \cos(\phi)/\cos(\theta)(g_2 - b_{g2}) - \sin(\phi)/\cos(\theta)(g_3 - b_{g3}) \tag{A.31}$$

$$A_{9,8} = \sin(\phi)\tan(\theta)/\cos(\theta)(g_2 - b_{g2}) + \cos(\phi)\tan(\theta)/\cos(\theta)(g_3 - b_{g3}) \tag{A.32}$$

$\frac{\partial f_{\dot{\Psi}}}{\partial \boldsymbol{b_g}}$ terms:

$$A_{7,13} = -1 \tag{A.33}$$

$$A_{7,14} = -\sin(\phi)\tan(\theta) \tag{A.34}$$

$$A_{7,15} = -\cos(\phi)\tan(\theta) \tag{A.35}$$

$$A_{8,14} = -\cos(\phi) \tag{A.36}$$

$$A_{8,15} = \sin(\phi) \tag{A.37}$$

$$A_{9,14} = -\sin(\phi)/\cos(\theta) \tag{A.38}$$

$$A_{9,15} = -\cos(\phi)/\cos(\theta) \tag{A.39}$$

$\frac{\partial f_{bias}}{\partial \boldsymbol{b_{a,g}}}$ terms:

$$A_{10...15,10...15} = -1/\tau_{bias} \tag{A.40}$$

A.2 Measurement Matrix, H, Elements

Each element of the measurement matrix, H, is determined by taking the partial derivatives of the nonlinear measurement equations with respect to each state.

$$H_{i,j} = \frac{\partial h_i}{\partial X_j} \tag{A.41}$$

The nonlinear measurement equations are repeated here (see Section 2.2) along with the corresponding measurement matrix elements for each measurement type. Note that the H matrices shown assume that cooperative measurements are taken from vehicle i to vehicle j. For centralized implementations the H matrices below are appended as:

$$H_{centralized} = [H_{vehicle\ 1}\ H_{vehicle\ 2}\ H_{vehicle\ 3}\ \ldots] \tag{A.42}$$

The H matrix row corresponding to additional vehicles (not directly involved in the cooperative measurement) is represented by $\mathbf{0_{1\times 15}}$.

Inter-Vehicle Range Measurement:

$$\rho_{ij} = \sqrt{\Delta P_N^2 + \Delta P_E^2 + \Delta P_D^2} + \eta_\rho \tag{A.43}$$

$$\frac{\partial h}{\partial P_{Ni}} = H_1 = \frac{\Delta P_N}{\sqrt{\Delta P_N^2 + \Delta P_E^2 + \Delta P_D^2}} \tag{A.44}$$

$$\frac{\partial h}{\partial P_{Ei}} = H_2 = \frac{\Delta P_E}{\sqrt{\Delta P_N^2 + \Delta P_E^2 + \Delta P_D^2}} \tag{A.45}$$

$$\frac{\partial h}{\partial P_{Di}} = H_3 = \frac{\Delta P_D}{\sqrt{\Delta P_N^2 + \Delta P_E^2 + \Delta P_D^2}} \tag{A.46}$$

$$\begin{aligned} H_{\rho \ vehicle \ i} &= [H_1 \quad H_2 \quad H_3 \quad \mathbf{0_{1\times 12}}] \\ H_{\rho \ vehicle \ j} &= [\text{-}H_1 \quad \text{-}H_2 \quad \text{-}H_3 \quad \mathbf{0_{1\times 12}}] \end{aligned} \tag{A.47}$$

Inter-Vehicle Range-Rate Measurement:

$$\dot{\rho_{ij}} = \frac{\Delta P_N \Delta V_N + \Delta P_E \Delta V_E + \Delta P_D \Delta V_D}{\rho_{ij}} + \eta_{\dot{\rho}} \tag{A.48}$$

$$\frac{\partial h}{\partial P_{Ni}} = H_4 = \frac{\Delta V_N}{\sqrt{\Delta P_N^2 + \Delta P_E^2 + \Delta P_D^2}} - \frac{\Delta P_N(\Delta P_N \Delta V_N + \Delta P_E \Delta V_E + \Delta P_D \Delta V_D)}{(\Delta P_N^2 + \Delta P_E^2 + \Delta P_D^2)^{3/2}} \tag{A.49}$$

$$\frac{\partial h}{\partial P_{Ei}} = H_5 = \frac{\Delta V_E}{\sqrt{\Delta P_N^2 + \Delta P_E^2 + \Delta P_D^2}} - \frac{\Delta P_E(\Delta P_N \Delta V_N + \Delta P_E \Delta V_E + \Delta P_D \Delta V_D)}{(\Delta P_N^2 + \Delta P_E^2 + \Delta P_D^2)^{3/2}} \tag{A.50}$$

$$\frac{\partial h}{\partial P_{Di}} = H_6 = \frac{\Delta V_D}{\sqrt{\Delta P_N^2 + \Delta P_E^2 + \Delta P_D^2}} - \frac{\Delta P_D(\Delta P_N \Delta V_N + \Delta P_E \Delta V_E + \Delta P_D \Delta V_D)}{(\Delta P_N^2 + \Delta P_E^2 + \Delta P_D^2)^{3/2}} \tag{A.51}$$

$$\begin{aligned} H_{\dot{\rho} \ vehicle \ i} &= [H_4 \quad H_5 \quad H_6 \quad H_1 \quad H_2 \quad H_3 \quad \mathbf{0_{1\times 9}}] \\ H_{\dot{\rho} \ vehicle \ j} &= [\text{-}H_4 \quad \text{-}H_5 \quad \text{-}H_6 \quad \text{-}H_1 \quad \text{-}H_2 \quad \text{-}H_3 \quad \mathbf{0_{1\times 9}}] \end{aligned} \tag{A.52}$$

Inter-Vehicle Relative Bearing (Azimuth):

$$\Lambda_{ij} = \arctan(\frac{\Delta P_N}{\Delta P_E}) - \psi_i + \eta_\Lambda \tag{A.53}$$

$$\frac{\partial h}{\partial P_{Ni}} = H_7 = \frac{\Delta P_E}{\Delta P_N^2 + \Delta P_E^2} \tag{A.54}$$

$$\frac{\partial h}{\partial P_{Ei}} = H_8 = \frac{-\Delta P_N}{\Delta P_N^2 + \Delta P_E^2} \tag{A.55}$$

$$\frac{\partial h}{\partial \psi_i} = H_9 = -1 \tag{A.56}$$

$$\begin{aligned} H_{\Lambda \ vehicle \ i} &= [H_7 \quad H_8 \quad \mathbf{0_{1\times 6}} \quad H_9 \quad \mathbf{0_{1\times 6}}] \\ H_{\Lambda \ vehicle \ j} &= [\text{-}H_7 \quad \text{-}H_8 \quad \mathbf{0_{1\times 13}}] \end{aligned} \tag{A.57}$$

Inter-Vehicle Relative Bearing (Elevation):

$$E_{ij} = \arctan(\frac{-\Delta P_D}{\sqrt{\Delta P_N^2 + \Delta P_E^2}}) - \theta_i + \eta_E \tag{A.58}$$

$$\frac{\partial h}{\partial P_{Ni}} = H_{10} = \frac{\Delta P_N \Delta P_D}{\sqrt{\Delta P_N^2 + \Delta P_E^2}(\Delta P_N^2 + \Delta P_E^2 + \Delta P_D^2)} \tag{A.59}$$

$$\frac{\partial h}{\partial P_{Ei}} = H_{11} = \frac{\Delta P_E \Delta P_D}{\sqrt{\Delta P_N^2 + \Delta P_E^2}(\Delta P_N^2 + \Delta P_E^2 + \Delta P_D^2)} \tag{A.60}$$

$$\frac{\partial h}{\partial P_{Di}} = H_{12} = \frac{\sqrt{\Delta P_N^2 + \Delta P_E^2}}{(\Delta P_N^2 + \Delta P_E^2 + \Delta P_D^2)} \tag{A.61}$$

$$\frac{\partial h}{\partial \theta_i} = H_{13} = -1 \tag{A.62}$$

$$\begin{aligned} H_{E\ vehicle\ i} &= [H_{10} \quad H_{11} \quad H_{12} \quad \mathbf{0_{1\times 4}} \quad H_{13} \quad \mathbf{0_{1\times 7}}] \\ H_{E\ vehicle\ j} &= [\text{-}H_{10} \quad \text{-}H_{11} \quad \text{-}H_{12} \quad \mathbf{0_{1\times 12}}] \end{aligned} \tag{A.63}$$

Absolute Position (GPS):

$$\boldsymbol{P}_{meas} = \boldsymbol{P} + \boldsymbol{\eta}_{GPS} \tag{A.64}$$

$$H_{GPS} = [\boldsymbol{I_{3\times 3}} \quad \mathbf{0_{3\times 12}}] \tag{A.65}$$

Absolute Attitude (AHRS):

$$\boldsymbol{\Psi}_{meas} = \boldsymbol{\Psi} + \boldsymbol{\eta}_{AHRS} \tag{A.66}$$

$$H_{AHRS} = [\mathbf{0_{3\times 6}} \quad \boldsymbol{I_{3\times 3}} \quad \mathbf{0_{3\times 6}}] \tag{A.67}$$

Absolute Vertical Position (DEM):

$$P_{DEM} = P_{Dt} + \eta_{DEM} \tag{A.68}$$

$$H_{DEM} = [\mathbf{0_{1\times 2}} \quad 1 \quad \mathbf{0_{1\times 12}}] \tag{A.69}$$